

University of Southampton Research Repository ePrints Soton

Copyright © and Moral Rights for this thesis are retained by the author and/or other copyright owners. A copy can be downloaded for personal non-commercial research or study, without prior permission or charge. This thesis cannot be reproduced or quoted extensively from without first obtaining permission in writing from the copyright holder/s. The content must not be changed in any way or sold commercially in any format or medium without the formal permission of the copyright holders.

When referring to this work, full bibliographic details including the author, title, awarding institution and date of the thesis must be given e.g.

AUTHOR (year of submission) "Full thesis title", University of Southampton, name of the University School or Department, PhD Thesis, pagination

UNIVERSITY OF SOUTHAMPTON
FACULTY OF ENGINEERING, SCIENCE AND MATHEMATICS
Optoelectronics Research Centre

Polarization engineering with ultrafast laser writing in transparent media

by

Martynas Beresna

Thesis for the degree of Doctor of Philosophy

August 2012

UNIVERSITY OF SOUTHAMPTON
ABSTRACT

FACULTY OF ENGINEERING, SCIENCE AND MATHEMATICS

OPTOELECTRONICS RESEARCH CENTRE

Doctor of Philosophy

Polarization engineering with ultrafast laser writing in transparent media

By Martynas Beresna

In this thesis novel developments in the field of femtosecond laser material processing are reported. Thanks to the unique properties of light-matter interaction on ultrashort time scales, this direct writing technique allowed the observation of unique phenomena in transparent media and the engineering of novel polarization devices.

Using tightly focused femtosecond laser pulses, high average power second harmonic light was generated in the air with two orders of magnitude higher normalised efficiency than reported by earlier studies. We also demonstrated optical vortex generation in the air as a result of spin-orbital momentum coupling in the frequency doubling process.

The ultrashort laser pulses were also explored as a tool for micro-bubble formation. Due to the high refractive index contrast at the interface of a bubble and the glass substrate we observed edge birefringence, which could be utilised for optical vortex generation or as a radial polarizer. The experimental observation was supported by a theoretical model.

Finally, a series of birefringent optical elements were developed based on self-assembled nanostructures induced by ultrashort laser pulses in fused silica. The process was discovered a decade ago and mostly was regarded as a scientific curiosity. However, we demonstrated that these nanostructures can be used as the building blocks for novel optical elements based on spatially varying birefringent properties.

Contents

| | |
|---|-------------|
| UNIVERSITY OF SOUTHAMPTON | 3 |
| ABSTRACT | 3 |
| CONTENTS | I |
| LIST OF FIGURES | V |
| LIST OF TABLES | XV |
| DECLARATION OF AUTHORSHIP | XVII |
| ACKNOWLEDGEMENTS | XIX |
| DEFINITIONS AND ABBREVIATIONS | XXI |
| CHAPTER 1. INTRODUCTION | 1 |
| 1.1 Historical background | 1 |
| 1.2 Thesis overview | 3 |
| CHAPTER 2. LIGHT PROPAGATION IN TRANSPARENT MEDIUM | 5 |
| 2.1 Overview of ultrashort pulse laser systems | 5 |
| 2.2 Laser beam optics | 7 |
| 2.2.1 Gaussian laser beam | 7 |
| 2.2.2 Optical vortex | 8 |
| 2.3 Material modification with laser pulses | 9 |
| 2.3.1 Self-focusing of the laser beam | 10 |
| 2.3.2 Spherical aberration due to refractive index mismatch | 11 |
| 2.3.3 Permanent material modification | 12 |

| | | |
|--|---|-----------|
| 2.3.4 | Permanent material damage and pulse duration | 14 |
| 2.3.5 | Self-assembled nanograting | 17 |
| 2.4 | Jones calculus for polarization optics | 20 |
| CHAPTER 3. EXPERIMENTAL SETUPS | | 23 |
| 3.1 | Direct-writing setup | 23 |
| 3.1.1 | Focusing optics | 27 |
| 3.2 | Setup for the birefringence measurements | 27 |
| 3.3 | Digital holographic microscope | 32 |
| CHAPTER 4. HIGH AVERAGE POWER SECOND HARMONIC GENERATION IN AIR | | 35 |
| 4.1 | Introduction | 35 |
| 4.2 | Generation of second harmonic in isotropic material | 36 |
| 4.3 | Experimental set-up | 39 |
| 4.4 | Experimental results | 40 |
| 4.5 | Conclusions | 45 |
| CHAPTER 5. EFFECT OF EDGE BIREFRINGENCE | | 47 |
| 5.1 | Introduction | 47 |
| 5.2 | Radial edge birefringence | 47 |
| 5.3 | Bubble formation in fused silica with femtosecond laser pulses | 51 |
| 5.4 | Experimental results | 53 |
| 5.4.1 | Bubble formation | 53 |
| 5.4.2 | Polarization conversion | 56 |

| | | |
|--|--|-----------|
| 5.5 | Conclusion | 59 |
| CHAPTER 6. THEORY OF FEMTOSECOND LASER INDUCED NANOGRATINGS | | 61 |
| 6.1 | Introduction | 61 |
| 6.2 | Overview of proposed bulk ripple formation theoretical models | 63 |
| 6.3 | Excitonic model of nanograting formation | 66 |
| 6.4 | Discussion | 69 |
| 6.5 | Conclusions | 70 |
| CHAPTER 7. PROPERTIES OF FEMTOSECOND LASER PULSE INDUCED NANOGRATINGS | | 71 |
| 7.1 | Spectral properties of the nanogratings | 71 |
| 7.1.1 | Modelling spectral properties of nanograting | 71 |
| 7.1.2 | Measuring spectral properties of nanograting | 75 |
| 7.1.3 | Experimental results | 77 |
| 7.2 | Retardance dependence on spherical aberration | 81 |
| 7.3 | Retardance dependence on the numerical aperture | 85 |
| 7.4 | Conclusions | 87 |
| CHAPTER 8. POLARIZATION SENSITIVE ELEMENTS | | 89 |
| 8.1 | Introduction | 89 |
| 8.2 | Polarization diffraction grating | 91 |
| 8.2.1 | Working principle | 91 |
| 8.2.2 | Experimental results | 94 |
| 8.2.3 | Birefringence measurements with polarization grating | 102 |

| | | |
|---|--|------------|
| 8.3 | Polarization converter | 103 |
| 8.3.1 | Introduction | 103 |
| 8.3.2 | Methods for spatially variant polarization generation | 105 |
| 8.3.3 | Form birefringence based polarization converters | 108 |
| 8.3.4 | Fabrication and characterization | 111 |
| 8.3.5 | Application of radial polarization for transparent material processing | 117 |
| 8.4 | 5 dimensional optical memory | 119 |
| 8.4.1 | Multi-dimensional optical memory | 120 |
| 8.4.2 | Optical storage based on nanograting | 121 |
| 8.5 | Conclusions | 126 |
| CHAPTER 9. CONCLUSIONS AND FUTURE WORK | | 129 |
| 9.1 | Summary and discussion | 129 |
| 9.2 | Future work | 132 |
| LIST OF PUBLICATIONS | | 135 |
| BIBLIOGRAPHY | | 143 |

List of figures

Figure 2.1: The intensity distribution of the laser beam focused with a 0.7 NA objective lens into silica glass at a different focusing depth d . '0' position on the z axis corresponds to the focus position if spherical aberration is neglected.....12

Figure 2.2: Schematic diagram of the photoionization of an electron in an atomic potential for different Keldysh parameter values. Source: C.B. Schaffer et al [33] 13

Figure 2.3: Schematic diagram of avalanche (impact) ionization. The free electron absorbs energy through free carrier absorption acquiring sufficient energy to knock-out another electron from the valance to conduction band.....14

Figure 2.4: Damage threshold observed for the surface of fused silica and calcium fluoride at 825 and 1053 nm. Solid lines are fits for $\tau > 0.5$. Deviation from the model for laser pulses shorter than 10 ps indicate presence of different permanent damage mechanism. Source: Perry et al. [18].15

Figure 2.5: Cross-section of the nanograting induced in fused silica with femtosecond laser. Two periodicities can be distinguished; one along light propagation \mathbf{k} and another along the electric field direction \mathbf{E}18

Figure 3.1: Yb:KGW (Yb-doped potassium gadolinium tungstate) femtosecond laser system Pharos, LightConversion Ltd.....23

Figure 3.2: Spectrum of directly diode pumped Yb:KGW femtosecond laser PHAROS24

Figure 3.3: Femtosecond laser direct writing setup. DM – dielectric mirror, SM – silver mirror, I – iris, BS – beam splitter, L – lens, HW – half-wave plate, MO – microscope objective, LC – condenser, LS – light source.26

Figure 3.4: Traditional polarization microscope. The light from the bulb is polarized with a polarizer inserted below the condenser. After the light propagates through the sample it is collected with strain-free objectives and

analyzed with an analyzer. Intensity variation of the specimen allows qualitatively investigate anisotropy of the specimen. Source: MicroscopyU and Nikon..... 28

Figure 3.5: Optical scheme of PolScope (or Abrio) birefringence measurement system. The light emitted by the halogen lamp is initially circularly polarized and projected with the condenser onto the sample. The objective collects the transmitted light, which passes through the universal analyzer comprised of two liquid crystal variable retarders LCA and LCB with 45° between their principal axes and a linear polarizer A. Further the intensity signal is measured with a CCD camera. Source: M. Shribak and R. Oldenbourg [58]..... 29

Figure 3.6: Digital holography microscopy working in transmission mode. The delay line is used to compensate optical path difference for object (**O**) and reference (**R**) waves. Source: www.lynceetec.com..... 32

Figure 4.1: Second harmonic generated in air by tightly focused femtosecond laser pulse with linear (left) and circular (right) polarizations. The white spot is plasma glow at the focus of the objective..... 38

Figure 4.2: Second harmonic vortex generated with circularly polarized pump in accordance with angular momentum conservation (Left). Two-lobe second harmonic pattern with π shifted electric fields for linearly polarized pump (Right). 39

Figure 4.3: Experimental setup for generating second harmonic in air: Half-wave plate and Glan polarizer (P), dichroic mirror (DM), objective (O), condenser (C), CCD camera (CCD), white screen (WS), power meter (D). (Insert) Image of SH pattern for circular polarization. On top of the photography the objective's edge can be seen..... 40

Figure 4.4: Spectra of the first and second harmonics measured with an Avantes spectrometer..... 41

Figure 4.5: Second harmonic power as a function of the pump power. Dashed lines show fit of data with quadratic function..... 41

| | |
|--|----|
| Figure 4.6: CCD images of plasma spot evolution with pump power increase. Numeric values indicate pump power delivered to the focus..... | 42 |
| Figure 4.7: Plasma spot diameter d_{FWHM} dependence on pump power evaluated from the images taken with a CCD camera. | 43 |
| Figure 4.8: Second harmonic power change when compressed HFC gas is blown at the focus spot for two pump powers. The second harmonic increases about 20 times at 0.65 W pump power (blue) and about 4 times at 2.45 W (red). | 44 |
| Figure 5.1: Schematic representation of light ray impinging a void embedded in glass..... | 48 |
| Figure 5.2: (Right) Transmission at the glass/air interface for s and p polarized light versus angle of incidence θ . The black curve represents differential transmission, which in the case of incident circular polarization produces partially linear (p) polarization..... | 49 |
| Figure 5.3: (a) Optical vortex generation on an isotropic sphere. Incident circularly polarized light with plane front ($l = 0$) after refraction on a spherical surface is partially converted into an optical vortex with the orbital angular momentum $l = 2\hbar$. (b, c) Modelled wave-front profiles of incident and transmitted electric field modelled using the Jones matrix formalism. | 50 |
| Figure 5.4: Schematic of the heat-affected regions created by a single (left) and multi-pulse (right) irradiation. Red arrows indicate stress direction and blue ones show stressed material flow which induces compaction..... | 52 |
| Figure 5.5: Side view of femtosecond laser induced structure. (Left) Glass modification after single pulses (enhanced contrast). (Right) Cross-sections of femtosecond laser-induced structures. The number of pulses is indicated above. The laser beam is entering from the top..... | 54 |
| Figure 5.6: Top and side views of the structure formed by femtosecond laser in silica glass (exposition 0.01 s). Right column represents same image taken with | |

| | |
|---|----|
| Abrio system. The pseudo colour indicates direction of the slow axis (see legend) and the intensity relative strength of the retardance..... | 55 |
| Figure 5.7: Optical setups for optical vortex observation. P – polarizer, C – condenser, S – sample, O – objective. Vortex patterns (measured and modelled), observed under left and right handed polarizations, show mirror symmetry indicating reverse of orbital momentum sign. | 56 |
| Figure 5.8: Multiple vortex conversion with an array of micro-voids (a period 10 μm)..... | 58 |
| Figure 6.1: Nanograting period evolution predicted by plasmon interference theory. Inset shows wave vector matching diagram. Image source: [6]..... | 64 |
| Figure 6.2: Evolution of nanoplasma (A) formed at the ionized defects or colour centres into nanoplanes (D). Image source: [112]..... | 65 |
| Figure 6.3: Self-assembled nanograting induced by femtosecond laser irradiation ($\lambda = 1045 \text{ nm}$) inside fused silica. SEM image with backscattered electrons. Two periodicities (along the light propagation and electric field directions) can be clearly seen. The arrows indicate light propagation and electric field \mathbf{E} polarization directions, n – refractive index of fused silica (Source: [114]). | 66 |
| Figure 6.4: Theoretical simulation of the formation of the nanograting. (a) is a schematic of the exciton-polariton dispersion, showing a point on the upper polariton branch (UP) and a point on the lower polariton branch (LP) with the same group velocity, and their splitting in energy ΔE (not in scale). (c) shows the grating in x and in z, while (b) shows a zoom of the grating in the z-direction. | 67 |
| Figure 6.5: Energy as a function of a for $d = 300 \text{ nm}$, showing the minimum at $a = 20 \text{ nm}$ | 69 |
| Figure 7.1: Light with wave number β propagation along the plates of the nanograting. The grating consists of two layers with thickness a (refractive index n_1) and b (refractive index n_2). The image after [124]. | 72 |

Figure 7.2: Form birefringence dispersion calculated for two laminar structure models using exact and approximate formulas. Parameters used for calculation are shown in the legends.....74

Figure 7.3: Retardance measurement set-up. The supercontinuum laser source is emitting a broad spectrum spanning from 450 to 1750 nm. The dichroic mirror is used to reflect strong the fundamental wavelength component. After the mirror the spectrum is 450-750 nm. The polarizers and achromatic half-wave plate are designed to work efficiently at the given wavelengths.....76

Figure 7.4: Retardance dependence of the average power and writing speed for nanogratings induced with 515 nm (below) and 1030 nm (above). The steep increase of retardance at 300-400 mW indicates phase transition from type I to type II modification.....77

Figure 7.5: The birefringent region transmission of 515 nm measured at different distances from the sample. The red line is an exponential fit of the measured data. Exponential decrease in the transmitted intensity confirms our assumption that the main part of the losses is introduced by scattering.....78

Figure 7.6: Losses for group of samples written at 1, 5 and 10 mm/s translation speed with I and II harmonics (1030 nm and 515 nm). The legend indicates the range of average power used during the writing procedure. The large separation between structures written at 200 mW and 300-800 mW indicates presence of I (isotropic refractive index increase) and II type (nanograting) modifications.....80

Figure 7.7: Spectral dependence of femtosecond laser induced retardance in fused silica glass. Oscillations seen on the short wavelength side are due to interference of the coherent white light laser source used in the experiments. The dashed lines indicate independent measurements performed with 3 different laser sources at 515 nm, 1030 nm and 1550 nm.....81

Figure 7.8: Dependence of induced retardance on focusing depth. Pulse energy was 0.75 μ J and numerical aperture 0.7.....82

Figure 7.9: Intensity distribution at the focus for unaberrated x-polarized laser beam focused with 0.7 NA objective. The colorbar indicate difference in the magnitude for x, y and z polarized components. 84

Figure 7.10: Modelled retardance dependence on the focusing depth into the substrate of fused silica. 85

Figure 7.11: Retardance values for nanogratings written with 0.16 NA aspheric lens (Top) and 0.35 NA objective (Bottom) at two translation speeds (1 and 2 mm/s). Dotted lines indicate retardance values of quarter and half wave for 530 nm. 87

Figure 8.1: Scheme to generate radial polarization using a liquid crystal spatial light modulator (SLM) (Source: [133]). Incident linear polarization after being reflected from the SLM is passed through a quarter wave plate, then again reflected from the SLM and after passing through the second quarter wave plate radial polarization is generated. 90

Figure 8.2: Quantitative birefringence microscopy image of polarization diffraction grating. Pseudo colour indicates azimuth of the slow axis. 94

Figure 8.3: Retardance (Top) and azimuth (Bottom) profiles taken along the white dotted line. 95

Figure 8.4: (Left) Grayscale map representation of the birefringent grating phase variation measured with a digital holography microscope. (Right) An optical path variation (taken along the green line) for linear polarization produced by a periodic pattern of the slow axis orientation. 95

Figure 8.5: Directional dependence of written lines when the polarization azimuth is at 45° to the writing direction. Structures are produced of lines separated by 1 μm, white arrows indicate the sample translation direction. If lines are written by translating the sample in both directions two adjacent lines merge together. The effect is clearly seen on the first structure. 97

Figure 8.6: Optical image of the polarization grating. A peculiar pattern could be clearly seen. The smoothness of the induced structure strongly depends on the polarization of the writing beam with respect to the writing direction.....97

Figure 8.7: Far-field diffraction images for linear and circular incident polarizations. Incident polarization state is indicated on the left side. The white light is due to saturation of the CCD camera.....98

Figure 8.8: Diffraction profiles measured for HeNe laser with beam profile meter: a) incident beam profile, b) diffraction pattern for linear polarization, c,d) diffraction patterns for left and right handed circular polarizations.99

Figure 8.9: Far-field diffraction images for circular (right (a) and left (b)) and linear (c) incident polarizations. Respective profiles measured for 515 nm with a beam profile meter: (d,e) diffraction patterns for right and left handed circular polarizations respectively, (f) diffraction pattern for linear polarization..... 100

Figure 8.10: Coloration of birefringent structure in crossed polarizers when additional constant retarder is added. 101

Figure 8.11: Birefringent rose printed in silica glass using ultrashort light pulses. (Color contrast is enhanced). 102

Figure 8.12: Schematic representation of various polarization states. In the upper row all polarizations are spatially homogeneous, while in the lower row both polarizations are spatially variant. 105

Figure 8.13: Schematic drawings of nanogratings distribution in quarter- (a) and half-wave (b) polarization converters. The blue dashes indicate the direction of the nanogratings. 109

Figure 8.14: Principle of radial polarization converter (quarter-wave plate case). Incident circularly polarized light is converted into radially polarized optical vortex due to spatially variant slow axis direction shown in pseudo colour. 110

Figure 8.15: Quantitative birefringence measurements of femtosecond laser written radial polarization converters for circular (c) and linear (d) incident

polarizations. The brightness represents the retardance magnitude while the colour indicates the direction of the slow axis.....112

Figure 8.16: (a) Modelled and (b) measured vortex intensity profiles, (c) diffraction pattern of two interfering vortices, (d) zoomed central part, red circles indicate a ‘fork’ pattern formed due to a phase discontinuity present in the interfering electric field.....113

Figure 8.17: Modelled near- and far-field (top and middle) and measured (bottom) intensity distributions after the polarization converter for incident linear polarization (a) and for left handed circular polarization (i.e., azimuthal polarization with the orbital angular momentum $l = 1$ is generated) at different angles of the polarizer 0° (b), 45° (c), 90° (d), 135° (e). White arrows indicate the incident polarization state.....114

Figure 8.18: Diffraction patterns of radially/azimuthally polarized optical vortices.115

Figure 8.19: Modelled (top) and measured (bottom) profiles of generated radial polarization directly after converter (a) and after polarizer (b-d). White arrows indicate the transmission axis of the polarizer inserted between the converter and a CCD camera.....116

Figure 8.20: A beam profile of the radially polarized laser beam (515 nm) generated with a half-wave converter. The intensity distribution shown on the right is taken along the red line.....116

Figure 8.21: An optical vortex characterization with a beam profiler. After a linear polarizer the optical vortex intensity contrast is less than 0.1% (measurements are limited by the dynamic range of the camera). Inset: zoom of the vortex’s central part. For a linearly polarized vortex, intensity measured in the central part is close to the background value ~ 0.01117

Figure 8.22: Birefringent structures written with a femtosecond radially polarized beam. Clear dependence of the slow axis orientation on writing direction can be seen. The uniform slow axis orientation can be achieved overlapping adjacent

lines (Left), if the interline distance is increased each laser written line has a complex slow axis variation across. 118

Figure 8.23: Abrio image of the line written with radially polarized femtosecond laser beam. White arrow indicates writing direction. The variation of the nanograting orientation manifests as spatial variation of slow axis direction..... 119

Figure 8.24: Schematic description of two parameters describing birefringence: slow axis angle θ and retardance $nx' - ny' \cdot d$ 121

Figure 8.25: Dependence of femtosecond laser induced retardance on the pulse energy. In this experiment the laser repetition rate was set to 200 kHz. For pulse energies higher than 2 μ J strong damage occurs, which leads to reduction of induced retardance. 122

Figure 8.26: Dependence of femtosecond laser induced retardance on the number of pulses (or exposure time) for two different pulse durations (800 fs – black, 270 fs – red). In this experiment the laser repetition rate was set to 200 kHz. 123

Figure 8.27: Images of 8 layers generated with MATLAB code for 5D optical recording demonstration. Each of these layers was assigned a fixed polarization orientation, while the greyscale information was recorded by variation of number of laser pulses..... 124

Figure 8.28: (Left) The Abrio image representing in false colours the recorded information in slow axis and retardance. (Middle and Right) Decoupled images of Maxwell and Newton (no additional operations on images were performed). 126

List of tables

| | |
|--|-----|
| Table 2.1: Representation of various beam polarization states with Jones polarization vectors..... | 21 |
| Table 8.1: Summary of polarization generation methods. | 108 |

DECLARATION OF AUTHORSHIP

I, Martynas Beresna, declare that the thesis entitled **Polarization engineering with ultrafast laser writing in transparent media** and the work presented in the thesis are both my own, and have been generated by me as the result of my own original research. I confirm that:

- this work was done wholly or mainly while in candidature for a research degree at this University;
- where any part of this thesis has previously been submitted for a degree or any other qualification at this University or any other institution, this has been clearly stated;
- where I have consulted the published work of others, this is always clearly attributed;
- where I have quoted from the work of others, the source is always given. With the exception of such quotations, this thesis is entirely my own work;
- I have acknowledged all main sources of help;
- where the thesis is based on work done by myself jointly with others, I have made clear exactly what was done by others and what I have contributed myself;
- parts of this work have been published as:

M.Beresna, P.G.Kazansky, Y.Svirko, M.Barkauskas, R.Danielius

High average power second harmonic generation in air

Applied Physics Letters 95(12), 121502 (2009)

M.Beresna, P.G.Kazansky

Polarization diffraction grating produced by femtosecond laser nanostructuring in glass

Optics Letters 35(10), 1662 (2010)

M.Beresna, M.Gecevicius, P.G.Kazansky, T.Gertus

Radially polarized optical vortex converter created by femtosecond laser nanostructuring of glass

Applied Physics Letters 98(20), 201101 (2011)

M.Beresna, M.Gecevicius, P.G.Kazansky

Polarization sensitive elements fabricated by femtosecond laser nanostructuring of glass
Optical Materials Express 1(4), 783 (2011)

M.Beresna, M.Gecevicius, N.M.Bulgakova, P.G.Kazansky

Twisting light with micro-spheres produced by ultrashort light pulses
Optics Express 19(20), 18989 (2011)

Signed:

Date:.....

Acknowledgements

I would like to express my gratitude to the numerous individuals whose help and support assisted my professional growth during my recent years. I am grateful to the Engineering and Physical Sciences Research Council who gave the opportunity to study in the ORC by supporting my PhD financially.

I am thankful to my bachelor work supervisor, Roland Tomasiunas, who was the first person I met in the research community. His passion for, and dedication to, science encouraged me to embark on science as a career. Sincere thanks are addressed to Peter Kazansky, my PhD project supervisor, who introduced me to the fascinating field of ultrafast optics.

I acknowledge all the help and support from our research group members, Costa, Mindaugas and Nadya. Every one of them is not only a great researcher, but also a great person.

I am sincerely grateful to the technical support team for putting many bits and pieces together in our laboratory.

I owe a particular gratitude to my dear and loving wife Maria and parents and faithful friends.

Finally, I am extremely thankful to my God and Saviour Jesus Christ, without whom nothing would be possible.

Definitions and abbreviations

| | |
|--------------|--|
| E | Electric field |
| P | Induced polarization |
| E_{DC} | External electric field |
| γ | Keldysh parameter |
| ϵ_0 | Electric permittivity in free space |
| μ_0 | Magnetic permeability in free space |
| c | Speed of light in free space |
| n | Refractive index of material |
| n_0 | Linear refractive index |
| n_2 | Nonlinear refractive index |
| n_e | Extraordinary refractive index |
| n_o | Ordinary refractive index |
| $\Delta\phi$ | Phase retardation |
| ϕ | Slow axis azimuth |
| R | Retardance |
| λ | Wavelength of light |
| k_0 | Wavenumber in vacuum |
| $\chi^{(i)}$ | The i -th order susceptibility |
| P | Peak power of the laser pulse |
| P_{cr} | Critical power for self-focusing |
| I_{sf} | Laser intensity reached due to self-focusing |
| τ | Laser pulse duration |
| E_g | Bandgap energy of the material |
| E_{PSF} | Point spread function |
| NA | Numerical aperture |
| SEM | Scanning electron microscope |
| CCD | Coupled charge device |
| OAM | Orbital angular momentum |

| | |
|--------|---|
| Yb:KGW | Yb-doped potassium gadolinium tungstate |
| CW | Continuous wave |
| FWHM | Full width at half maximum |
| SLM | Spatial light modulator |
| SH | Second harmonic |

Chapter 1. Introduction

1.1 Historical background

Processing of transparent materials with lasers has become a fast growing field of research and technology. The very first investigations of laser induced material modifications followed immediately after the invention of the laser in the early sixties. Starting as unwanted consequences of high laser fluencies, this field sought the potential for controllable material structuring. The development of powerful laser systems with high quality beam parameters allowed easily focusing of light to a diffraction limited spot, leading to unprecedented intensities. As a result, lasers could serve as a unique versatile contactless material modification tool.

The 1990s saw a revolution in ultrafast laser technology. The invention of new mode locking mechanisms, namely Kerr-lens mode locking [1] and semiconductor saturable absorber mirrors [2], allowed the generation of stable pulse trains from a solid state laser system. Commercially available femtosecond laser systems can easily provide intensities of 10^{13} W/cm². At such high intensities any transparent material will be ionized leading to non-equilibrium conditions and fast cooling rates, which results in a material phase different from the initial one. Material modification with femtosecond laser systems dates back to 1994 when the first ablation experiments were performed on surfaces of silica [3] and silver [4]. The growing interest into femtosecond laser material processing is related to its unique abilities: inducing highly nonlinear process, altering material properties without excessive production of heat, but at extremely high pressures, modifying almost any transparent material with sub-micron resolution. The arrival of ultrafast laser sources enabled the expansion of the laser processing of transparent materials from surface to three-dimensional (in bulk) modification. The first demonstration was made in 1996 by K. Hirao group in Japan [5] when waveguiding structures were written inside of fused silica glass. At higher energies self-assembled nanostructures inside fused silica could be induced [6]. A more detailed description of this type of modification is presented in Paragraph 2.3.5.

femtosecond laser induced refractive index modification was also applied for micromachining of laser amplifiers in such lasing media as Nd-, Er-Yb-doped glasses [7,8] or a Nd:YAG crystal [9]. The intrinsic nonlinear spatial confinement of femtosecond light pulses was applied to introduce polymerisation into a resin [10]. This two photon polymerization technique enabled printing 3D structures with a 100 nm resolution. The development of new materials for the photopolymerization allowed the use of this technique for applications ranging from photonic devices to tissue engineering [11]. Recently Karlsruhe Technical Institute together with Carl-Zeiss introduced a commercial two-photon polymerization system, Nanoscribe, thus indicating a large commercial potential of the technique. Femtosecond laser micro-processing was also successfully applied for biological samples. The virtues of short light pulses allowed performing a dissection of chromosomes within the nucleus of a living cell [12] and investigate the neuronal network in the roundworm, *C. elegans* [13].

The interaction of ultra short pulses with matter is a complex process and is still not fully understood. Although excitation of the material takes place only during the light pulse propagation through the material, the relaxation can extend up to milliseconds and take different character depending on the experimental conditions. Recent discoveries indicate that the spatio-temporal properties of short light pulses such as pulse front tilt can play a very important role in material modification [14–16]. However, theoretical explanation of these phenomena is still to be found. Another interesting phenomenon is non-reciprocal writing occurring when short light pulses interact with anisotropic materials [17]. This thesis is concerned with the highly nonlinear interaction between intense femtosecond laser pulses and transparent media: gases and glasses, in particular fused silica.

Recent developments of various laser sources tremendously expanded available options for transparent material processing in the sense of lasing medium, available power, pulse duration and etc. A decade ago all ultrafast material processing was made exclusively with Ti:Sapphire systems which were the first stable solid state based femtosecond laser systems delivering light pulses as short as several tens of femtoseconds. However, recently new directly diode pumped

and fibre laser systems became available providing similar or even better parameters in terms of stability and flexibility in a compact and cost effective way. As a result, ultrafast direct writing is turning into a commercially viable technique.

1.2 Thesis overview

Chapter 2: This chapter provides an overview to the basics of light propagation in transparent medium. Nonlinear propagation and ionization mechanisms governing the ultrashort pulse interaction with transparent materials are shortly reviewed. This chapter also introduces spherical aberration – an optical effect playing an important role for focusing with high numerical aperture optics. Also it gives an introduction to Jones matrix calculus which is extensively used throughout the thesis for the description of material anisotropy.

Chapter 3: This chapter describes the experimental setup for the femtosecond laser material processing. The Quantitative birefringence measurement and digital holography techniques which were frequently used in the characterization of the irradiated samples are described as well.

Chapter 4: This chapter presents results on the ultrashort pulse generated second harmonic light in the ambient air. When a powerful femtosecond laser pulse is tightly focused into the ambient air, the laser intensity at the focus is sufficient to ionize the medium. In contrast to the previous work, the high average second harmonic is generated with a high numerical aperture and a relatively small pulse energy. Additionally, due to the momentum conservation law circularly polarized pump generated an optical vortex. High sensitivity to external gas flow is also reported.

Chapter 5: This chapter is dedicated to edge birefringence observed for femtosecond laser produced bubbles in fused silica. A simple theory is invoked to demonstrate that microbubbles can behave as a partial radial polarizer producing a radially polarized optical vortex. The supporting modelling based on Jones calculus and the Fourier transform is in good agreement with the experimental observation.

Chapter 6: In this chapter I overview recent progress in the theory of femtosecond laser induced nanograting formation. The limitations of previous models are discussed together with a new model based on a exciton-polariton mediated self-assembly mechanism, which was suggested by A. V. Kavokin.

Chapter 7: In this chapter I describe properties of the nanograting and their dependence on various parameters of laser irradiation, such as wavelength, pulse duration, fluence and etc.

In house developed broadband birefringence characterization setup is used for the characterization of nanograting form-birefringence dispersion, which is compared with several models dedicated to a layered structure anisotropy description.

Chapter 8: In this chapter I describe several polarization sensitive elements implemented with femtosecond laser induced nanostructures. The first demonstration is a polarization diffractive grating, where an imprinted periodic modulation of the slow axis manifests as a polarization sensitive diffraction. Essentially, this element can be seen as a prism for circular polarization, where an optical path sign depends on the handedness of incident light. This property can be used for polarimetric measurements. The second demonstration is a birefringent beam converter, which can be used to generate cylindrical vector beams or optical vortices. Finally, five-dimensional optical recording is achieved by self-assembled nanogratings. The described technique can be used for robust, high capacity optical memory realisation.

Chapter 9: This chapter concludes the thesis by summarizing the key findings and gives an outlook on future research and developments in femtosecond direct writing.

Chapter 2. Light propagation in transparent medium

2.1 Overview of ultrashort pulse laser systems

In recent years, huge advances have been achieved in the field of ultrafast laser systems. Progress in high power ultrashort pulse lasers has provided deeper insight into the physics of light-matter interaction. At high intensities atoms in gaseous media are ionized and plasma in the interaction volume is formed giving rise to such phenomena as coherent X-ray generation and nonlinear Thomson scattering [18]. A particularly attractive medium due to its abundance is the ambient air, where an intense femtosecond pulse can emit terahertz radiation [19] or control the atmospheric discharge [20]. The modern short pulse laser systems have become not only versatile but also highly reliable and easy to operate. Currently on the market three different laser designs are available.

First are Ti:Sapphire based ultrafast laser systems. This gain medium, having a wide emission bandwidth, allows the generation of light pulses as short as 5 fs with a bandwidth of 350 nm [21]. Additionally, high pulse energies and average powers have been demonstrated. A typical Ti:Sapphire laser oscillator produces 20 fs, 5 nJ, 800 nm pulses at a repetition rate of 90 MHz. After amplification pulses are of about 100 fs and few hundreds of microjoule energy. The repetition rate after an amplifier tends to be from 1 to few hundred kHz. Such systems are the most popular among the other ultrashort pulse laser systems and the most of material processing with ultra-short pulses is performed with them. However, there are several drawbacks of Ti:Sapphire based laser systems. First of all, due to a short life-time of the upper laser level (3 μ s) the gain medium needs to be pumped with an external laser (for instance frequency doubled Nd:YAG). This leads to an increased footprint of the whole system. Additionally, there are basically only two configurations with fixed repetition rates: low repetition rate (1 kHz) and high repetition rate (100 kHz).

A second option has been recently developed, which in many cases can serve as a solid alternative to Ti:Sapphire laser systems. It is based on a Yb:KGW (Yb-doped potassium gadolinium tungstate) crystal, which can be directly diode pumped at 980 nm. Thus an external pump laser is no longer required and the system is much more compact. Typically the oscillator in such laser system produces 80 fs, 13 nJ, 1030 nm pulses at a repetition rate of 76 MHz. By more careful GVD (group velocity dispersion) management pulse duration in the oscillator can be reduced to 50 fs. After stretching, laser pulses can be further amplified to about 200 μ J energy with a pulse duration of 270 fs. The maximum power obtained with the Yb:KGW laser is about 400 μ J and it is limited by stimulated Raman scattering. Further energy increase can be achieved with a different cavity design which is less efficient at high repetition rates [22]. By additional gain management in the laser amplifier pulse duration can be reduced to 150 fs, which is already close to what is delivered by a standard Ti:Sapphire laser system. Most experiments in this thesis are performed using this type of laser system.

The third option is fibre based ultrafast laser sources. Such laser system can be even further reduced in size as stable operation is possible exclusively with air cooling. As a result the fibre laser systems are easy to operate and service. On the other hand such laser systems are restricted to high repetition rates above 1 MHz. At such repetition rates strong thermal accumulation takes place, which reduces the precision of fabricated structures. On the other hand, this regime was explored by several groups for highly symmetric waveguide fabrication, where symmetric refractive index variation is achieved as a result of the non-uniform resolidification created by a thermal gradient.

Further, I will short discuss the principle of solid state ultra-fast laser operation, which is the same for Ti:Sapphire and Yb:KGW laser systems. At the beginning short light pulses are generated inside the oscillator, which should include a gain medium with a broad emission bandwidth, the dispersion management and a mode-locking mechanism. The dispersion management can be achieved by a pair of prisms which add negative dispersion and thus compensates the pulse broadening. However, a more compact and less alignment sensitive design can be

implemented with the use of chirped dielectric mirrors inside the cavity. The mode-locking mechanism can be achieved in two different ways. The first is SESAM (a semiconductor saturable absorber mirror), this mode-locking mechanism allows implementing a self-started mode locking mechanism [23]. Another mode-locking mechanism is based on the Kerr-lens effect [1], which ensures that only most energetic, i. e. the shortest pulses, will sustain in the cavity, thus driving the oscillator into a pulsed operation regime as opposed to CW operation. The Kerr-lens effect requires some fluctuation in the system to be started; typically one of the optical elements is slightly shaken to trigger the effect. Next step is the pulse amplification. As short pulses can become highly intensive during the amplification process the chirped pulse amplification scheme is employed [24]. It requires stretching of the pulse down to several picoseconds before sending it to an amplifier and later compressing it after the amplification. As a result pulses can be amplified up to several Joules [25]. Higher energies requires an advanced laser set-up.

2.2 Laser beam optics

2.2.1 Gaussian laser beam

Gaussian laser beams are by far the most common beam shape used in laser optics. For the Gaussian beam the complex electric field distribution can be written as:

$$E(r, z) = E_0 \left(\frac{\omega_0}{\omega(z)} \right) \exp\left(-\frac{r^2}{\omega^2(z)}\right) \exp\left(-ikz - ik \frac{r^2}{2R(z)} + i\xi(z)\right), \quad (2.1)$$

$$R(z) = z \left(1 + \left(\frac{z_R}{z} \right)^2 \right)$$

$$\omega(z) = \omega_0 \sqrt{1 + \left(\frac{z}{z_r} \right)^2}$$

$$z_r = \frac{\pi \omega_0^2}{\lambda}$$

where E_0 is the amplitude of the electric field, ω is the radius at which the field amplitude drops by $1/e$, z_r is the Rayleigh range and $\xi(z) = \arctan(\frac{z}{z_r})$ is the Gouy phase. The important feature of a Gaussian beam is that it does not change its intensity distribution upon the free space propagation. Also it preserves its shape as it passes through an optical system consisting of simple lenses. This is particularly important for material processing as no additional beam shape control needs to be invoked for beam delivery to the sample.

The real laser systems do not actually generate ideal Gaussian beam, i.e. is not diffraction limited as a result of multimode operation or mode mixing. The parameter used to describe closeness of generated beam to theoretical Gaussian beam is called M squared (M^2). M squared is the ratio of the beam parameter product BPP of an actual beam and ideal Gaussian at the same wavelength. The BPP is given by:

$$BPP = \vartheta \omega_0 \quad (2.2)$$

For diffraction limited beam divergence ϑ is:

$$\vartheta = \frac{\lambda}{\pi \omega_0} \quad (2.3)$$

Thus for Gaussian beam BPP is equal λ/π . For the multimode beam spot size W_{M0} and divergence ϑ_{M0} will be:

$$W_{M0} = M \omega_0 \quad (2.4)$$

$$\vartheta_{M0} = \frac{M \lambda}{\pi \omega_0} \quad (2.5)$$

The BPP then will be M^2 times larger than for diffraction limited Gaussian beam.

2.2.2 Optical vortex

In the paraxial approximation, the angular momentum of light can be split into two parts: spin and orbital angular momentum. The spin angular momentum is related to the gradient of the electric field and the state of polarization. For instance, a circularly polarized beam carries a angular spin momentum of \hbar per photon.

However, it is worth noticing that a circularly polarized plane wave does not carry a spin. The orbital angular momentum is related to the Poynting vector for light fields with inclined wavefronts and is associated with the phase singularities [26]. The last can be described by a local phase dependence of the electric field in the form of $\exp(il\theta)$ where l is an integer number called the topological charge, which corresponds to the number of twists in the phase front within one wavelength, and θ is the azimuthal angle. The generalized expression of the laser beam with a single optical vortex at the centre of the beam can be written as:

$$E(r, \theta, z) = E_0(r, z) \exp(il\theta) \exp(i\Phi(r, z)). \quad (2.6)$$

Such type of optical beams is frequently referred as optical vortices due to their screw like phase front. Then the orbital angular momentum is quantized as $l\hbar$ per photon. Due to the twisting of the phase front the phase in the beam's centre becomes undefined giving rise to an optical singularity and vanishing amplitude at this point. Thus optical vortices are also sometimes referred as doughnut beams.

The manifestation of angular momentum occurs when light is absorbed, scattered or transmitted through birefringent material. In such cases, the angular momentum can be transferred to the matter inducing mechanical angular momentum.

2.3 Material modification with laser pulses

The ultrashort light propagation in transparent material is affected by both linear and non-linear effects. The linear effects include dispersion, aberration and diffraction. The nonlinear effects, which manifest at high intensities, are such as self-focusing, filamentation, plasma defocusing. The strength of each of these effects strongly depends on experimental conditions and laser parameters. The two mostly considered effects from both groups are spherical aberration and self-focusing.

2.3.1 Self-focusing of the laser beam

As was mentioned above self-focusing is a nonlinear effect, which is a result of the intensity dependent nonlinear refractive index:

$$n = \sqrt{1 + \chi^{(1)} + \frac{3}{4}\chi^{(3)}|\mathbf{E}|^2} = n_0 + n_2 I, \quad (2.7)$$

where $\chi^{(i)}$ is the i -th order susceptibility, higher than 4th order terms are neglected due to negligible contribution. The 2nd term of susceptibility is not present in isotropic materials due to inversion symmetry. The $n_0 = \sqrt{1 + \chi^{(1)}}$ is the linear part of refractive index, while $n_2 = \frac{3\chi^{(3)}}{4\epsilon_0 c n_0^2}$ is nonlinear refractive index and $I = \frac{1}{2}\epsilon_0 n_0 c |\mathbf{E}|^2$ is the laser intensity. The Gaussian intensity distribution of the laser pulse creates a lens for the propagating laser beam. The nonlinear refractive index n_2 for a given material is positive at low photon energies, and turns negative for $\hbar\omega \gtrsim 0.7 \cdot E_g$, where E_g is the band gap of the material [27]. Thus the infrared laser beam induces positive lens for itself. Although the refractive index is intensity dependent, the self-focusing depends only on the peak power. This is the result of the balance between laser beam diffraction, which defocuses the beam, and the focusing power of the induced positive lens. The strength of the self-focusing can be estimated from the following formula for the critical peak power at which a laser beam collapses to a focal point:

$$P_c = \frac{3.77\lambda^2}{8\pi n_0 n_2}. \quad (2.8)$$

For fused silica the nonlinear refractive index $n_2 = 2.1 - 3.54 \times 10^{-16} \text{ cm}^2/\text{W}$ [27,28], then the critical power for 1030 nm is in the range of 3.1 to 5.2 MW. The critical power scales with the square of the laser wavelength. Thus the self-focusing threshold is 1.5 times higher for 1030 nm than for 800 nm (the wavelength of a Ti:Sapphire femtosecond laser). Assuming a 300 fs pulse duration, which is typical for a Yb:KGW laser, the pulse energy at critical power is about 1.3 μJ .

The collapse of the laser beam however does not occur, as the material at high intensities becomes highly ionized and the electron gas behaves as a negative lens by contributing a negative index change. The presence of the both processes complicates the evaluation of the laser intensity in the bulk of the material. Self-focusing tends to increase the laser intensity to I_{sf} by:

$$I_{sf} = \frac{I}{1 - \frac{P}{P_{cr}}}, \quad (2.9)$$

where I_{sf} is laser intensity reached due to self-focusing, and P is the actual peak power of the laser beam. However, this simple dependence is valid only for moderate laser powers $< 0.25 P_{cr}$ [29]. At high powers dense electron gas prevents light focusing and leads to intensity clamping [28,30].

2.3.2 Spherical aberration due to refractive index mismatch

A linear effect, which can strongly affect the laser beam, is spherical aberration. The refractive index of fused silica is higher than the air's by 0.5. The light is therefore refracted at the interface between the air and sample. As a result the adjacent part of the beam is focused deeper than the central, thus extending the focal spot in the propagation direction. This also effectively reduces angular spectrum of focused beam, as a result the spot size becomes larger. A precise evaluation of the effect requires calculation of the point spread function [31]:

$$E_{PSF}(\rho, z) = \int_0^\phi \sqrt{\cos \phi_1} \sin \phi_1 (\tau_s + \tau_p \cos \phi_2) J_0(k_0 \rho n_1 \sin \phi_1) e^{i\Phi + ik_0 z n_2 \cos \phi_2} d\phi_1, \quad (2.10)$$

where $\phi = \text{asin } NA$ is the half angle of the light convergence cone, $k_0 = \frac{2\pi}{\lambda}$ is the wavenumber in a vacuum, $\rho = \sqrt{x^2 + y^2}$ is a radial coordinate in the cylindrical coordinate system; ϕ_1 and ϕ_2 are the angles of the incident and refracted ray and are related through Snell's law:

$$\phi_2 = \text{asin} \left(\frac{n_1}{n_2} \sin \phi_1 \right). \quad (2.11)$$

The coefficients τ_s and τ_p are the Fresnel transmission coefficients for s and p polarizations. J_0 is the zero order Bessel function. The function Φ is the spherical aberration function that describes the effect of the refractive index mismatch:

$$\Phi = -k_0 d (n_1 \cos \phi_1 - n_2 \cos \phi_2), \quad (2.12)$$

where d is the distance from the sample surface to the geometrical focus.

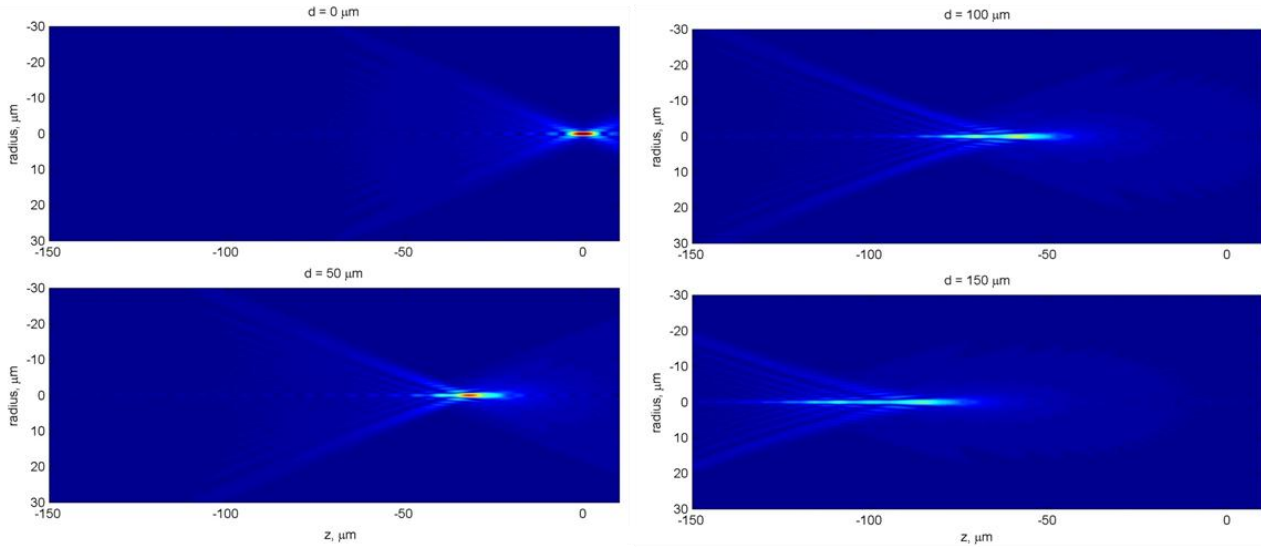


Figure 2.1: The intensity distribution of the laser beam focused with a 0.7 NA objective lens into silica glass at a different focusing depth d . ‘0’ position on the z axis corresponds to the focus position if spherical aberration is neglected.

One can see that this term linearly increases with the distance, and thus deteriorate the phase of the beam and its distribution at the focus (Figure 2.1). The beam focus is moving deeper into the glass substrate with distance d . At high numerical apertures even at relatively small focusing depths, the intensity at the focus is strongly spread along the laser propagation direction, thus reducing intensity.

2.3.3 Permanent material modification

The band gap of dielectrics is typically much larger than the energy of the single photon of the infrared source. For comparison, the band gap of fused silica is about 9 eV, while the photon energy at 1030 nm wavelength is 1.2 eV. In the linear interaction regime, a photon with such energy $\hbar\omega$ is much smaller than the band gap of the material E_g and thus cannot be absorbed. If, however, the light intensity

is high, nonlinear processes can lead to the strong material ionization. There are two classes of such processes: nonlinear photoionization and avalanche ionization [32] (Figure 2.2).

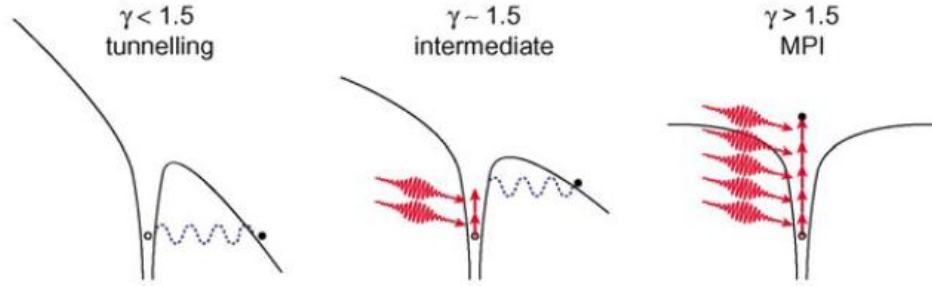


Figure 2.2: Schematic diagram of the photoionization of an electron in an atomic potential for different Keldysh parameter values. Source: C.B. Schaffer et al [33]

Photoionization refers to the direct electron excitation by an electric laser field. Depending on laser frequency and laser intensity, the ionization can occur in the form of tunnelling or multiphoton absorption. Normally, the character of the nonlinear photoionization is evaluated by calculating the adiabatic parameter γ , also widely referred as Keldysh parameter [34]:

$$\gamma = \frac{\omega}{e} \sqrt{\frac{m_e c n_0 \epsilon_0 E_g}{I}}. \quad (2.13)$$

When the Keldysh parameter is smaller than 1.5, the tunnelling process dominates the photoionization, if it exceeds 1.5, then multiphoton process is dominant. In the multiphoton absorption regime, photoionization rate $P_{PI}(I)$ depends strongly on the laser intensity:

$$P_{PI}(I) = \sigma_k I^k, \quad (2.14)$$

where σ_k is the multiphoton absorption coefficient for k -photon absorption. The electron will be excited to the conduction band if the following condition is met:

$$k\hbar\omega \geq E_g. \quad (2.15)$$

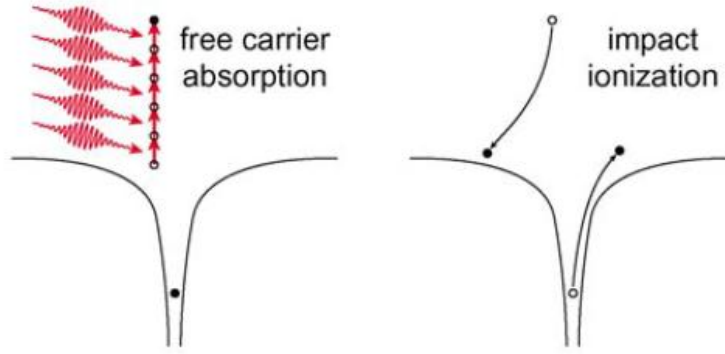


Figure 2.3: Schematic diagram of avalanche (impact) ionization. The free electron absorbs energy through free carrier absorption acquiring sufficient energy to knock-out another electron from the valance to conduction band.

Avalanche ionization involves free-carrier absorption followed by impact ionization [33,35]. The electrons already present in the conduction band are oscillating in the electromagnetic field of the laser and gradually gain net energy by collisions. After the electron energy exceeds that of the band gap, it can ionize, via collision, another electron from the valence band resulting in two electrons near the bottom of the conduction band. Both electrons can again absorb energy and repeat the described energy transfer cycle. The process will continue as long as the light electric field is present. The density of electrons generated through the avalanche process is:

$$\eta_{av}(t) = \eta_0 2^{w_{imp}t} = \eta_0 e^{w_{imp}t \ln 2}, \quad (2.16)$$

where η_0 is initial (seed) electron concentration and w_{imp} is the probability of the impact ionization. One can see that avalanche ionization requires the presence of seed electrons, which trigger the process. The source of the seed electrons η_0 can be photoionization (for ultrashort pulses), intrinsic defects and impurities, which can be easily ionized via linear absorption or thermal excitation [33].

2.3.4 Permanent material damage and pulse duration

When sufficient energy is absorbed via the described mechanisms and is deposited into the material, permanent damage occurs. The damage threshold is the most accepted measure of the permanent damage. There is, however, no widely accepted technique of its measurement. Frequently the damage threshold is

characterized by post-mortem optical measurements [33,36]. Additionally, damage thresholds for the surface and bulk of the material are mostly considered as the same quantity. However, these two situations are quite different. First of all, the laser focus at the surface is not affected by the self-focusing and spherical aberration as for the bulk. Second, the damage threshold on the surface may greatly vary with its preparation (type of the polishing, impurities) and quality.

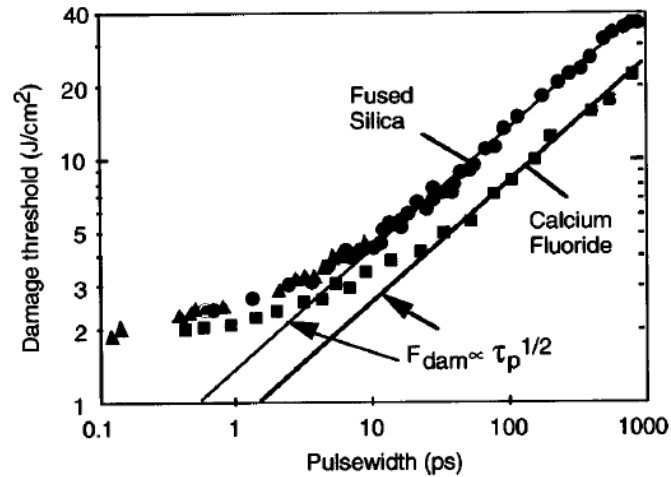


Figure 2.4: Damage threshold observed for the surface of fused silica and calcium fluoride at 825 and 1053 nm. Solid lines are fits for $\tau^{0.5}$. Deviation from the model for laser pulses shorter than 10 ps indicate presence of different permanent damage mechanism. Source: Perry et al. [18].

The character and mechanism of the material modification largely depends on the laser pulse duration. During laser irradiation electric field energy is absorbed by the electrons, which are excited into the conduction band. The excited electrons distribute energy between themselves via carrier-carrier scattering (10-100 fs) and also by carrier-phonon scattering. The first process leads to fast energy redistribution among the excited carriers, the second transfers the energy to the lattice equalizing the temperature of the electrons and the lattice. The typical timescale for the electron energy transfer to the lattice is of tens of picoseconds.

Thus if the laser pulse duration is of the same scale a substantial amount of energy will be transferred to the lattice during the pulse propagation [33]. The excited lattice phonons are transferring energy into the vicinity of the laser focus by thermal diffusion. Later, the material is permanently damaged if the temperature

in the affected zone becomes sufficient to melt it. As a result, strong tension gradient occurs, which leads to fracturing of the material, degrading the quality of the machined material. The damage threshold is then determined by a relative rate of energy deposition and thermal diffusion. It is known that damage threshold (fluence) scales as the square root of the pulse duration. However, with the development of ultrafast lasers a deviation from this law was observed with laser pulses shorter than 10 ps (Figure 2.4). As it was mentioned above, mostly the damage threshold is measured for the surface in order to avoid complications related to non-linear effects such as self-focusing, dispersion and self-phase modulation. The deviation from the square root law can be explained by a rapid electron ionization mechanism. For pulses < 10 ps, thermal diffusion and electron-ion interaction take place after the laser pulse, thus the electrons can reach high temperatures, while keeping the lattice in the cold state. The damage is typically related to the critical plasma concentration, when the laser irradiation is strongly absorbed by the excited electron plasma. However, recent direct measurements of the plasma concentration put this assumption under dispute. It was found that a permanent damage can be induced even if the critical plasma concentration was not reached [28,37].

The permanent modification can be a result of several effects: fast thermal cooling [38], defect generation [39] or micro-explosion [40]. For glass, large thermal gradients, induced by ultrashort laser pulses, lead to a higher fictive temperature and thus create density changes. In the fused silica case density increases with a fictive temperature enabling fabrication of light guiding structures. Photo-excitation also creates colour centres which affect the optical properties of the glass. For fused silica, defects can be classified into two categories: oxygen-deficient defects or oxygen-excess defects. An example for the former case is the E' centre where a silicon atom has one unpaired electron. The latter case includes non-bridging oxygen hole centres [41,42]. The induced defects can be detected by specific absorption and photoluminescence bands. Additionally, the induced defects decrease the damage threshold of the material [43].

2.3.5 Self-assembled nanograting

Depending on the fluence, femtosecond laser irradiation can produce three types of modification in the bulk of fused silica: isotropic refractive index increase [5], nanogratings [6] and voids [44]. However, these three types can be clearly distinguished only for pulses shorter than about 200 fs [45]. At longer pulses nanogratings appear even at relatively low fluencies, just above a permanent modification threshold. Femtosecond laser induced nanogratings possess two periodicities: perpendicular to the polarization and along the light propagation direction [46]. The first grating has a period smaller than the wavelength of light, in the range of 100-300 nm depending on experimental conditions (Figure 2.5). The second period grows from the head of the structure to the tail with the initial period close to the light wavelength λ_0 in the material (refractive index n), i.e. λ_0/n . Recent studies suggest that the nanoplanes of the structure consists of a porous material [47] indicating possible glass decomposition during the irradiation of silica glass.

The nanogratings are able to self-replicate over distances much larger than the spot size of the writing beam. Experiments suggest that the structure imprinted earlier provides initial “seeding” conditions during the formation of the self-organized period assembly in the adjacent region [46]. This property affects the etching rates of the irradiated regions [48] as the etchant can propagate faster when nanoplanes are aligned parallel to the laser written line. Additionally nanogratings exhibit extraordinary thermal stability and sustain the temperatures over 1000°C [49]. On the other hand, femtosecond laser pulses with different polarization can completely overwrite previously modified regions, enabling the exploration of nanogratings as a rewritable optical medium [46,50,51].

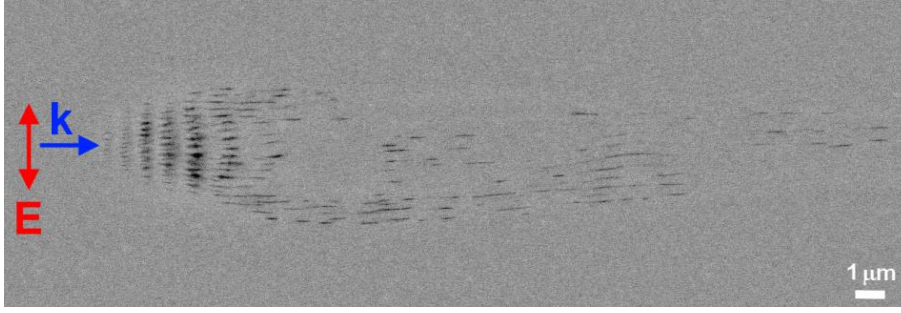


Figure 2.5: Cross-section of the nanograting induced in fused silica with femtosecond laser. Two periodicities can be distinguished; one along light propagation k and another along the electric field direction E (Source: [46]).

The predominant way of characterizing nanogratings is the analysis of the structure under a scanning electron microscope (Figure 2.5). Despite its straightforwardness, the method restricts characterization of the femtosecond laser induced anisotropy to the measurements of the nanograting period. Moreover, it often requires additional post-processing efforts such as sample polishing and etching in fluoric acid. The alternative, nondestructive way of characterizing the anisotropic structure is quantitative birefringence measurements, which provide information on the dependence of induced modification on writing parameters such as fluence, repetition rate, numerical aperture, etc.

The effect of form birefringence, unlike intrinsic birefringence which is due to the anisotropy of oriented molecules, manifests itself due to the alignment of submicroscopic rodlets or platelets [52]. The light polarized parallel to the interfaces experiences a larger refractive index and as a result a phase difference for two perpendicular polarizations is acquired. The strength of the birefringence can be controlled by periodicity and material composition of the microstructure. Under a linear approximation, refractive indices of nanogratings for ordinary n_o and extraordinary n_e wave are:

$$n_e = \sqrt{\frac{n_1^2 n_2^2}{f_f n_2^2 + (1 - f_f) n_1^2}}, \quad (2.17)$$

$$n_o = \sqrt{f_f n_1^2 + (1 - f_f) n_2^2}, \quad (2.18)$$

where f_f - filling factor; n_1 and n_2 are refractive indices for platelets constituting the grating. One can see that

$$n_e^2 - n_o^2 = -\frac{f_f(1-f_f)(n_1^2 - n_2^2)^2}{f_f n_2^2 + (1-f_f)n_1^2} \leq 0, \quad (2.19)$$

i. e. the nanogratings always behave as a negative uniaxial crystal. A typical value of $n_e - n_o$ is $-(2 - 4 \times 10^{-3})$ [49]. For comparison, quartz crystal is a positive uniaxial crystal and $n_e - n_o = 9 \times 10^{-3}$. It is worth mentioning that aligned rodlets produce positive birefringence. Further discussion on the calculation of retardance for form birefringence is presented in Chapter 7.

Birefringent modification can be characterized by two parameters: the retardance and the azimuth of the slow axis. On the other hand, they can be independently controlled during the writing experiment as the retardance is a function of fluence and the azimuth of the slow axis is defined by polarization.

Observation of birefringence which could be controlled by the polarization of a femtosecond IR laser beam was first reported by Sudrie et al [53]. It should be noted that in these experiments the femtosecond laser induced anisotropy was reported to exhibit positive birefringence. Simultaneously, a peculiar scattering with propeller like shape oriented perpendicular to the laser beam polarization was observed in Ge doped silica glass [54]. It was suggested that aligned subwavelength structures are responsible for this scattering. The experimental observation by Sudrie et al. could be explained by well-known anisotropy due to light induced anisotropic bonds rearrangement (light induced anisotropy) [55]. Knowing that the nanograting always acts as a negative uniaxial crystal these experiments does not suggest the presence of the subwavelength structure. However, this can be only error of sign made in the experiment. All further experiments confirmed the presence of negative birefringence. Discovery of the nanograting produced in the bulk of the material provided an appropriate explanation for the both effects. Under certain conditions this type of glass modification can be an undesirable effect. As revealed from the studies of the glass modification dependence on the pulse duration, for pulses longer than ~ 200 fs a

smooth refractive index increase cannot be achieved [45]. If waveguides are to be written using relatively long pulses >200 fs, they potentially can be polarization sensitive, additionally, some losses can also occur due to nanograting formation [56]. However, at megahertz repetition rates birefringence is strongly reduced, probably due to heat accumulation effects [57,58].

2.4 Jones calculus for polarization optics

In optics, polarized light can be effectively described in an extremely compact mathematical form using Jones calculus. It can be viewed as simplified version of Mueller Calculus, which uses a full description of light by Stokes vectors, thus can be used for analysis of partially polarized or unpolarized light. However, in most cases the main interest is to analyse the propagation of polarized light, which is typical situation for the laser beam propagation. As a result Jones calculus becomes very handy for such type of analysis and it was extensively used throughout all of my postgraduate work.

In Jones calculus, the polarization of the beam is described by a two element column vector, where the amplitudes of electric field, in general, are complex numbers. Depending on the coordinate system, one can use linear (vertical and horizontal) [59], circular (left and right handed) [60] or even cylindrical (radial and azimuthal) [61] polarizations as unit vectors for polarization description. Here we will use most accepted form, where linear polarizations are the unit vectors used to describe any state of polarization. In this coordinate system, linear horizontal (LHP) and linear vertical (LVP) polarizations are respectively expressed as following:

$$\mathbf{E}_{LHP} = \begin{pmatrix} 1 \\ 0 \end{pmatrix} \quad (2.20)$$

and

$$\mathbf{E}_{LVP} = \begin{pmatrix} 0 \\ 1 \end{pmatrix}. \quad (2.21)$$

Then any arbitrary state of polarization \mathbf{E} is written as a linear superposition of these two states:

$$\mathbf{E} = \begin{pmatrix} E_x \\ E_y \end{pmatrix} = \begin{pmatrix} E_{0x}e^{i\delta_x} \\ E_{0y}e^{i\delta_y} \end{pmatrix}. \quad (2.22)$$

The intensity I can be determined by multiplying Jones vector with its complex conjugate:

$$I = \mathbf{E}^\dagger \cdot \mathbf{E} = (E_x^* \ E_y^*) \begin{pmatrix} E_x \\ E_y \end{pmatrix} = E_x^*E_x + E_y^*E_y. \quad (2.23)$$

Here is a table of Jones polarization vectors for mostly used polarization states:

| Linear horizontal | Linear vertical | Circular left-handed | Circular right-handed | Radial | Azimuthal |
|---|---|---|--|--|--|
| $\mathbf{E}_{LHP} = \begin{pmatrix} 1 \\ 0 \end{pmatrix}$ | $\mathbf{E}_{LVP} = \begin{pmatrix} 0 \\ 1 \end{pmatrix}$ | $\mathbf{E}_{LCP} = \frac{1}{\sqrt{2}} \begin{pmatrix} 1 \\ -i \end{pmatrix}$ | $\mathbf{E}_{RCP} = \frac{1}{\sqrt{2}} \begin{pmatrix} 1 \\ i \end{pmatrix}$ | $\mathbf{E}_{RAD} = \begin{pmatrix} \cos \phi \\ -\sin \phi \end{pmatrix}$ | $\mathbf{E}_{AZI} = \begin{pmatrix} -\sin \phi \\ \cos \phi \end{pmatrix}$ |

Table 2.1: Representation of various beam polarization states with Jones polarization vectors.

where ϕ is the polar angle in polar coordinate system.

A polarizing element in Jones calculus is represented as a 2×2 matrix:

$$J = \begin{pmatrix} j_{xx} & j_{xy} \\ j_{yx} & j_{yy} \end{pmatrix}. \quad (2.24)$$

The effect of the polarizing element on the polarization \mathbf{E}_{IN} of the propagating beam is then described as:

$$\mathbf{E}_{OUT} = J \cdot \mathbf{E}_{IN}. \quad (2.25)$$

Frequently, a polarization element has to be rotated around the z axis. This important operation is performed with a help of rotation matrix:

$$J_{ROT}(\theta) = \begin{pmatrix} \cos \theta & \sin \theta \\ -\sin \theta & \cos \theta \end{pmatrix}. \quad (2.26)$$

For a polarizing element rotated by angle θ the Jones matrix is given by:

$$J(\theta) = J_{ROT}(-\theta) \cdot J \cdot J_{ROT}(\theta). \quad (2.27)$$

Chapter 3. Experimental Setups

The experimental work presented in this thesis involved the modification of optically transparent media with femtosecond laser pulses. Section 3.1 describes the setup employed for writing the predefined patterns into the materials. The rest of the chapter describes characterization setups used routinely in this work.

3.1 Direct-writing setup

In the first year of my studies, the new direct writing setup was assembled in the laboratory of our group, which was later used throughout all of my PhD work. The radiation source was a Light Conversion directly diode pumped 6 W femtosecond laser system “Pharos” (Figure 3.1). This type of laser system in many aspects is more suitable for ultrafast laser material processing compared to Ti:Sapphire laser systems.

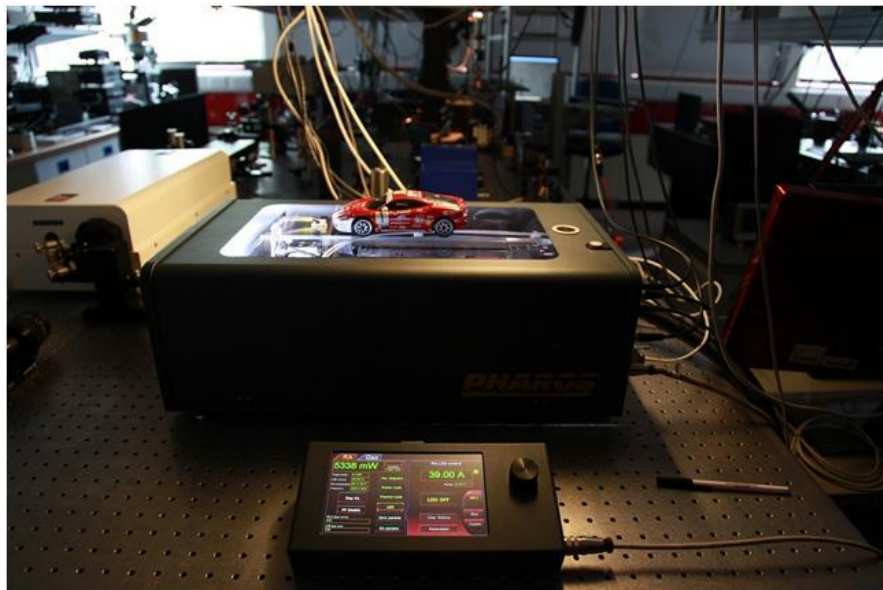


Figure 3.1: Yb:KGW (Yb-doped potassium gadolinium tungstate) femtosecond laser system Pharos, LightConversion Ltd.

The main advantage is the possibility to pump laser crystals in the oscillator and amplifier directly with laser diodes without the need of an external laser source. As a result the laser system is more stable and compact with greater flexibility of such parameters as repetition rate and pulse energy. However, Yb:KGW based systems

at the amplifier output have pulses of about 270 fs, which is about twice longer than of the conventional Ti:Sapphire system. Although pulse duration can play a critical role in material modification process, in most situations Ti:Sapphire can be fully replaced with Yb:KGW systems. Comparing with ultrafast fibre laser systems, our “Pharos” at the output can give up to 200 μJ of pulse energy, while fibre systems are limited to few microjoules. The laser system operates at 1030 nm wavelength with 8 nm bandwidth.

The shortest pulse duration available with this system is 270 fs, and longer pulse durations were obtained by the detuning of built-in optical pulse compressor. The pulse duration was constantly monitored using a single shot autocorrelator, APE PulseCheck. Additional pulse inspection was performed with a Grenouille (simplified single shot FROG version) from Swamp Optics. The pulse spectrum was occasionally checked with an Avantes fibre coupled spectrometer (Figure 3.2). The pulse repetition rate could be varied from 10 to 500 kHz. Single pulse extraction was possible with an externally triggering pulse picker. Later this system was upgraded with a higher harmonic generation module “Hiro”, which was used for second harmonic generation.

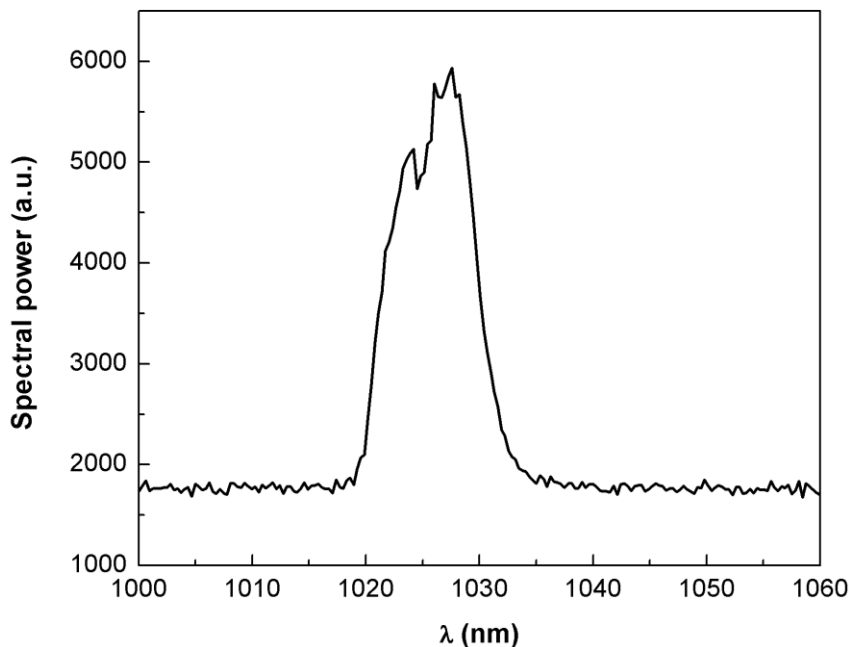


Figure 3.2: Spectrum of directly diode pumped Yb:KGW femtosecond laser PHAROS

The laser beam was delivered to the sample via dielectric mirrors (DM) (Figure 3.3). A set of irises (I1-I6) were placed to simplify the alignment procedure. After our laboratory was equipped with harmonic generation module “Hiro” some of the single dielectric mirrors were replaced with double line dielectric mirrors, which can effectively reflect both the fundamental and second harmonics. A small part of the laser light was directed into the pulse characterization setup via a beam sampler, BS1, designed for ultrafast light pulses. The average power of the laser irradiation incident on the sample was controlled with an attenuator made of a half-wave plate (HW1) mounted into a motorized rotation stage and a linear Glan polarizer. The rotation stage was first calibrated to find the precise relation between transmitted power and the angle of the rotation stage. Then the stage was controlled with a simple LabView program. Then depending on the used optics the laser beam diameter and collimation was manipulated with a telescope (comprised of two plano-convex lenses L1 and L2) to match the entrance aperture of the focusing optics. The second half-wave plate (HW2) was placed just before the focusing optics (MO) to control the incident polarization. In most of our experiments polarization played a crucial role, thus to increase the purity of incident polarization it was manipulated after passing all dielectric mirrors, just before the focusing optics. Finally, the light was focused via either an objective or aspheric lens into a sample that was mounted on an Aerotech ABL1000 computer controlled linear motor translation stages.

Previously, the sample was mounted vertically on two goniometers using melted wax. However, while assembling the new setup we chose a more ergonomic solution: mounting the sample on the horizontal platform. This resembles an upright microscope arrangement and helps to reduce to minimum the preparation process before the writing procedure and enabled the fabrication on samples of arbitrary geometry.

The whole set-up was controlled with Aerotech A3200 system and SCA software by Altechna Ltd. The writing process was additionally monitored via a home-made transmission microscope integrated into the writing system. The back illumination of the sample was performed with a fiber light source and a microscope long

working distance condenser. After the objective (MO) the light was collected with tube lens (L3). The additional lens (L4) was added to enable imaging of the plane where the laser focus is located. For each lens adjustment of L4 lens was required thus it was placed onto a mechanical translation stage. Finally the image was taken with a scientific CCD camera Retiga 2000, QImaging.

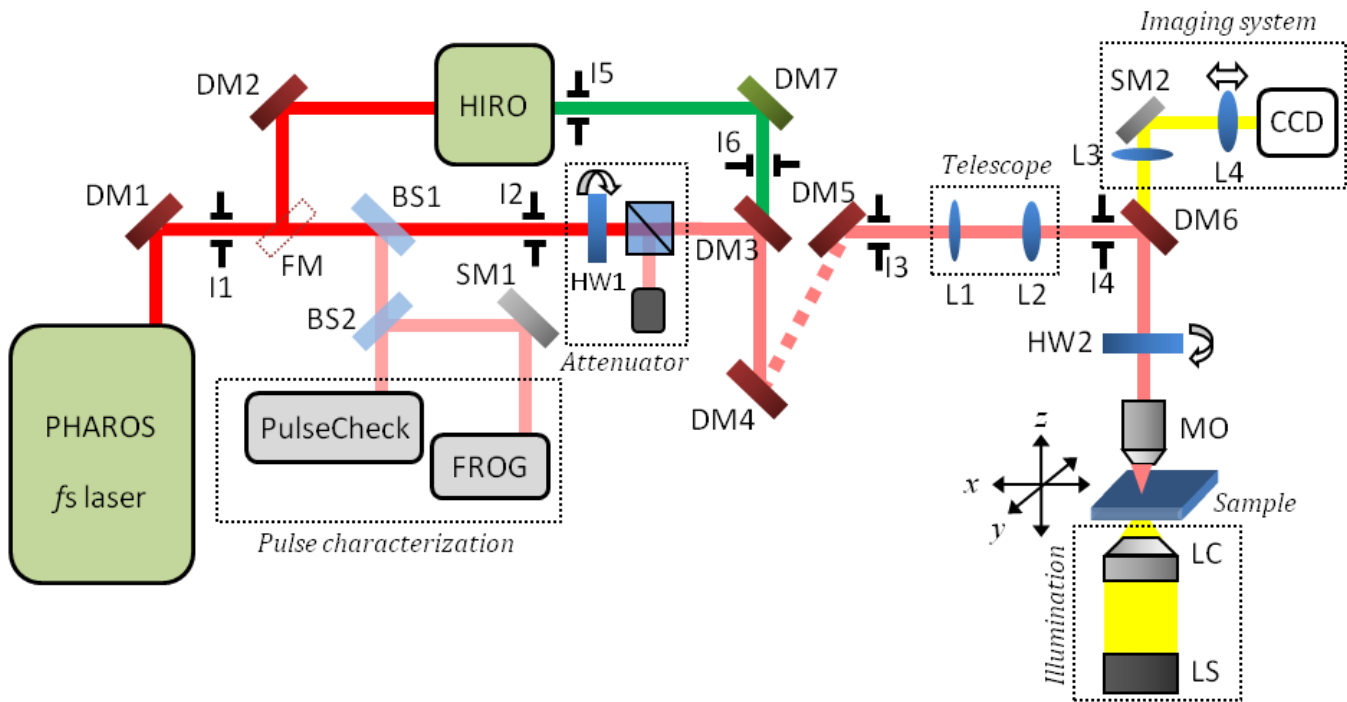


Figure 3.3: Femtosecond laser direct writing setup. DM – dielectric mirror, SM – silver mirror, I – iris, BS – beam splitter, L – lens, HW – half-wave plate, MO – microscope objective, LC – condenser, LS – light source.

The desired patterns were written in the bulk in the transparent material by moving the translation stage, while the laser was focused inside the sample. For the first experiments, the patterns were defined using translation stage programming language, G-code. Later, the set-up control was implemented with the SCA system, which allowed full control of translation stages, motorized rotation stage of the attenuator and the laser.

To ensure that the input surface of the sample was perpendicular to the writing beam the focusing optics were removed and the sample was replaced with a metallic mirror. The reflection from the mirror was then routed back the same way

as the incident laser beam through the system of partially closed irises. The final adjustments were made using the translation stage holding the objective.

3.1.1 Focusing optics

During my PhD work two different approaches were used for focusing the laser light into the sample. In the first approach, objectives designed for IR were used. The advantage of using microscope objectives is better light management over a broad band spectrum, which is not so crucial for the laser beam itself (an 8 nm bandwidth can be considered as monochromatic in this situation), but very important for the imaging system. Additionally, the microscope objectives used in our experiments possessed high numerical aperture and long working distance which have better focusing properties than simple spherical lenses eliminating unwanted spherical aberration if focused in the air.

It is important to mention that there was no tool to control spherical aberration which occur when focusing laser light in the bulk of the material. This optical effect is caused by the refractive index mismatch at the air/glass interface. The result of the spherical aberration is the shift of the focus in the vertical axis and its strong elongation. As the numerical aperture of the lens is increased the effect becomes even stronger. Some research groups compensate the index mismatch in their experiments using oil immersion objectives. The other solution is spatial light modulators, which would impose a desired phase onto the beam thus pre-compensating phase distortion at the sample surface.

3.2 Setup for the birefringence measurements

Investigation of the laser induced birefringence was one of the most important parts of sample characterization. The techniques used for characterization of birefringence stem from the field of biology, where polarization microscopy provides non-invasive method for the analysis of living organisms. Additionally, polarization microscopy can be used with birefringent or dichroic samples as a contrast enhancing tool. The traditional polarization microscope is made in the following way (Figure 3.4).

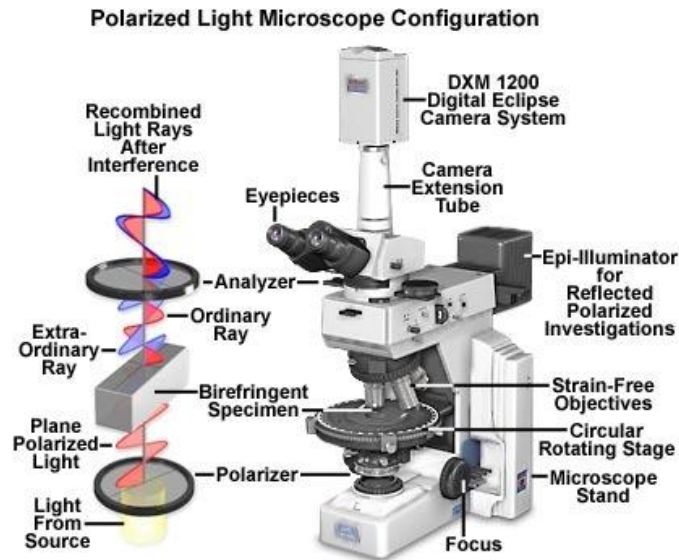


Figure 3.4: Traditional polarization microscope. The light from the bulb is polarized with a polarizer inserted below the condenser. After the light propagates through the sample it is collected with strain-free objectives and analyzed with an analyzer. Intensity variation of the specimen allows qualitatively investigate anisotropy of the specimen. Source: MicroscopyU and Nikon.

First, the microscope light source is linearly polarized with a polarizer, later it passes through the condenser, analyzed sample and microscope objective (which should be strain free, in order to avoid any background noise). Then the light is passed through the analyzer (another linear polarizer) which is mounted in a manual rotation stage to enable control of the transmission axis angle. The most typical arrangement is when the transmission axes of the polarizer and analyzer are in crossed position, then only birefringent parts of the sample are visible creating strong contrast in the image. This simple technique allows qualitative characterization of the sample. The quantitative analysis requires more elaborate measurements, which include several intensity measurements of a sample with different positions of the analyser. This introduces several problems such as the calibration of the measured signal, misalignment of the images and potentially long measurement procedure.

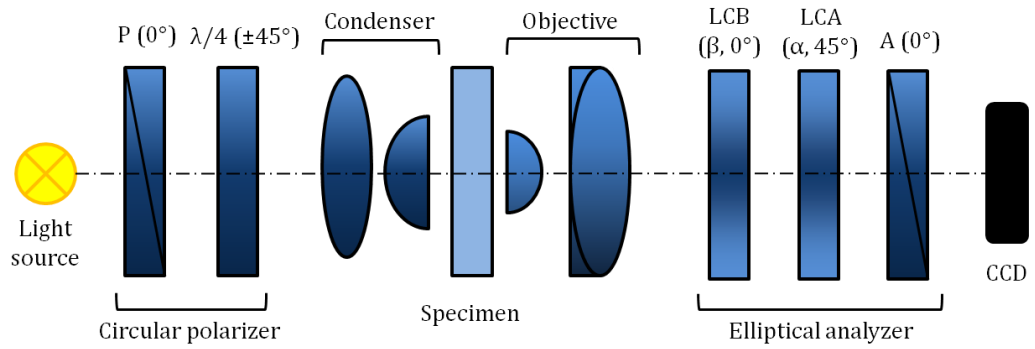


Figure 3.5: Optical scheme of PolScope (or Abrio) birefringence measurement system. The light emitted by the halogen lamp is initially circularly polarized and projected with the condenser onto the sample. The objective collects the transmitted light, which passes through the universal analyzer comprised of two liquid crystal variable retarders LCA and LCB with 45° between their principal axes and a linear polarizer A. Further the intensity signal is measured with a CCD camera. Source: M. Shribak and R. Oldenbourg [58].

The analysis of the obtained data also requires a lot of computation resources. These problems can be solved with the PolScope microscope, which is essentially the same polarization microscope with a modified polarizer and analyser (compensator) (Figure 3.5). In the PolScope system a linear polarizer is replaced with a circular one (comprised of a linear polarizer P and a quarter-wave plate), this simplifies further extraction of the data and excludes the possibility of undefined measurements when the polarization plane is oriented along the slow or fast optical axis. Another modification is the replacement of the analyser with a liquid crystal universal compensator, which excludes the image misalignment due to mechanical movement of the analyser. The universal compensator is built from two variable retarder plates (LCA and LCB) and a linear polarizer. The retarders are made of liquid crystals and can be controlled by a DC voltage supplied by an electronic controller connected to a personal computer. The PolScope also requires monochromatic light, thus the circular polarizer is combined with an interference filter, which transmits at 515 nm with 8 nm bandwidth. However, in principle any other wavelength can be used for measurements after recalibration of the universal compensator.

In the special case when the second cell LCB has quarter-wave retardance ($\beta = \lambda/4$), the elliptical polarizer operates as a linear polarizer with a variable

azimuth. The polarization direction equals half of the retardance, in degree, to which the first cell LCA is set.

Let us assume that the analyzed sample has a distribution of retardance $R(x, y)$ and of slow axis azimuth $\phi(x, y)$. Then the intensity recorded by the CCD camera is:

$$I(\alpha, \beta, x, y) = \frac{1}{2} \tau(x, y) I_{max}(x, y) [1 + \sin \alpha \cos \beta \cos R(x, y) - \sin \alpha \sin \beta \cos 2\phi(x, y) \sin R(x, y) + \cos \alpha \sin 2\phi(x, y) \sin R(x, y)] + I_{min}(x, y). \quad (3.1)$$

Here $I_{max}(x, y)$ is the distribution of the illumination intensity on the sample and $\tau(x, y)$ is the distribution of the isotropic sample transparency. The $I_{min}(x, y)$ describes the distribution of the depolarized background arising due to imperfect polarizers. It also accounts for the offset of electronic signal on the CCD camera. The α and β are retardance values for LCA and LCB retarders respectively. The measurement of retardance $R(x, y)$ and slow axis direction $\phi(x, y)$ are performed by measuring a series of intensity images for different α and β values.

A set of intensity images (I_1, I_2, I_3, I_4, I_5) are generated by adding a swing value χ to the nominal values of the retarders $\alpha = \lambda/4$ and $\beta = \lambda/2$:

$$\begin{aligned} 1: & \quad \alpha = \frac{\lambda}{4}; \beta = \frac{\lambda}{2} \\ 2: & \quad \alpha = \frac{\lambda}{4} - \chi; \beta = \frac{\lambda}{2} \\ 3: & \quad \alpha = \frac{\lambda}{4} + \chi; \beta = \frac{\lambda}{2} \\ 4: & \quad \alpha = \frac{\lambda}{4}; \beta = \frac{\lambda}{2} - \chi \\ 5: & \quad \alpha = \frac{\lambda}{4}; \beta = \frac{\lambda}{2} + \chi \end{aligned}$$

Then two parameters, A and B, can be calculated:

$$A = \frac{I_2 - I_3}{I_2 + I_3 - 2I_1} \tan \frac{\chi}{2} = \sin 2\phi \tan R, \quad (3.2)$$

$$B = \frac{I_5 - I_4}{I_5 + I_4 - 2I_1} \tan \frac{\chi}{2} = \cos 2\phi \tan R. \quad (3.3)$$

Finally the retardance and azimuth can be found as:

$$R = \frac{\lambda}{2\pi} \arctan \sqrt{A^2 + B^2} \quad (3.4)$$

$$\text{when } I_2 + I_3 - 2I_1 \geq 0,$$

$$R = \frac{\lambda}{2\pi} \left(\pi - \arctan \sqrt{A^2 + B^2} \right) \quad (3.5)$$

$$\text{when } I_2 + I_3 - 2I_1 < 0,$$

$$\phi = \frac{1}{2} \arctan \left(\frac{A}{B} \right). \quad (3.6)$$

Retardance values higher than $\lambda/2$ are measured ambiguously. For instance if the retardance of the sample is in the range $\lambda/2 < R_{sample} < \lambda$, the measured retardance is the $R = \lambda - R_{sample}$ and the slow axis angle is rotated by 90° . This is very important for laser induced birefringence and especially for characterization of polarization devices, where frequently the retardance value exceeds $\lambda/2$ (257 nm). The ambiguity can be partially solved by noticing that the measured slow axis angle is perpendicular to the expected one and thus the correction of the retardance value should be made. If this problem plays a very important role, phase unwrapping techniques might be applied for the polarization measurements.

The measurements with PolScope are taken and analysed with the commercial software Abrio. For a single birefringence measurement four intensity images have to be taken. The images are taken with different values of the variable retarders. The commercial software is used to extract and analyse the data. Some of the data was extracted and analysed with Matlab using the dynamic library for reading raw PolScope files. The advantage of using Matlab is the simplified analysis of a huge amount of data and the ability to extract additional information such as a measurement error and spatial variation of the measured parameters.

3.3 Digital holographic microscope

Another technique used to characterize photo-induced phase change is digital holography microscopy. This technique is based on a Mach-Zehnder interferometer (Figure 3.6).

The sample is placed in one arm of the interferometer. The hologram at the exit of the interferometer is created by the interference between the object wave $\mathbf{O}(x, y)$ and reference wave $\mathbf{R}(x, y)$. The hologram intensity

$$I_H(x, y) = |\mathbf{R}|^2 + |\mathbf{O}|^2 + \mathbf{R}^* \mathbf{O} + \mathbf{R} \mathbf{O}^* \quad (3.7)$$

is recorded with a CCD camera and processed with a computer to obtain the digital hologram:

$$I_H(k, l) = I_H(x, y) \text{rect} \left(\frac{x}{L}, \frac{y}{L} \right) \times \sum_k^N \sum_l^N \delta(x - k\Delta x, y - l\Delta y), \quad (3.8)$$

where k and l are integers $\left(-\frac{N}{2} \leq k, l \leq \frac{N}{2}\right)$, Δx and Δy are the sampling intervals in the hologram plane $\left(\Delta x = \Delta y = \frac{L}{N}\right)$, L is physical dimension of the CCD matrix and N is number of pixels.

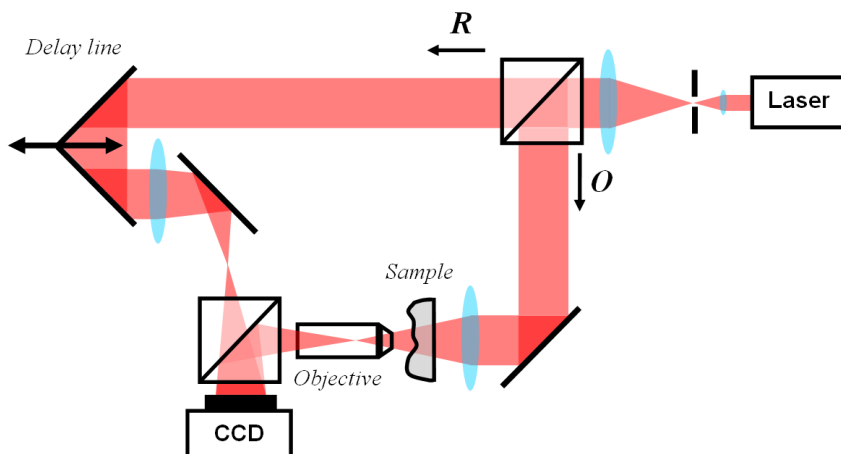


Figure 3.6: Digital holography microscopy working in transmission mode. The delay line is used to compensate optical path difference for object (\mathbf{O}) and reference (\mathbf{R}) waves. Source: www.lynceetec.com

The reference wave is then digitally propagated through the obtained digital hologram and the object is reconstructed and thus the phase is extracted. The advantage of this method is that the phase is measured from the single image, which allows continuous monitoring of the sample. Phase measurements for both methods are essentially identical, except for birefringent samples. QPM uses a non-polarized white light source, while DHM needs a laser diode. An integrated half-wave plate in the DHM system allows measuring the phase for different linear polarization azimuths, the measurements can then be combined to obtain quantitative birefringence measurement. The DHM system can also be enhanced by adding third branch to the interferometer, this enables the interfering of two perpendicular polarizations with the object wave and thus measure birefringent properties from the single image [27, 28].

Chapter 4. High average power second harmonic generation in air

4.1 Introduction

The optical breakdown observed in various transparent media, gases, liquids, transparent solids, is essentially the same phenomena occurring as a result of high laser intensity induced absorption. The laser induced absorption is similar for all substances. The wake of the ultra-short pulse induces free electrons via multi-photon absorption which are later heated via inverse bremsstrahlung and trigger avalanche ionization. The simplest medium for optical breakdown analysis is a gas. The various parameters of the gas can be easily controlled during the experiment including density, temperature and pressure. Additionally, a number of different phenomena observed in gaseous media have useful applications including X-ray [63], attosecond and single cycle pulse generation and terahertz emission [64].

The most accessible gaseous medium is ambient air, which is essentially a mixture of nitrogen (fractional content 78%, ionization potential 16 eV) and oxygen (fractional content 21%, ionization potential 12 eV). Depending on the focusing conditions and laser intensities several nonlinear effects can be observed in this medium. At high intensities and relatively loose focusing filamentation conditions can be achieved. At moderate conditions mostly third harmonic is analysed. The second harmonic in air can be generated only if inversion symmetry is broken. Such conditions can be created with tight focusing of ultra-short laser pulses.

Most of the experiments on gas ionization are carried out with relatively low NA optics. This results in strong self-focusing of the laser beam and filamentation in the case of ultra-short laser pulses. Similarly, the second harmonic generation in gaseous media or metal vapour were carried out by focusing high energy pulses with low numerical aperture (NA) optics [65,66] i.e. single lenses with focal length of several centimetres. Fedotov et al [65] reported second and third harmonic generation using 1 kHz 90 fs light pulses focused in a 25-30 μm diameter spot. The third harmonic conversion efficiency was about three orders of magnitude higher

than that for the second harmonic. Thus in loose focusing conditions third harmonic generation is a dominant process. The red halo present from 0.5 W indicated onset of the self-phase modulation. We however attempted to recreate tight focusing conditions similar to direct-writing in transparent solid medium. We demonstrated second harmonic generation in atmospheric pressure ambient air using tightly focused femtosecond laser beam with linear and circular polarizations. A conversion efficiency of 4×10^{-6} was achieved, corresponding to two orders of magnitude increase in normalized efficiency (which here is defined as efficiency divided by the pump peak power) and average second harmonic power compared to that previously reported [66]. Additionally, we demonstrated second harmonic generation enhancement with external gas flow, increasing the conversion efficiency by about 20 times. The second harmonic generation mechanism is explained in terms of the pondermotive force induced free electron gradient. Further, generation of a second harmonic optical vortex in accordance with angular momentum conservation law is demonstrated. The circularly polarized ring-shaped beam of the second harmonic is generated in the air by a fundamental beam of the same circular polarization, while the linear polarized beam produces a two-lobe beam at the second harmonic frequency.

4.2 Generation of second harmonic in isotropic material

If the laser intensity is high, the polarization of the material exhibits a nonlinear dependence on the applied electric field:

$$\mathbf{P} = \varepsilon_0 [\tilde{\chi}^{(1)} \mathbf{E} + \tilde{\chi}^{(2)} \mathbf{E} \mathbf{E} + \tilde{\chi}^{(3)} \mathbf{E} \mathbf{E} \mathbf{E} + \dots] \quad (4.1)$$

where $\tilde{\chi}^{(n)}$ is the n-th order nonlinear susceptibility.

Under the linear dipole approximation, second harmonic generation (and all other higher order even terms) is forbidden in centrosymmetric media due to inversion symmetry. The symmetry can be broken by adding an external electric field \mathbf{E}_{DC} , then second order susceptibility can be expressed as:

$$\tilde{\chi}^{(2)} = \tilde{\chi}^{(3)} \mathbf{E}_{DC}. \quad (4.2)$$

Alternatively, an electric field can be generated by the gradient of the intense laser beam thus excluding the necessity of external field application [67]. It has been demonstrated that in isotropic gaseous media, under radiation forces photoelectrons [68] can also give rise to the frequency doubling [69], which is otherwise forbidden under the dipole approximation.

Two mechanisms can give rise to the nonzero gradient of the electron concentration [70]. The first one is due to the inhomogeneous distribution of the electron density produced by the Gaussian fundamental beam in the focal area. We assume that at our laser intensities the ionization is saturated and the ionized region is bigger than the pump spot size, thus this mechanism does not explain the observed second harmonic generation. The second mechanism is based on the pondermotive force,

$$\mathbf{f}_e = -\frac{e^2}{4m\omega^2}\nabla_{\perp}E^2 \quad (4.3)$$

where ∇_{\perp} is the gradient of the electric field perpendicular to the beam propagation direction. This force is directed out of the centre of the pump and thus creates an inhomogeneous distribution of electrons pushing them from the centre of the focused beam and gives rise to the second harmonic.

Frequency doubling in the isotropic plasma with density η_e can be described in terms of the second-order polarization [68,71]:

$$\mathbf{P}(2\omega) = \chi \left((\mathbf{E} \cdot \nabla)\mathbf{E} + \frac{i\omega}{c}\mathbf{E} \times \mathbf{B} \right) + \frac{e\mathbf{E}(\nabla \cdot \mathbf{E})}{8\pi m\omega^2}, \quad (4.4)$$

where $\chi = \frac{\eta_e e^3}{4m^2\omega^4}$. By using the condition of the plasma neutrality $\nabla(\epsilon_p \mathbf{E}) = 0$, where $\epsilon_p = 1 - \frac{\omega_p^2}{\omega^2}$ is the plasma dielectric constant and $\omega_p = \sqrt{\frac{4\pi\eta_e e^2}{m}}$ is the plasma frequency, Equation 4.4 can be written as [68]:

$$\mathbf{P}(2\omega) = \chi \left[\frac{1}{2}\nabla E^2 + \frac{2(\mathbf{E} \cdot \nabla \ln \eta_e)\mathbf{E}}{\epsilon_p} \right]. \quad (4.5)$$

In the non-uniform plasma, the second term on the right-hand-side dominates the second harmonic generation [68], i.e. the second harmonic beam will be co-polarized with the fundamental one. Therefore, since in the cylindrically symmetric fundamental beam $\nabla\eta_e$ is perpendicular to the propagation direction, the linearly polarized fundamental beam produces second harmonic radiation in the form of two lobes (Figure 4.1). The lobes are oriented along the polarization azimuth and with electric field phase shifted by π with respect to one another. The circularly polarized fundamental beam produces the second harmonic radiation, which is co-circularly polarized and forms a ring around the beam axis (Figure 4.1).

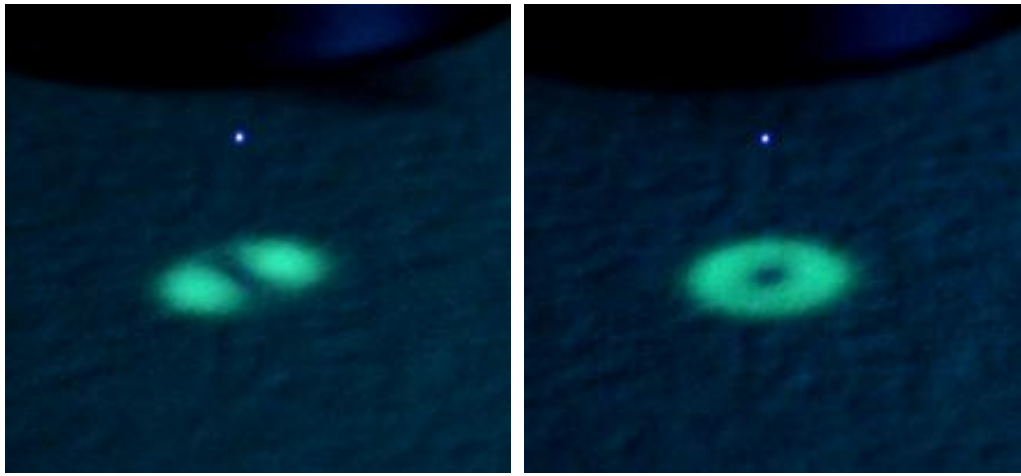


Figure 4.1: Second harmonic generated in air by tightly focused femtosecond laser pulse with linear (left) and circular (right) polarizations. The white spot is plasma glow at the focus of the objective.

The latter case is particularly interesting and deserves further insight because of the restrictions imposed by the momentum conservation law. Specifically, in the second harmonic generation process, a pair of the photons of the fundamental beam with angular momentum $2\hbar$ creates only one SH photon with angular momentum \hbar (Figure 4.2). Thus the remaining angular moment should be either transferred to the plasma in the focal area or to the orbital angular momentum of the SH beam creating an optical vortex [72,73]. However, the ring shaped pattern (typical for Laguerre–Gaussian TEM_{01}^* mode) observed in the far-field strengthens the assumption of a phase singularity presence and an optical vortex generation.

The circular polarization of the second harmonic was confirmed by placing a linear polarizer in the second harmonic beam. This led to the signal decrease by a half and was independent of the polarizer orientation. This observation coincides with the results on second harmonic generation in helium gas [70].

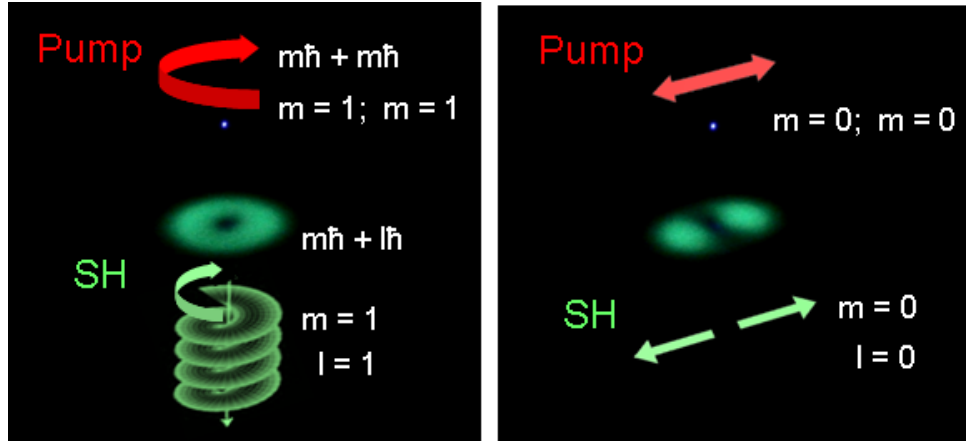


Figure 4.2: Second harmonic vortex generated with circularly polarized pump in accordance with angular momentum conservation (Left). Two-lobe second harmonic pattern with π shifted electric fields for linearly polarized pump (Right).

4.3 Experimental set-up

Experiments were performed with a Yb:KGW (Yb-doped potassium gadolinium tungstate) based femtosecond system (Pharos, Light Conversion Ltd.) that delivered pulses of 270 fs with a repetition rate of 200 kHz at 1025 nm. The power delivered to the focus was varied from 0.15 W to 2.5 W with an achromatic half-wave plate and Glan polarizer (Figure 4.3). The linear polarization of the incident beam was rotated with the second achromatic half-wave plate, which was replaced with an achromatic quarter-wave plate when circular polarization was studied. The beam after being reflected from a dichroic mirror was focused to about 940 nm diameter spot with an infinity-corrected objective (Mitutoyo $\times 100$ 0.7 NA M Plan Apo NIR HR). This is about 30 times smaller spot size than used in previous experiments of second harmonic generation in ambient air [65,66]. The Rayleigh range is about 670 nm, thus we can roughly assume interaction length of 1.3 μm . Consequently, the maximum radiation intensity in the focal spot was $6 \times 10^{15} \text{ W/cm}^2$ at 2.5 W (i.e. it was above the air ionization threshold of about

$\sim 10^{14}$ W/cm² [66]) producing plasma with a concentration of about 10^{17} cm⁻³. The low absorption of the transmitted laser pulses confirmed that the induced plasma was well below critical concentration.

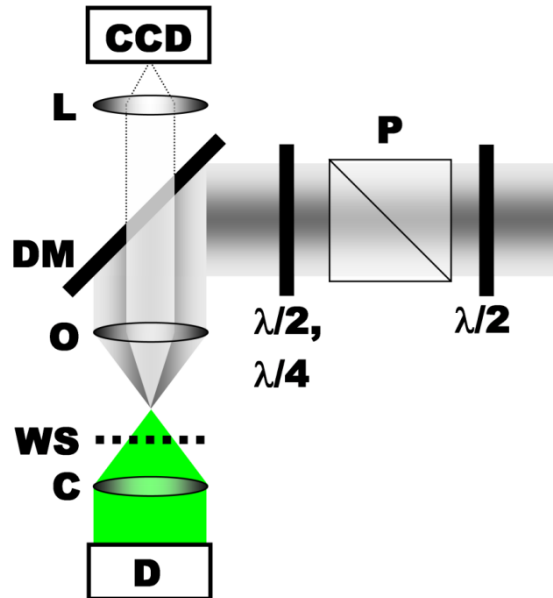


Figure 4.3: Experimental setup for generating second harmonic in air: Half-wave plate and Glan polarizer (P), dichroic mirror (DM), objective (O), condenser (C), CCD camera (CCD), white screen (WS), power meter (D). (Insert) Image of SH pattern for circular polarization. On top of the photography the objective's edge can be seen.

Additionally, the effect of focusing on the second harmonic generation was investigated using objectives with lower NA (0.2 and 0.55). Light after the focus was collected with microscope condenser. The focal spot was observed through dichroic mirror with a CCD (coupled-charge device) camera.

4.4 Experimental results

Once the laser beam was focused with the objective a small bluish spherical spot appeared in the focus with coherent green light viewed on a white screen placed after the beam focus (Figure 4.1). The spectral analysis confirmed that the observed green light was the second harmonic of the fundamental laser frequency (Figure 4.4). The shape of the second harmonic pattern depended on the fundamental beam polarization. Linear polarization produced two lobes aligned along the polarization direction. For the circular polarization light the doughnut

shape was observed. We observed a quadratic dependence of the second harmonic generation on fundamental beam power with an approximately 1.4 times stronger signal for circular polarization (Figure 4.5). The estimated maximum second harmonic conversion normalised efficiency was about 4×10^{-6} .

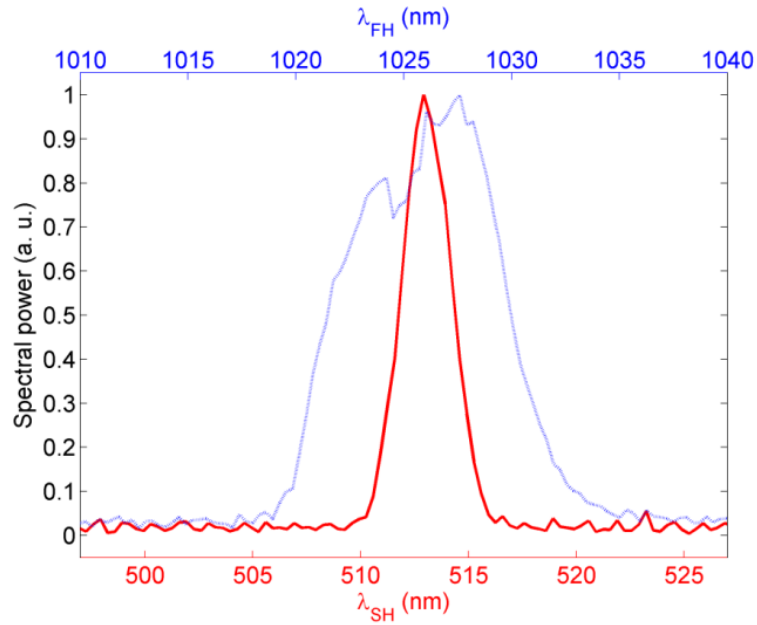


Figure 4.4: Spectra of the first and second harmonics measured with an Avantes spectrometer.

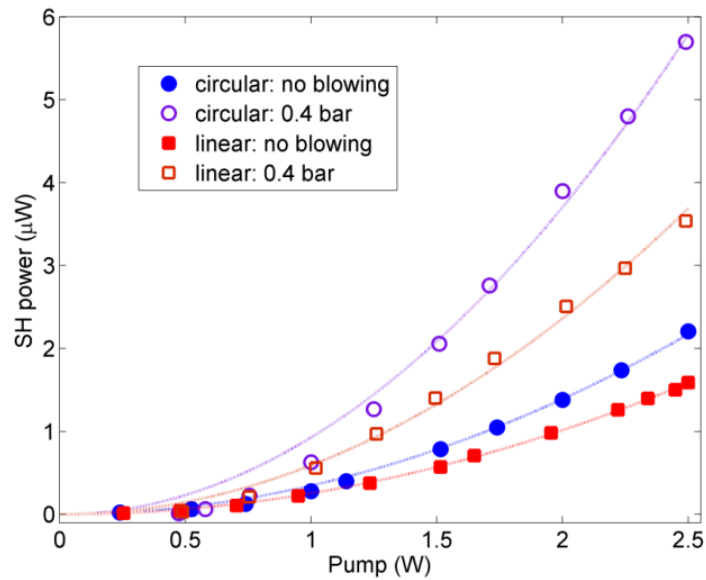


Figure 4.5: Second harmonic power as a function of the pump power. Dashed lines show fit of data with quadratic function.

The third harmonic visualized via blue luminescence on the paper screen was much weaker than the second harmonic signal. This can be explained by the fact that a circularly polarized fundamental beam cannot produce third harmonic radiation in an isotropic medium and the tight focusing of the pump. Only when the fundamental beam was focused with lower NA objectives and linearly polarized, we did manage to observe blue luminescence, indicating the presence of the third harmonic. This demonstrates crucial role of NA in the second harmonic generation in air.

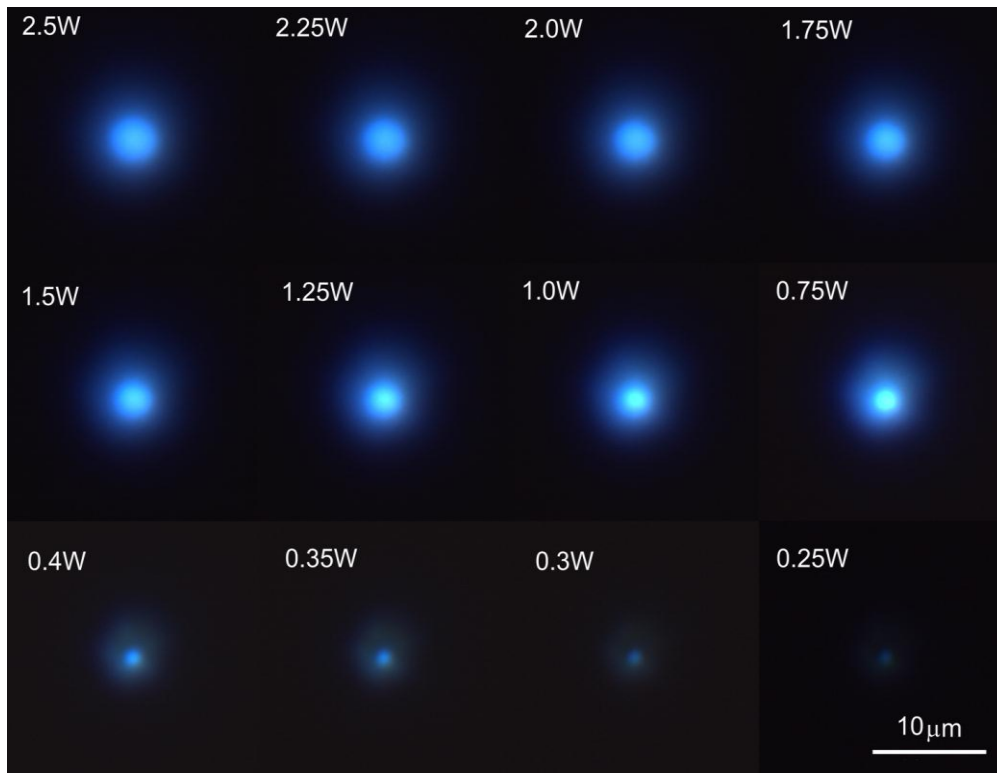


Figure 4.6: CCD images of plasma spot evolution with pump power increase. Numeric values indicate pump power delivered to the focus.

The power of the fundamental beam measured behind the focal plane was a linear function of the incident power, with the same slope for linear and circular polarizations. This indicates negligible plasma absorption.

The diameter of the ionized area d_{FWHM} was estimated by fitting the Gaussian function to the spot profile measured with the CCD camera (Figure 4.7). It increased with pump power from about $1.8 \mu\text{m}$, corresponding to the spot size in the focus, to $4.6 \mu\text{m}$ (Figure 4.6). For the circular polarization d_{FWHM} was about 7%

smaller than for the linear polarization. This change, however, did not affect the second harmonic far field pattern size supporting our assumption of the pondermotive force being responsible for the observed frequency doubling.

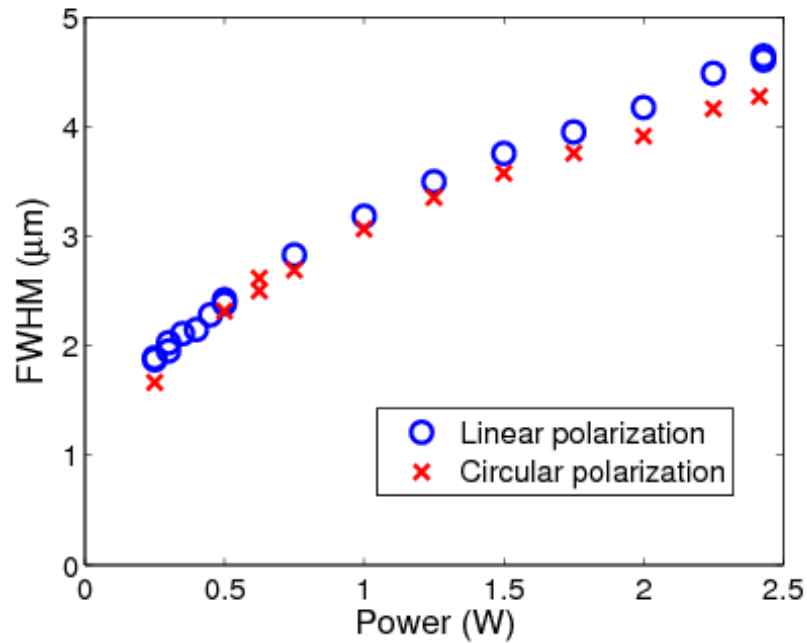


Figure 4.7: Plasma spot diameter d_{FWHM} dependence on pump power evaluated from the images taken with a CCD camera.

Another interesting observation was a significant (about 3 times) growth of the second harmonic signal accompanied by a plasma spot diameter and intensity increase when a weak stream of nitrogen gas (Figure 4.8), or compressed air was pointed at the focal area. The increased intensity of the plasma glow indicates that electrons acquire higher energy during laser irradiation, which might be explained by the earlier onset of the ionization or increased concentration of the atoms. The strong signal increase was observed at pressure below 0.1 bar (the lowest pressure measurable with our set-up). Yet a higher gas pressure had produced a merely several percent additional increase in the second harmonic signal. The nitrogen stream was accompanied with a yellow-orange light tail (emerging from plasma spot and pointing in the direction of gas flow) and a strong odour typical for nitrogen dioxide (NO_2). This glow can be attributed to chemiluminescence – emission of energy as a result of the chemical reaction of oxygen and nitrogen ionized by ultrashort laser pulses.

An even stronger effect was noticed with compressed a hydrofluorocarbon (HFC) gas flow from an air duster (Figure 4.8). This time the twenty- and four-fold increase of the second harmonic signal was measured at pump powers of 0.65 W and 2.45 W, respectively. Consequently, the measured power of signal was as high as 10 μ W. An additional sharp peak was observed in the wake front of second harmonic power. If, however, the laser beam was physically interrupted, while gas was blowing, the second harmonic signal wake front was without this peak. Currently, the origin of this peak needs to be further investigated.

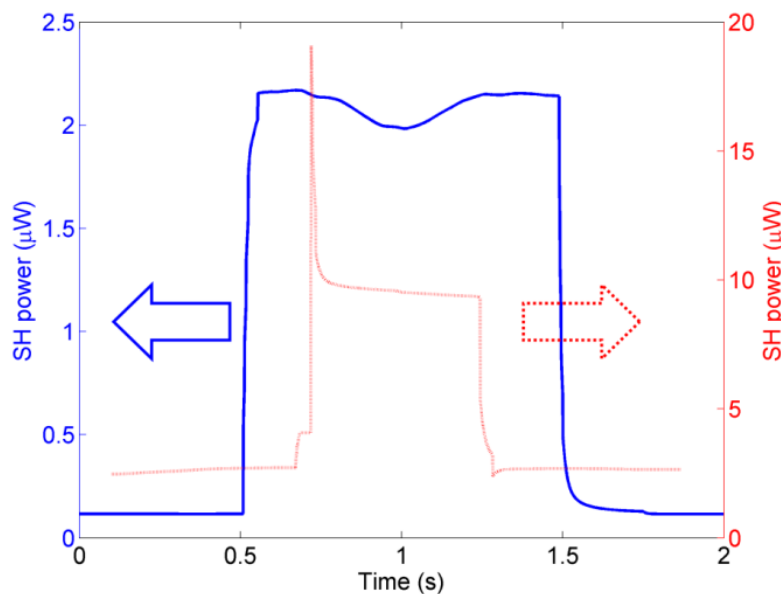


Figure 4.8: Second harmonic power change when compressed HFC gas is blown at the focus spot for two pump powers. The second harmonic increases about 20 times at 0.65 W pump power (blue) and about 4 times at 2.45 W (red).

The described above phenomenon also supports the assumption that the pondermotive force dominates the second harmonic generation process. Indeed, the pondermotive force pushes electrons until attraction between separated positive and negative charges counterbalance this force. The external gas flow drags positive ions out of the focus weakening the electric field strength and leading to a stronger electron concentration gradient and thus to the enhanced second harmonic emission. Alternatively, the gas stream directed to the focal point of the laser can serve as a free electron source. The avalanche can then start much earlier without multiphoton absorption which normally seeds the initial free electrons. This could also explain why harmonic enhancement was so sensitive to a

small amount of gas flow and strongly depended on the gas which was blown. The HFC might be easier to ionize and thus easier to create more electrons.

4.5 Conclusions

We presented a method for high average second harmonic generation in ambient air. The ultrashort laser pulses were tightly focused into the medium so that the threshold intensities are reached with relatively low pulse energies and thus no filamentation or self-phase modulation was observed. Assuming an interaction length of about 2 μm , we estimate the effective second order nonlinearity in our experimental conditions was 0.03 pm/V, which is of the same order as in poled silica fibres [74,75]. Increasing the interaction length, e.g. using a specially designed capillary or a photonic crystal fibre (PCF) [76], can result in practical conversion efficiencies in excess of 50%. However, the issue with the optical damage of photonic crystal fibres arises. It was demonstrated that pulses with intensities of 10^{14} W/cm² can be transferred in a PCF [77]. Thus is one order lower than used in our experiments. The interaction length could partially compensate reduced intensity. The limit of interaction length will also occur as a result of laser induced plasma absorption. Alternatively, the interaction length can be also increased by tightly focusing a Bessel beam instead of Gaussian [78]. The Bessel beams possess a much longer Rayleigh range, thus effectively increasing the interaction length. On the other hand, at a longer interaction length phase mismatch occurring for the fundamental and second harmonic have to be compensated. For instance, this can be achieved by period modulation of the gas concentration induced with acoustic waves.

In the course of the experiments we observed strong dependence of second harmonic generation on the external flow of gas. The second harmonic emission could be enhanced 20 times by utilising HFC gas found in an air duster.

We also speculate that the circular polarization of fundamental beam should produce an optical vortex in the second harmonic as a result of angular momentum conservation. The experimentally observed doughnut shape of second harmonic confirms spin-to-orbit momentum coupling.

The described second harmonic generation method is particularly interesting for deep UV generation where the use of nonlinear crystals such as beta barium borate (b-BaB₂O₄ or BBO) is restricted.

Chapter 5. Effect of edge birefringence

5.1 Introduction

An transparent isotropic sphere is one of the simplest optical elements. Yet, despite its simplicity, it found multiple applications and played an important role in one of the first microscope design. It was Antoni van Leeuwenhoek (1632–1723), a Dutch merchant, who designed his microscopes based on glass sphere. His microscope design allowed to achieve useful optical magnification of ~ 200 times, far surpassing his contemporaries [79]. Glass balls can be also used as a cost effective solution to couple light into optical fibre [80]. Small glass spheres have found application for road signs and license plates, where they are mixed with paint to enhance retro-reflectivity. Recently, sub-diffraction limit imaging was demonstrated where silica micro-spheres [81] were utilized as magnifying lenses thus resembling the idea of van Leeuwenhoek microscope.

We propose another application of a transparent isotropic sphere: a radial polarizer based on light refraction. We demonstrate theoretically and experimentally that as a result of the space variant Fresnel reflection/transmission coefficient at the interface of two dielectric media the circularly polarized light impinging on the sphere produces a double charged optical vortex. The superposition of two circularly polarized waves also leads to the generation of a radially polarized vortex. The experimental demonstration is implemented with a femtosecond laser enabling micro-sphere formation in the bulk of the fused silica. As a result of edge birefringence optical vortices were generated on a small scale using hollow micro-spheres in fused silica.

5.2 Radial edge birefringence

Let us consider a circularly polarized light incident on an interface of two media with different refractive indices, n_1 and n_2 . As a result of differential transmission, transmitted light is elliptically polarized with its major axis directed perpendicular

to the interface and can be analyzed as superposition of linear \mathbf{E}_{linear} and circular $\mathbf{E}_{circular}$ polarizations:

$$\mathbf{E}_{REF} = (t_p(\theta) - t_s(\theta)) \cdot \mathbf{E}_{linear} + t_s(\theta) \cdot \mathbf{E}_{circular}, \quad (5.1)$$

where t_p, t_s are the Fresnel transmission coefficients for p and s polarized light and θ is the angle of incidence. In the explicit form one can write:

$$t_p(\theta) - t_s(\theta) = \frac{2 \left(\frac{n_1^2}{n_2^2} - 1 \right) a(\theta) \cos \theta}{\frac{n_1}{n_2} (\cos^2 \theta + a^2(\theta)) + \left(\frac{n_1^2}{n_2^2} + 1 \right) a(\theta) \cos \theta}, \quad (5.2)$$

where

$$a(\theta) = \sqrt{1 - \left(\frac{n_1}{n_2} \sin \theta \right)^2}. \quad (5.3)$$

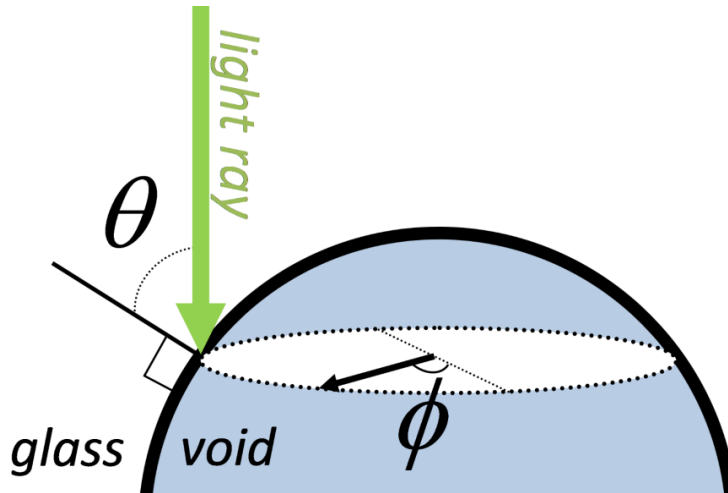


Figure 5.1: Schematic representation of light ray impinging a void embedded in glass.

Due to a high degree of symmetry, a sphere adds an azimuthal angle as an additional degree of freedom. Thus, for interfaces of spherical shape the transmitted and reflected light will be partially polarized (see Equation (5.2)) correspondingly in radial and azimuthal directions. This partial polarization occurring at the interface of two media with different refractive indices is caused by edge birefringence [82]. It is called edge birefringence as is observed only close

to the edge of the medium. Also its strength depends on the refractive index difference, the higher it is, the stronger is the edge birefringence.

In the Rayleigh range the light wave front is flat, the polarizing effect of the spherical shape can be approximated as a radial polarizer and described by the following Jones matrix:

$$M = \begin{pmatrix} \cos^2 \phi & \cos \phi \sin \phi \\ \cos \phi \sin \phi & \sin^2 \phi \end{pmatrix}, \quad (5.4)$$

where ϕ is the polar angle. After refraction \mathbf{E}_{linear} (the incident field is left circularly polarized, $\mathbf{E}_{IN} = \mathbf{E}_{LCP} = E_0[1, i]$) can be written as:

$$\mathbf{E}_{linear} = M \cdot \mathbf{E}_{IN} = \frac{1}{2}E_0 e^{i2\phi} \begin{pmatrix} 1 \\ -i \end{pmatrix} + \frac{1}{2}E_0 \begin{pmatrix} 1 \\ i \end{pmatrix}. \quad (5.5)$$

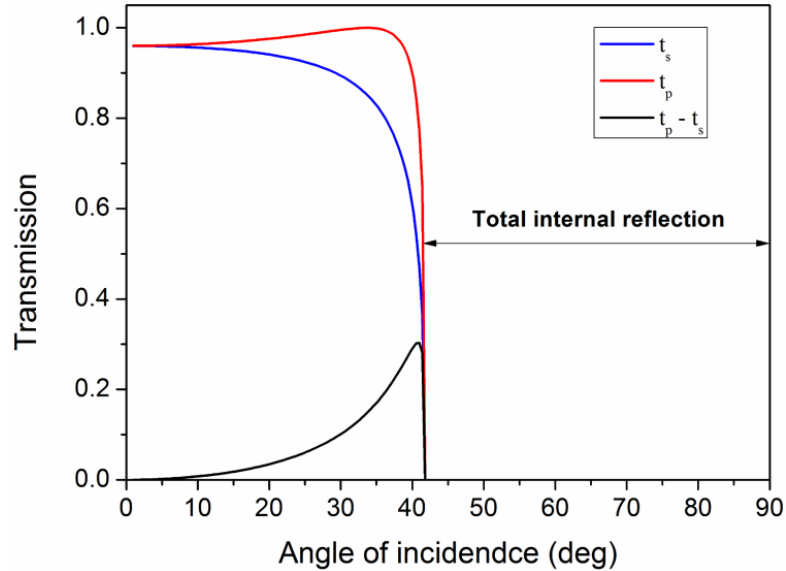


Figure 5.2: (Right) Transmission at the glass/air interface for s and p polarized light versus angle of incidence θ . The black curve represents differential transmission, which in the case of incident circular polarization produces partially linear (p) polarization.

Hence, the incident beam after passing the radial polarizer splits into two circularly polarized waves of opposite handedness. The wave, which retains the state of incident polarization, has a plane wave front. However, the other one acquires an explicit $e^{i2\phi}$ phase factor, indicating the presence of a phase singularity and associated OAM $l = 2\hbar$. As a result, the beam transforms into a circularly polarized optical vortex. This is confirmed by our modelling based on the

Jones matrix formalism (Figure 5.3). Indeed, the ability of a radial polarizer to generate optical vortex was demonstrated by several groups in 2006 [83,84]. This phenomenon, often referred as spin-to-orbit coupling, requires the interaction of light with matter that is both optically inhomogeneous and anisotropic. The underlying physics is also associated with the so-called Pancharatnam-Berry geometrical phase that is involved in any space variant transformation of the optical polarization. This can be achieved via dichroism (as shown in this chapter) or birefringence (as discussed in Chapter 8).

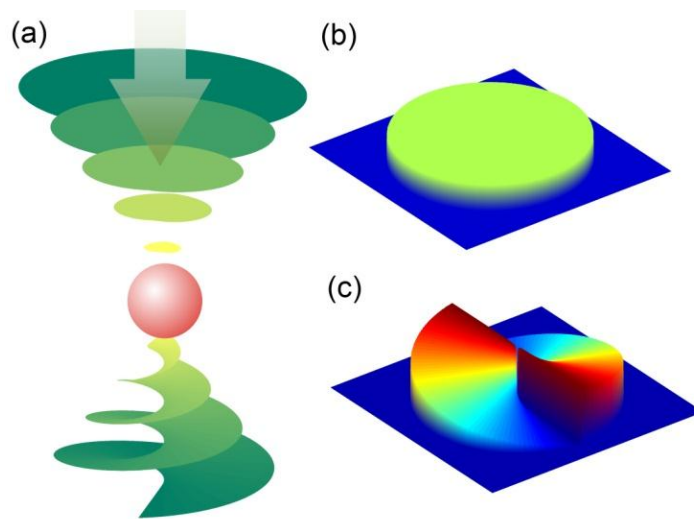


Figure 5.3: (a) Optical vortex generation on an isotropic sphere. Incident circularly polarized light with plane front ($l = 0$) after refraction on a spherical surface is partially converted into an optical vortex with the orbital angular momentum $l = 2\hbar$. (b, c) Modelled wave-front profiles of incident and transmitted electric field modelled using the Jones matrix formalism.

Right-hand circularly polarized beam after passing through the sphere will acquire OAM $l = -2\hbar$. Therefore, the input polarization determines the sign of the output OAM. Superposition of two circularly polarized waves, to which the incident beam splits, yields a vortex with radial distribution of electrical field polarization and non-zero intensity at the centre. The optical vortex and plane wave can be separated by a combination of a quarter-wave plate and linear polarizer, which serve as a circular polarizer.

5.3 Bubble formation in fused silica with femtosecond laser pulses

In fused silica, bubbles can be formed in several regimes with a femtosecond laser. In fact, internal cavity (a bubble or a void) formation in transparent materials at ultrashort irradiation regimes is a complicated multiphysics phenomenon, resulting from the generation of localized dense plasmas whose recombination brings matter into a highly stressed state. The geometry of the heat-affected region and the matter state in this region (softened, molten, or ionized vapour) depend on the irradiation parameters among which the focusing geometry plays an important role. Focusing femtosecond laser pulses with an oil immersion lens can lead to a single void creation [40,44,85]. An important feature of these voids is that they are created without excessive cracking of the surrounding medium, frequently seen after the irradiation with longer laser pulses. Another situation, where spherical objects with a femtosecond laser can be created, is high repetition rate (>1 MHz) and high scanning speed (>1 mm/s). Heat accumulation present at these high repetition rates leads to the formation of pearl-like chains inside the glass [86,87]. If multiple laser pulses are delivered to a single location, self-organized arrays of bubbles can be formed along the light propagation direction [88–90]. The last case will be considered more thoroughly as it is closely related to our experimental conditions. Kanehira et al. [89] reported the formation of long bubble chains after the multiple pulse irradiation in the case of deep focusing and proximity of the laser focus to the exit surface of the sample. After a single laser pulse only a filamentary track could be observed, however further irradiation leads to bubble formation at the surface of the sample, which triggered the formation of multiple bubbles towards the laser focus. This phenomenon can be closely related to a fiber fuse, then the periodic damage propagates upstream within an optical fiber [91]. The requirement for deep focusing might be related to the high numerical aperture used in these experiments. As it was shown in Paragraph 2.3.2, the uncompensated spherical aberration can lead to filament like channels for large focusing depths. Another group reported bubble chain formation inside of the glass sample without the presence of the interface [90]. In this case the formation of the bubble chain

was explained by oscillations of laser intensity caused by spherical aberration. However, material processing with ultrashort pulses is a highly nonlinear process. If nonlinearities are taken into account, modulation which could produce bubbles is strongly reduced. Also the presented model accounts only for the single pulse situation and the model does not take into account plasma scattering which can strongly distort the intensity distribution at the focus. Moreover, consecutive pulses will be scattered by the induced material modification.

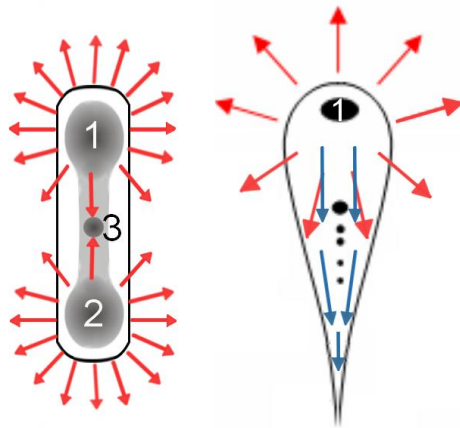


Figure 5.4: Schematic of the heat-affected regions created by a single (left) and multi-pulse (right) irradiation. Red arrows indicate stress direction and blue ones show stressed material flow which induces compaction.

During a single laser pulse, a dense electron plasma is generated via multi-photon ionization and avalanche processes in an elongated prefocal region in a quasi-cylindrical shape with rounded bases (Figure 5.4). Typical sizes of the laser-heated regions are $\sim 10 \mu\text{m}$ in length and $\sim 1 \mu\text{m}$ in diameter. As electron recombination in fused silica occurs via a trapping like process with a characteristic time of $\sim 150 \text{ fs}$, in 1 ps after the pulse action the excited region is heated to 2000 K and brought into a highly stressed state. The stress maxima (stress concentrators) in excess of 10 GPa are located at the butt-ends of the long narrow laser-heated zone, where material is melted/softened. These stress maxima are conditioned by the hot material expansion facilitated along the softened “channel”. As the stress level is more than two orders of magnitude greater compared to the tensile strength ($\sim 50 \text{ MPa}$), and exceeds the yield stress ($\sim 4.5 \text{ GPa}$) of cold fused silica (note that with heating these mechanical parameters considerably decrease), material

rupture happens in the stress maxima locations with creation of void structures. Sudden material rupture with creation of voids at the hot region ends generates emission of the unloading waves and relocation of the maximum stress sites toward the centre of the hot structure, where again the tensile strength can be exceeded. Depending on the temperature (and, hence, stress) level, a third void can be created in approximately half-way between voids 1 and 2 (Figure 5.4) or a chain rupture occurs with the formation of several successive voids along the laser-excited region. However, even slight variations of the temperature along the hot region axis and associated variations of material strength can influence the location and size of interstitial voids. Each subsequent pulse generates a denser plasma (and, hence, higher temperature) in the front part of the structure around void 1 (Figure 5.4) while a smaller portion of the laser energy is transferred to the structure's tail. As a result, the heat-affected region transforms from a quasi-cylinder to a teardrop shape under multi-pulse irradiation. The hot matter is pressed out preferably to the structure tail (blue arrows) penning the voids located there and creating material compaction. On the contrary, the front void (indicated as „1“ on the right-hand side in Figure 5.4) increases due to heat accumulation in the surrounding zone and migrates in the direction of the laser driven by the difference in surface tension, developed by the temperature gradient between the front and back poles of the void [92,93].

5.4 Experimental results

5.4.1 Bubble formation

To demonstrate this optical phenomenon, we created localized structural changes in silica glass using a tightly focused femtosecond laser beam. The experiments were carried out with a regeneratively amplified mode-locked Yb:KGW (Yb-doped potassium gadolinium tungstate) laser delivering 270 fs pulses with 200 kHz repetition rate and 6 W average power at 1030 nm wavelength. The energy of the pulse could be varied with a combination of an achromatic half-wave plate and a Glan polarizer.

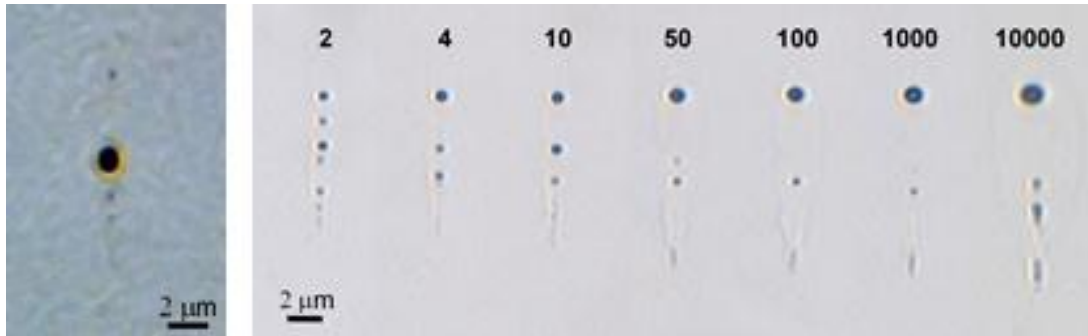


Figure 5.5: Side view of femtosecond laser induced structure. (Left) Glass modification after single pulses (enhanced contrast). (Right) Cross-sections of femtosecond laser-induced structures. The number of pulses is indicated above. The laser beam is entering from the top.

The average laser power used in the experiments was 325 mW. The laser beam was focused about 60 μm below the surface of a silica glass plate via a 100× (NA = 0.7) microscope objective. The sample was mounted on three-axial air-bearing motorized stage. The polarization state was controlled with achromatic quarter-wave plates inserted before the objective to avoid a potential polarization distortion due to reflection from the mirrors.

A series of dots was written by electronically controlling the laser output via a built-in pulse picker, while laterally translating the sample (Figure 5.5). The exposure time per single dot was in the range of 4 μs to 20 s. In order to avoid form birefringence induced by linear polarization, we used circular polarization, where femtosecond laser pulse nanogratings are not formed [94].

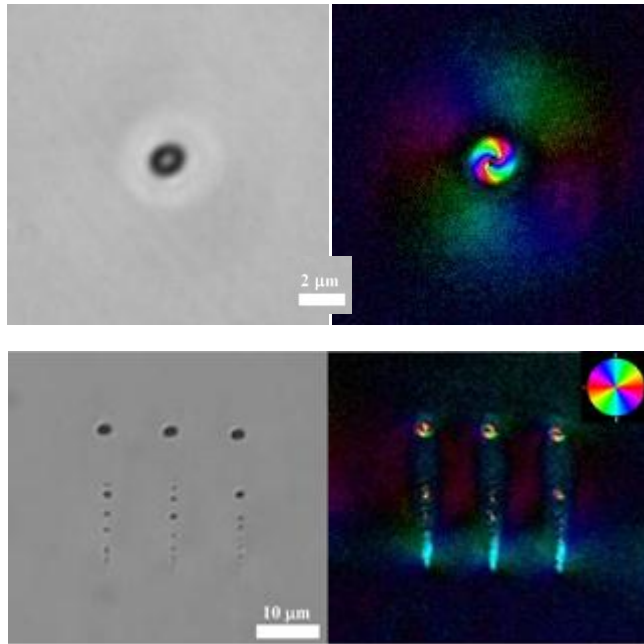


Figure 5.6: Top and side views of the structure formed by femtosecond laser in silica glass (exposition 0.01 s). Right column represents same image taken with Abrio system. The pseudo colour indicates direction of the slow axis (see legend) and the intensity relative strength of the retardance.

After laser writing, the cross-sections of the laser induced structures were investigated with a transmission optical microscope and a quantitative birefringence measurement system Abrio (CRi Inc.). Under our experimental conditions, we observed the formation of self-aligned spherical voids (Figure 5.5) whose origin is still under discussion [87–90]. In contrast with previous results [88] we observed void formation even after single pulse irradiation (Figure 5.5, left). In dots written with only several pulses, the voids were evenly distributed along the light propagation direction. At longer exposure (≥ 50 pulses per dot) smaller voids were erased leaving only a single void in the head and central part of the structures. The diameter of the induced voids varied from 600 nm to 2 μm depending on the exposure time. The analysis of birefringence revealed relatively strong anisotropy induced in the structure tail (Figure 5.6, a) while from the top of the structure the radially symmetric stress could be observed (Figure 5.6, d). Additionally, a “scissors effect” [95] could be observed outside the irradiated volume. In the front and central parts, where material was softer and, as a result, evenly distributed, no stress related birefringence was observed under all examined writing conditions.

5.4.2 Polarization conversion

For the observation of optical vortex formation, a light emerging from a halogen lamp was circularly polarized and filtered with a bandpass filter (a central wavelength of 531 nm and a bandwidth of 30 nm) (Figure 5.7). The sample was illuminated with a long working distance condenser set to 0.1 NA to achieve effective diffraction of the beam on the void. The light, transmitted through the sample, was collected with high NA objectives (0.9 and 0.6), passed through a quarter-wave plate and a linear polarizer filtering out background light, and projected onto a digital CCD camera. The handedness of the incident beam was reversed by adding an additional half-wave plate before the condenser.

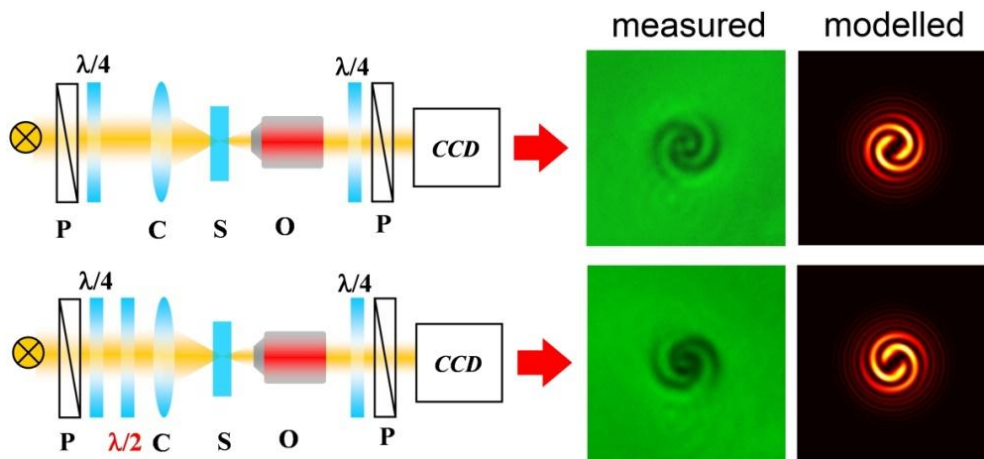


Figure 5.7: Optical setups for optical vortex observation. P – polarizer, C – condenser, S – sample, O – objective. Vortex patterns (measured and modelled), observed under left and right handed polarizations, show mirror symmetry indicating reverse of orbital momentum sign.

When the void observed in circularly polarized light was slightly defocused ($\sim 10 - 20 \mu m$), a distinctive two-branched spiral feature appeared which grew in size with increasing defocus (Figure 5.7). Depending on whenever the positive or negative defocus was added, the spiral changed its handedness. The spiral could be better seen in the focal plane located after the void. The asymmetry can be related to the residual spherical aberration which arises due to the mismatch of refractive indices at the void interior/fused silica interface. If the handedness of incident circular polarization was reversed by adding a half-wave plate, the spiral also changed its direction (Figure 5.7). This clearly demonstrates that the spiral

direction is defined by the handedness of incident circular polarization, as predicted by the modelling of the described optical system assuming a radial polarizer instead of a void. For comparison, using the Jones matrix formalism, modelling was performed of light propagation in the described optical system. The modelled patterns (Figure 5.7) are in good agreement with the measurements, confirming the validity of the model and the explanation of the phenomenon given above. Identical chiral features were found in the structures produced under the same experimental conditions with a Ti:Sapphire laser ($\lambda = 800 \text{ nm}$, $\tau_{pulse} = 150 \text{ fs}$) confirming that the observed spirals are the result of geometry of the modification.

In order to distinguish between stress and boundary related anisotropies, we inspected the bubble defects formed during glass preparation which presumably does not possess any stress birefringence. Similar two-branched spirals were observed for bubbles with diameters of $2 - 3 \mu\text{m}$. Larger bubbles, however, did not produce such patterns. This size dependence can be related to the fact, that efficient spiral shape formation requires strong interference with the background in order to reveal the presence of vortex phase. Similar spiral shapes were predicted theoretically by modelling the behaviour of a Rayleigh scatterer in a polarization microscope [96]. However, their origin was not clearly explained and was restricted to analysis of small scattering particles. We suppose that the spiral pattern is formed due to the superposition of left and right handed circular polarizations emerging when light couples with the bubble [97]. The presence of two branches clearly indicates that the OAM of the transmitted beam is $l = \pm 2\hbar$. This interference is also observed with the Abrio system and can be mistaken for a birefringent structure having whirlpool shape anisotropy. This ambiguity can be resolved by comparing images taken with left and right handed circular polarizations. The real birefringence, in contrast to the observed effect, is independent on the handedness of the circular polarization. Additionally, this suggests that the used microscope system can be effectively applied for characterizing phase singularities created by scattering or refraction on small particles.

In contrast to a conventional radial polarizer, the polarization efficiency of a void depends on the position (and, hence, angle) on the surface where light ray crosses the interface (see Equation (5.1)). The strongest effect is expected where the surface normal constitutes the Brewster angle with the incident light (Figure 5.2), i.e. where the differential transmission is the strongest. The total polarization conversion efficiency can be estimated by integrating $t_p(\theta) - t_s(\theta)$ through all θ values, i.e. from 0 to 90 degree. Assuming that the refractive indices of the glass sample and a void are respectively 1.5 and 1, the conversion efficiency of circular polarization into optical vortex is about 2% and it largely depends on the refractive index contrast and angle of incidence. One can expect that, for a ring-shaped incident beam (e.g. formed using axicon) impinging on the ring shaped area on the sphere, where the rays of light impinge at the Brewster angle and, hence, the polarization effect is strongest, the conversion efficiency will increase to $\sim 15\%$. A higher refractive index contrast would allow efficiencies of up to 40%. Alternatively, an optical vortex can be generated in reflection. However, the management of the diverging light in reflection is challenging and requires a more complicated setup. Despite the low conversion efficiencies, the proposed optical vortex formation scheme is extremely simple and compact as opposed to conventional methods. Additionally, as it is related only to the geometry of voids, the described properties are universal and can be expected in countless situations.

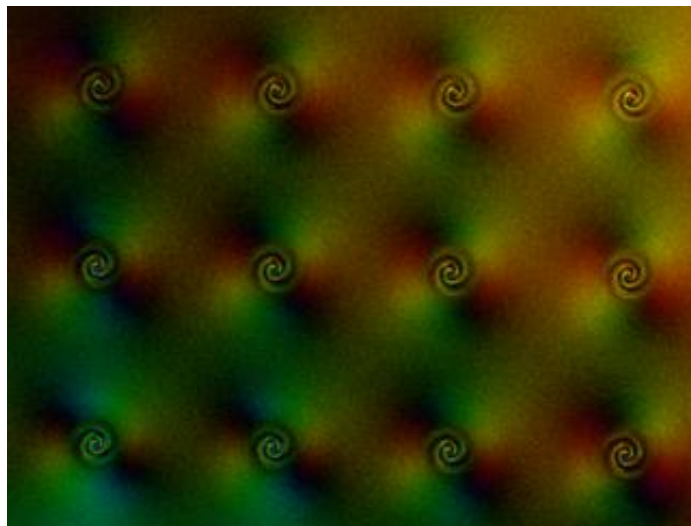


Figure 5.8: Multiple vortex conversion with an array of micro-voids (a period $10\ \mu\text{m}$).

Formation of optical vortices during femtosecond laser irradiation implies that, for circular polarization, partial angular orbital momentum interaction can occur in a multi-shot regime. The OAM acquired by the beam can interact with free electrons creating plasma whirlpools and lead to a new kind of laser-matter interaction. The flexibility of ultrafast laser direct writing also allows the production of arrays of voids, which could be integrated into microfluidic systems for the handling of micro-objects (Figure 5.8). Additionally, resolution beyond the diffraction limit can be achieved with a circularly polarized vortex.

5.5 Conclusion

Tight focusing of a femtosecond laser beam into the fused silica glass leads to the formation of micro-bubbles. The size of the bubbles depends on the exposure time. High refractive index contrast at the boundary of micro-bubbles produce spatially variant edge birefringence. We have proposed a radial polarizer based on this effect. Spatial variation of anisotropy allows orbital angular momentum formation on isotropic micro-voids embedded in isotropic medium; the magnitude of OAM is determined by radial geometry of voids. The sign of the orbital momentum can be controlled by the handedness of the incident circular polarization. The effect was successfully demonstrated on self-organized void arrays induced by tightly focused ultrashort pulses. The experimental results were backed by a theoretical model based on Jones matrix calculus and Fourier propagation. The estimated conversion efficiency is about 2%. This technique offers a practical alternative to conventional radial polarizers and a flexible way to produce dense arrays of optical vortex generators on the microscopic scale which could be used for integrated quantum optics and optofluidics.

Chapter 6. Theory of femtosecond laser induced nanogratings

6.1 Introduction

The first observation of laser induced surface ripples dates back to the sixties when Birnbaum reported ripple formation on the surface of a semiconductor [98]. Since then ripple formation was observed on virtually any material surface including dielectrics, metals and polymers. A single laser pulse of sufficient energy was enough to produce ripples on the surface. For pulses with lower energy, ripples could emerge after a longer exposure, even if the pulse energy was below damage threshold. The phenomenon turned out to be rather universal, the ripples could be formed with wavelengths ranging from the mid-infrared to the blue end of the visible spectrum and from CW operating to femtosecond lasers. For normal incidence, the period of such structures is close to the wavelength of light and perpendicular to the laser beam polarization [99]. For oblique incidence and TM polarization (electric field is in the plane of incidence) the ripples occur with one of two possible spacings [100]:

$$\Lambda_{gr} = \frac{\lambda}{1 \pm \sin \theta}, \quad (6.1)$$

where θ is the angle of incidence and λ is wavelength of incident laser light. For TE polarization Λ_{gr} remained close to the wavelength λ .

If the laser beam was moved with respect to the sample, the ripples could coherently extend over the scanned area [101].

Several models were proposed for ripple formation. One of the first explanations was that ripples are formed as a result of interference created by incident light and scattered with dust or impurities [102]. Later same authors proposed a theory based on dipole interaction [103]. The low ionisation centres were proposed to act as the radiating dipoles which could interact constructively with a laser beam. This could result in an array of dipoles radiating in phase. Another suggestion was that

there is an standing acoustic wave which results in the periodic melting of the surface [104]. Some authors suggested that surface plasmons or surface polaritons could produce the ripples [105,106]. The most widely accepted explanation is based on the interference of incident and surface scattered waves formed by random variation of surface height, electron density, defect density or any other optically significant physical property [100,102,107]. Interference of these two waves produces a sinusoidal component of light intensity impinging on the material surface. The induced modulation will further diffract light intensity continuing growth of the surface irregularities. As a result periodic structure can emerge from the initial “structural noise” [99].

However, ultrashort laser pulses were observed to induce two types of periodic surface structures [108]: above single pulse damage threshold – ripples with a period close to the wavelength and below single pulse damage threshold – sub-wavelength ripples with periods as small as 30 nm [109]. The period was found to increase with the number of pulses and fluence [110]. Peculiarly, such structures could be formed only after tens or even thousands of laser pulses. A subwavelength period with sharp features cannot be explained by incident and scattered wave interference. Thus several other models were proposed. Some explanations can be seen as an update to the classical ripple formation theory.

A decade ago, a new type of self-organization was observed inside SiO₂ glass after irradiation with an ultrafast laser [6], which was found to be responsible [52] for femtosecond pulse induced anisotropy and the propeller shape scattering reported earlier [53,54]. Under certain irradiation conditions, highly ordered subwavelength structures with features smaller than 20 nm could be formed in the irradiated volume. As opposed to surface ripples, nanostructures inside of the material were found only for a handful materials: fused silica, sapphire and several others. Recently, volume nanogratings was reported to continuously transform into surface ripples when the laser focus is moved out of the sample [111]. As a result, some theories on nanostructure formation try to reconcile surface ripple and volume nanograting formation.

6.2 Overview of proposed bulk ripple formation theoretical models

The first model proposed for volume nanograting formation was indeed an extension of traditional surface ripple formation theory [6] and relied on the interference of the bulk electron plasma longitudinal wave with the incident light. The coupling can couple only if the plasma wave propagates in the plane of light polarization. The initial coupling is presumably produced by inhomogeneities induced by electrons moving in the plane of light polarization. The periodic structure created due to the interference further enhances this coupling, resulting in periodic modulation of plasma concentration. Further this modulation is frozen within the material. The nanograting period can be defined from conservation of the longitudinal component of momentum:

$$\mathbf{k}_{ph} + \mathbf{k}_{gr} = \mathbf{k}_{pl}, \quad (6.2)$$

where:

$$k_{ph} = \frac{\omega n}{c} - \text{photon wavevector,}$$

$$k_{pl} = \frac{\omega_{pl}}{v_{pl}} - \text{plasma wavevector,}$$

$$k_{gr} = \frac{2\pi}{\Lambda_{gr}} = \sqrt{k_{pl}^2 - k_{ph}^2} - \text{grating wavevector.}$$

Finally one can arrive at the explicit equation for the grating period Λ_{gr} :

$$\Lambda_{gr} = \frac{2\pi}{\sqrt{\frac{1}{T_e} \left(\frac{m_e \omega^2}{3k_B} - \frac{e^2 \eta_e}{3\epsilon_0 k_B} \right) - k_{ph}^2}}. \quad (6.3)$$

This dependence shows that the grating period Λ_{gr} increases with electron concentration and temperature. Steep increase of the period occurs when the electron concentration η_e approaches the critical plasma density:

$$\eta_{cr} = \frac{\omega^2 \epsilon_0 m_e}{e^2}. \quad (6.4)$$

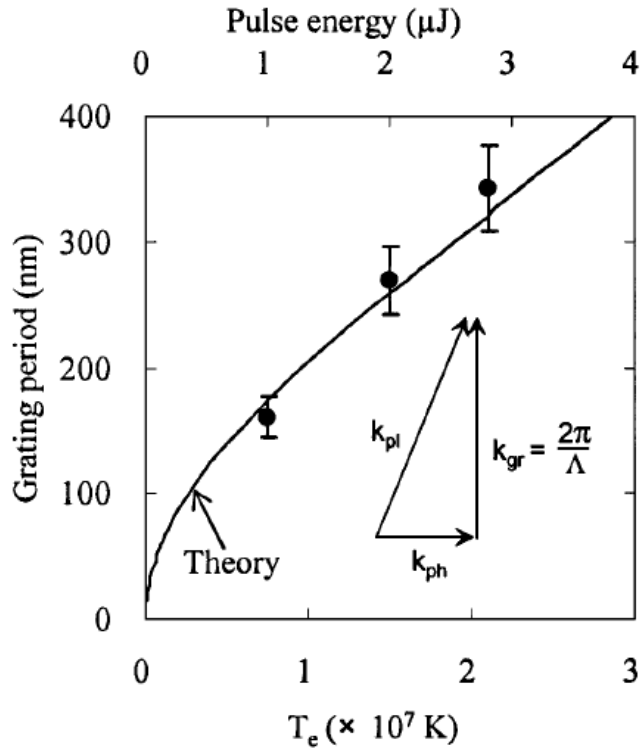


Figure 6.1: Nanograting period evolution predicted by plasmon interference theory. Inset shows wave vector matching diagram. Image source: [6].

Another consequence of this model is an energy dependent nanograting period, which should grow together with pulse energy. For a period of 150 nm induced with 800 nm wavelength ultrashort laser pulses, the following conditions were found: $T_e = 5 \times 10^7$ K and $\eta_e = 1.75 \times 10^{21} \text{ cm}^{-3}$. Similar conditions were reported for micro-explosions induced with ultrashort laser pulses [40]. However, nanograting formation was observed even for 100 nJ laser pulses, suggesting that nanogratings can be assembled at subcritical plasma concentrations. Also electron temperature can be limited by the band gap of the material, the hot electrons will dissipate their energy through impact ionization.

Taking these facts into account, the plasmon interference model was modified by assuming two-plasmon decay [35]. The major difference to the previous explanation is the excitation of two bulk plasmons of about half of the photon energy. This process can take place at much lower electron concentration $\eta_e = \frac{\eta_{cr}}{4} \sim 4 \times 10^{20} \text{ cm}^{-3}$. The electron temperature is also substantially reduced to 10^4 K.

The other attempt to explain the nanograting formation phenomenon was by nanoplasma formation [112]. The idea of this theory is the following. Initially, a focused ultrashort light pulse ionizes defects and colour centres leading to the formation of inhomogeneous plasma (Figure 6.2a). These plasma hot-spots after multiple laser pulses can evolve into spherically shaped nanoplasma. The local field enhancement at the boundary will result in an asymmetric growth of initially spherical nanoplasma in the direction perpendicular to the laser polarization (Figure 6.2b), there electric field at the poles E_{pol} and equator E_{eq} of the nanoplasma sphere will be the following:

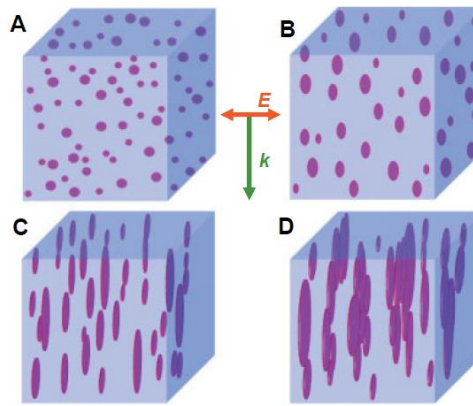


Figure 6.2: Evolution of nanoplasma (A) formed at the ionized defects or colour centres into nanoplans (D). Image source: [113].

$$E_{pol} = \frac{3\epsilon_p E}{\epsilon_p + 2\epsilon_d} \quad (6.5)$$

$$E_{eq} = \frac{3\epsilon_d E}{\epsilon_p + 2\epsilon_d} \quad (6.6)$$

there ϵ_d and ϵ_p are the real parts of the electric permittivity for dielectric medium and plasma. When the electron concentration is below critical $E_{pol} < E_{eq}$. The electric field is enhanced at the equator leading to nanoplans formation. Further evolution of nanoplans results in quasi-metallic waveguiding, which leads to a prediction of nanograting period equal to $\lambda/2n$, where n is refractive index of fused silica. The difficulty in this theory is that at high electron concentration when $\epsilon_p > \epsilon_d$, as a result $E_{pol} > E_{eq}$ and nanoplans could not be formed [114].

The imprint of plasma concentration modulation can be recorded via generation of defects such as nonbridging oxygen-hole centres and interstitial oxygen atoms [6]. Such oxygen atoms are mobile and can diffuse from the regions with high concentration.

Some difficulties still remain, as the plasma frequency cannot be defined as it depends on the concentration of free carriers, which is nearly zero in the absence of light and strongly varies as a function of time when the sample is illuminated with a light pulse. It is also unclear how the plasmons may be responsible for the formation of a grating in the propagation direction (Figure 6.3).

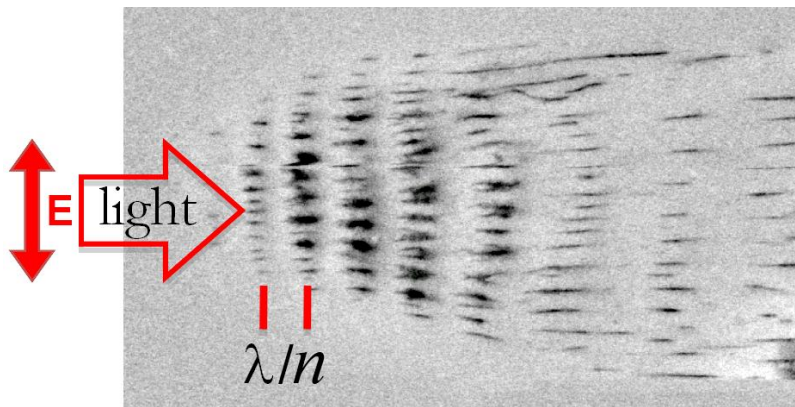


Figure 6.3: Self-assembled nanograting induced by femtosecond laser irradiation ($\lambda = 1045$ nm) inside fused silica. SEM image with backscattered electrons. Two periodicities (along the light propagation and electric field directions) can be clearly seen. The arrows indicate light propagation and electric field E polarization directions, n – refractive index of fused silica (Source: [115]).

6.3 Excitonic model of nanograting formation

An alternative theory was suggested by A. V. Kavokin, in which the nanograting is formed due to interference, attractive interaction and self-trapping of exciton-polaritons [116]. It is well-known that the absorption spectra of SiO_2 are characterised by a strong exciton peak at about 10.4 eV [117,118]. The binding energy and oscillator strength of excitons in SiO_2 are expected to exceed by orders of magnitude those in GaAs, where excitonic effects are studied in detail. In striking similarity to our observation, formation of a polarization grating in the direction of propagation of light due to interference of exciton-polariton modes in GaAs was predicted more than 11 years ago [116]. The period of this grating was found to

gradually increase as a function of the distance from the front edge of the sample due to the dependence of the splitting between two interfering exciton-polariton modes on the group velocity of the exciton-polaritons. In the fused silica case, the two dispersion branches of exciton-polaritons (Figure 6.4) may be excited simultaneously by multiphoton absorption. The interference of propagating exciton-polaritons results in formation of the polarization grating (Figure 6.4).

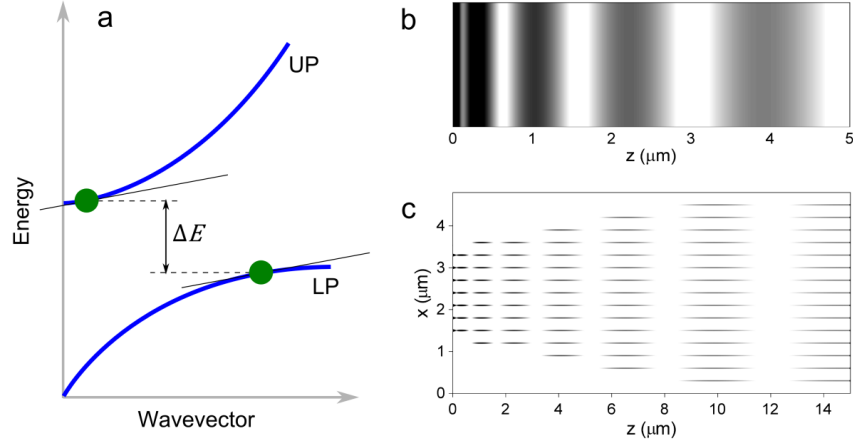


Figure 6.4: Theoretical simulation of the formation of the nanograting. **(a)** is a schematic of the exciton-polariton dispersion, showing a point on the upper polariton branch (UP) and a point on the lower polariton branch (LP) with the same group velocity, and their splitting in energy ΔE (not in scale). **(c)** shows the grating in x and in z , while **(b)** shows a zoom of the grating in the z -direction.

The simulation is performed using a semiclassical approach. The dielectric polarization in the direction of propagation may be calculated as:

$$\mathbf{P}_{exc}(z) = \chi_e \mathbf{E}(z), \quad (6.7)$$

where $\mathbf{E}(z)$ is the electric field, and the dielectric susceptibility is given by

$$\chi_e = \frac{\epsilon_b \omega_{LT}}{\omega_0 - \omega - i\gamma}. \quad (6.8)$$

ω_0 and ω_{LT} denote the exciton resonance frequency and the exciton longitudinal-transverse splitting respectively, γ is the exciton non-radiative broadening, and ϵ_b is the background dielectric constant. The time dependent polarization is calculated using the scattering state approach in which frequency dependent solutions of Maxwell's equations (called scattering states) are Fourier integrated,

with a spectral function characterizing the pulse. The exciton inhomogeneous broadening does not qualitatively change the effect of grating formation [116]. The splitting of exciton-polariton modes in SiO₂ is more than 100 meV, which exceeds the inhomogeneous broadening of the free exciton resonance. Also note that the first period of the polariton grating shown in Figure 6.4 is very close to the wavelength of light. Then the period increases as a square root of the distance from the sample edge, approximately. These two features are in excellent agreement with the experiment which confirms the validity of the model.

To obtain the distribution of exciton density in the direction of light polarization, the exciton gas energy is minimised for fixed exciton concentration, n_{ex} , accounting for the attractive dipole-dipole interaction between coherent exciton-polaritons. This excitonic system can be described by the Hamiltonian:

$$H = -\frac{\hbar^2}{2m} \frac{\partial^2}{\partial x^2} + \alpha |\psi|^2, \quad (6.9)$$

where m is the mass of an exciton and α is the negative (attractive) exciton-exciton interaction constant. This Hamiltonian is expected to correctly describe the exciton-polariton dynamics in the direction of the polarisation vector. Then characteristic size of in-plane wave-vectors of the polariton fluid is much less than the wave-vector of light, which is exactly the case in our system.

The equation is solved variationally with a trial function

$$\psi = \sqrt{\frac{N}{a}} \left(\frac{2}{\pi}\right)^{\frac{1}{4}} e^{-x^2/a^2}, \quad (6.10)$$

where $N = n_{ex}d$ is the number of excitons, d is the exciton mean free path, and a defines the width of the Gaussian. Then the energy may be found and minimised with respect to a (Figure 6.5). Therefore only two fitting parameters are used: the interaction constant α , which is taken to have the value 2.25×10^{-7} meV cm. This value seems sensible when compared to values measured in and predicted for GaAs microcavities [119,120]. The second fitting parameter is the exciton mean free path d . The calculation with only two fitting parameters yields a good qualitative agreement with the experiment (Figure 6.5).

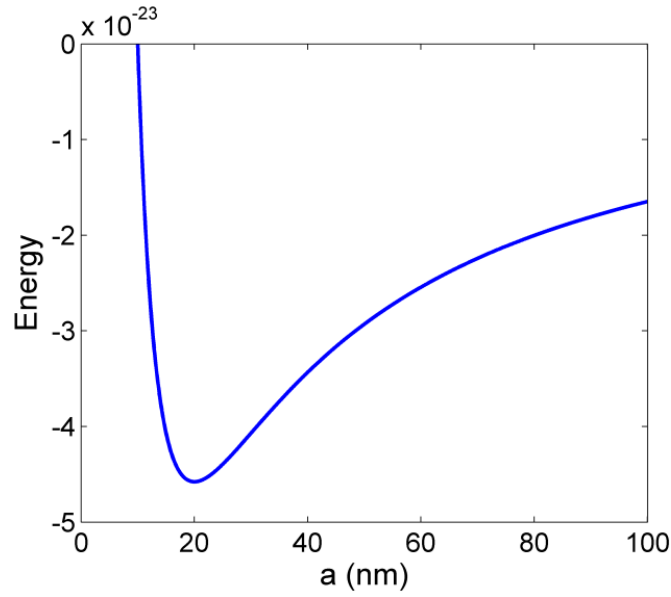


Figure 6.5: Energy as a function of a for $d = 300$ nm, showing the minimum at $a = 20$ nm.

6.4 Discussion

The exciton-polaritons form a dynamical grating which evolves in time. However, the lifetime of exciton-polaritons is limited to a fraction of a picoseconds (< 300 fs) by their phonon assisted relaxation to indirect exciton states decoupled from light [43]. The indirect excitons are essentially immobile. They are easily self-trapped and live several microseconds or even longer [121]. Excitons generated by subsequently arriving pulses of light are accumulated in significant concentrations in the specific sites of the sample corresponding to the peaks of the exciton-polariton density in the polariton grating generated in the same fashion by all pulses. Recombination of self-trapped excitons is accompanied by the generation of molecular oxygen [47] due to the photosynthesis-like reaction:



where X denotes an exciton. Recently the presence of molecular oxygen was confirmed for GeO_2 glass after femtosecond laser irradiation [122]. Nanopores of silica filled by oxygen are formed in the locations of high concentrations of self-trapped excitons. Agglomerations of these nanopores form the grating seen in the

SEM images (Figure 6.3). They are responsible for the freezing of light in silica glasses.

6.5 Conclusions

Several attempts were made to explain the self-organising effect observed in fused silica glass under femtosecond laser irradiation. The nanogratings formation was attempted to be explained by plasma interference, nanoplasma formation or self-organization of exciton-polaritons. The explanations are more related to excitation of plasma or excitons and their interaction with light. However, each of the proposed theories is supported solely by observations made after the irradiation. It is not fully clear how nanogratings assembled in matter (while it is still excited) are imprinted afterwards. All of the presented theories consider nanogratings formation under single laser pulse irradiation. However, it is well known that nanogratings can be formed only after a sequence of laser pulses. It indicates that some sort of accumulation must take place. Direct experimental observations on nanogratings formation would definitely be of benefit to the explanation.

Chapter 7. Properties of femtosecond laser pulse induced nanogratings

7.1 Spectral properties of the nanogratings

In this chapter we analyse properties of femtosecond laser pulse induced nanogratings. First there is a theoretical description of form birefringence and modelling results on fused silica dispersion influence on the properties of the nanogratings.

The second part of this chapter is an experimental study of nanogratings obtained under various writing conditions. In these experiments we discovered that isotropic refractive index increase can be successfully achieved under > 300 fs laser irradiation, which was said to be impossible earlier.

The period of nanogratings is known to be strongly dependent on the wavelength of the laser [46]. Additionally one should expect strong dependence on the wavelength if nonlinear absorption is playing a crucial role in material excitation. As a result the experiments were performed with fundamental and second harmonics of the laser.

7.1.1 Modelling spectral properties of nanograting

The dispersion in the layered media can arise due to two factors; one is intrinsic refractive index dispersion of the comprising layers, second is the dependence of the effective refractive index on the ratio λ/Λ , (where λ is the wavelength of incident light, Λ is the period of the layered medium). The last factor manifests on the shorter wavelength scale and can be calculated from the dispersion relation for a two-component layered medium [123]. The period of self-assembled nanogratings is in the range 100 – 300 nm and varies with the wavelength, writing speed and pulse energy [46]. Thus the dispersion arising due to the complex structure of the layered medium will also play an important role. Based on modelling results it is expected to have a slowly rising difference of refractive

indices if the medium and silica dispersions are taken into account. The light induced defects are expected to decrease the refractive index; however, the dispersion will follow the same trend that of a pure material.

It is known that homogeneous periodic layered medium behaves as uniaxial birefringent crystal [124]. This means that the electric field oscillating along (TE mode) and perpendicular (TM mode) to the layered medium obtain a different amount of the phase shift.

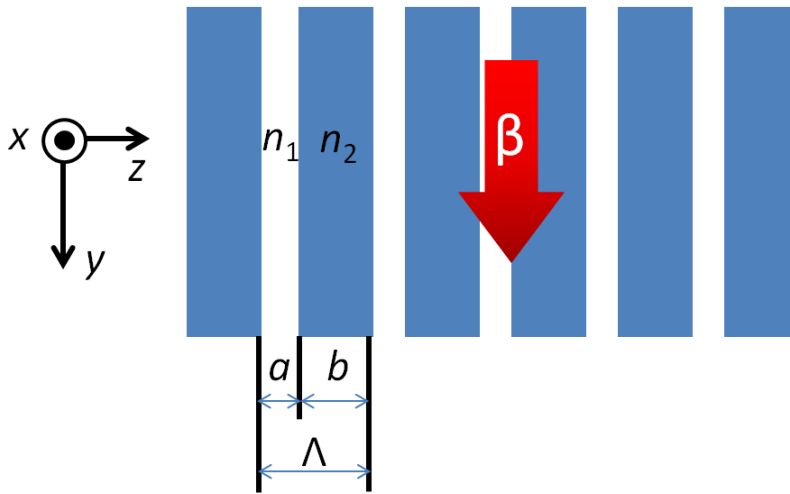


Figure 7.1: Light with wave number β propagation along the plates of the nanograting. The grating consists of two layers with thickness a (refractive index n_1) and b (refractive index n_2). The image after [125].

The equations describing this behaviour are the following:

TE mode

$$\cos(K\Lambda) = \cos(k_{1z}a) \cos(k_{2z}b) - \frac{1}{2} \left(\frac{k_{2z}}{k_{1z}} + \frac{k_{1z}}{k_{2z}} \right) \sin(k_{1z}a) \sin(k_{2z}b) \quad (7.1)$$

TM mode

$$\cos(K\Lambda) = \cos(k_{1z}a) \cos(k_{2z}b) - \frac{1}{2} \left(\frac{n_2^2}{n_1^2} \cdot \frac{k_{1z}}{k_{2z}} + \frac{n_1^2}{n_2^2} \cdot \frac{k_{2z}}{k_{1z}} \right) \sin(k_{1z}a) \sin(k_{2z}b) \quad (7.2)$$

where

$$k_{1z,2z} = \sqrt{\left(\frac{n_{1,2}\omega}{c}\right)^2 - \beta^2} \quad (7.3)$$

$$\beta = \frac{\omega n_{TE, TM}}{c} \quad (7.4)$$

For the geometry shown in Figure 7.1 $\cos(K\Lambda) = 1$, where K is a wavevector of the periodic structure. These equations however cannot be solved analytically for n_{TE} and n_{TM} and thus require optimisation algorithms.

In certain cases, when $\Lambda \ll \lambda$ second order approximation can be used [123], when:

$$\frac{K^2}{n_o^2} + \frac{\beta^2}{n_o^2} = \left(\frac{\omega}{c}\right)^2 \quad (7.5)$$

$$\frac{K^2}{n_o^2} + \frac{\beta^2}{n_e^2} = \left(\frac{\omega}{c}\right)^2 \quad (7.6)$$

The refractive indices are then:

$$n_o^2 = \frac{a}{\Lambda} n_1^2 + \frac{b}{\Lambda} n_2^2 \quad (7.7)$$

$$\frac{1}{n_e^2} = \frac{a}{\Lambda} \frac{1}{n_1^2} + \frac{b}{\Lambda} \frac{1}{n_2^2} \quad (7.8)$$

where n_1 and n_2 are the refractive indices for the two materials of thickness a and b comprising the nanograting. In this approximation however there is no dependence on the wavelength of the incident light, i.e. there is no dispersion. If wavelength is close to the grating period this approximation becomes invalid. The problem can be partially solved by adding higher order approximation [123], which provides some dependence on the wavelength at the expense of simplicity of the formulas:

$$\bar{n}_o^2 = n_o^2 + \Delta n_o^2 \quad (7.9)$$

$$\bar{n}_e^2 = n_e^2 + \frac{\Delta n_o^2 n_e^4 (n_1^2 + n_2^2)}{10 n_1^2 n_2^2 n_o^2} \quad (7.10)$$

$$\Delta n_o^2 = \frac{(ab)^2(n_1^2 - n_2^2)^2 \left(\frac{\omega}{c}\right)^2}{10\Lambda^2} \quad (7.11)$$

Considering femtosecond laser induced nanograting as a laminar structure with $a = 20 \text{ nm}$, $b = 250 \text{ nm}$ and refractive indices $n_1 = 1$ (air) and $n_2 = 1.45$ (fused silica) we get the result shown in Figure 7.2. The values used for these calculations are based on experimental observations [6,46]. First of all, both methods give negative birefringence values as it should be expected for form birefringence. However, the values are about ten times larger than measured experimentally. This indicates that there is much smaller refractive index contrast. To confirm this the dispersion was calculated using $n_1 = 1.3$ and $n_2 = 1.45$, where values of refractive indices were found fitting the experimental data. In this case, the birefringence values are close to the expected ones. The dispersion curve, however, shows monotonous decrease with the wavelength, which contradicts the experimental observations presented below.

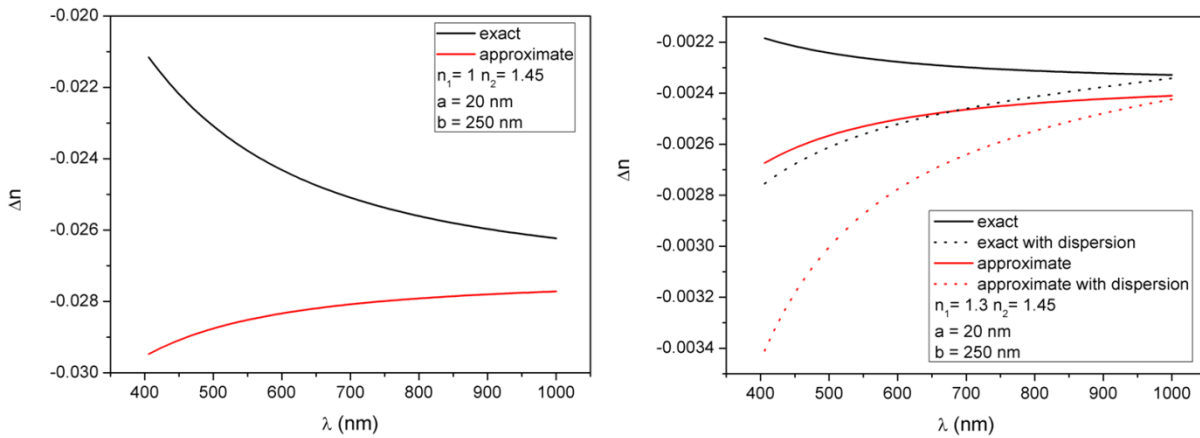


Figure 7.2: Form birefringence dispersion calculated for two laminar structure models using exact and approximate formulas. Parameters used for calculation are shown in the legends.

Adding dispersion of the fused silica described by the following Sellmeier equation¹:

$$n_2 = n_{SiO} \quad (7.12)$$

$$= \sqrt{1 + \frac{0.6961663\lambda^2}{\lambda^2 - 4.679148 \times 10^{-3}} + \frac{0.4079426\lambda^2}{\lambda^2 - 1.3512063 \times 10^{-2}} + \frac{0.8974794\lambda^2}{\lambda^2 - 9.7934002 \times 10^1}}$$

it was possible to achieve an increase of birefringence with the wavelength using Equations 7.1 and 7.2. The approximate model always gives a birefringence increase with wavelength. Both models approach to the steady value predicted by Equations 7.7 and 7.8. This dispersion modelling indicates complex inner structure of a femtosecond laser induced nanostructure, which could not be described by a simple two layer laminar structure model.

7.1.2 Measuring spectral properties of nanograting

For the experiments a series of squares (2 mm × 2 mm) was written with first (1030 nm) and second (515 nm) harmonics at various pulse energies and speeds. The repetition rate was set to 200 kHz and the numerical aperture of the objective was 0.16. After the laser irradiation, the samples were analyzed with a polarization measurement set-up, comprised of a supercontinuum laser source SC450 (Fianium Ltd.) and broadband polarization optics. The specified spectrum with for this laser source is 450-1750 nm. The average power 2.3 W and a 400 fs pulse is delivered with a 20 MHz repetition rate. After the laser source a narrow band dichroic mirror is inserted to separate the fundamental wavelength from the generated supercontinuum (450 – 750 nm).

¹ Source: http://cvimellesgriot.com/products/Documents/Catalog/Dispersion_Equations.pdf

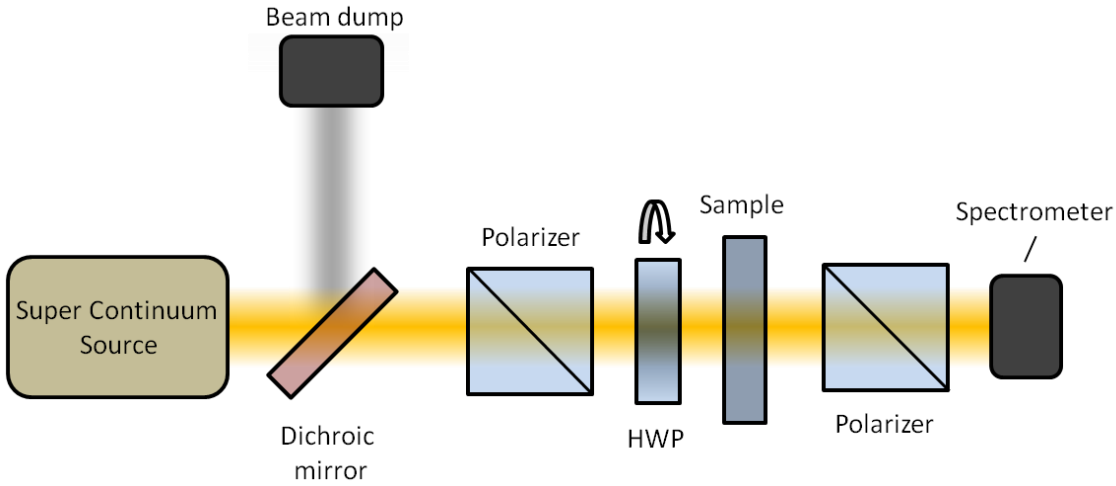


Figure 7.3: Retardance measurement set-up. The supercontinuum laser source is emitting a broad spectrum spanning from 450 to 1750 nm. The dichroic mirror is used to reflect strong the fundamental wavelength component. After the mirror the spectrum is 450-750 nm. The polarizers and achromatic half-wave plate are designed to work efficiently at the given wavelengths.

The achromatic half-wave plate is used to control the incident linear polarization and to measure transmission spectra for two perpendicular polarizations with an optical fibre coupled spectrometer. After a simple mathematical operation the retardance spectral $R(\lambda)$ dependence can be calculated:

$$R(\lambda) = \text{acos} \left(\frac{T_{45} - T_{-45}}{T_{45} + T_{-45}} \right) \cdot 2\pi\lambda \quad (7.13)$$

where T_{45} and T_{-45} are the transmission for two second polarizer positions (Figure 7.3). The same measurement technique was used with our femtosecond laser system Pharos to characterize birefringence at 515 and 1064 nm. Additionally, we were able to incorporate a telecommunication fibre laser operating at 1550 nm. Thus using the available laser sources we were able to characterize laser induced birefringence from 450 nm to 1550 nm.

The quantitative birefringence measurement system Abrio (CRi. Inc.), operating at 515 nm, was used for calibration of the described retardance measurement system and additional birefringence characterization. The losses (180 – 650 nm) of the laser induced permanent material modification were measured with the spectrometer Varian Cary 500.

7.1.3 Experimental results

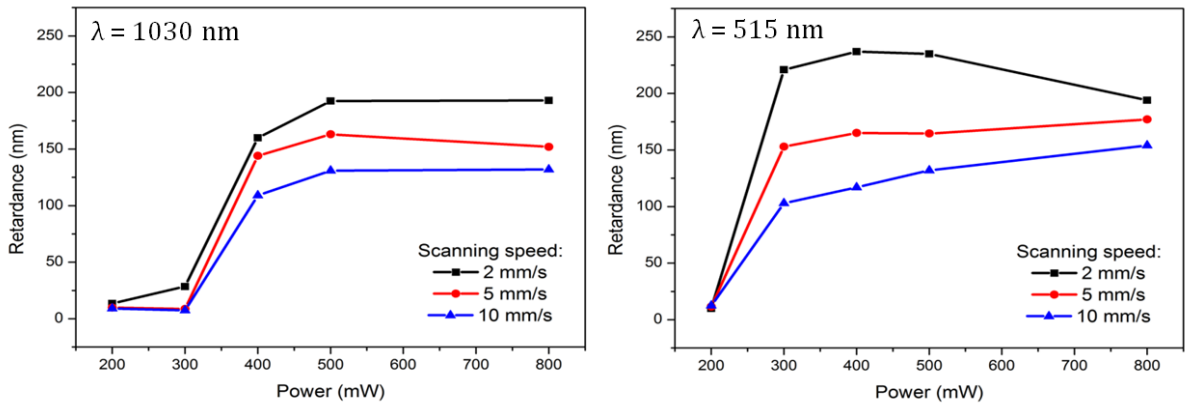


Figure 7.4: Retardance dependence of the average power and writing speed for nanogratings induced with 515 nm (below) and 1030 nm (above). The steep increase of retardance at 300-400 mW indicates phase transition from type I to type II modification.

Depending on the fluence two distinctive types of material modification were obtained. At low pulse energies and high scanning speeds the isotropic refractive index increase was induced. This type of modification does not exhibit birefringence and has negligible losses over the whole visible region. According to previous studies, isotropic refractive index increase could not be achieved with pulse durations longer than 150 fs [45], however, in our experiments we noticed that this modification can be induced even with 800 fs pulse trains if the pulse energy and number is relatively small (few hundreds of pulses) or in other words if the writing speed is high enough (at least 2 mm/s).

This observation indicates that waveguiding structures can be written in fused silica even with relatively long sub-picosecond laser pulses - the duration which is typical for amplified diode pumped solid state or fibre laser systems.

The second type of modification exhibits strong anisotropy related to self-assembled nanostructures and high scattering losses at short wavelength (Figure 7.5).

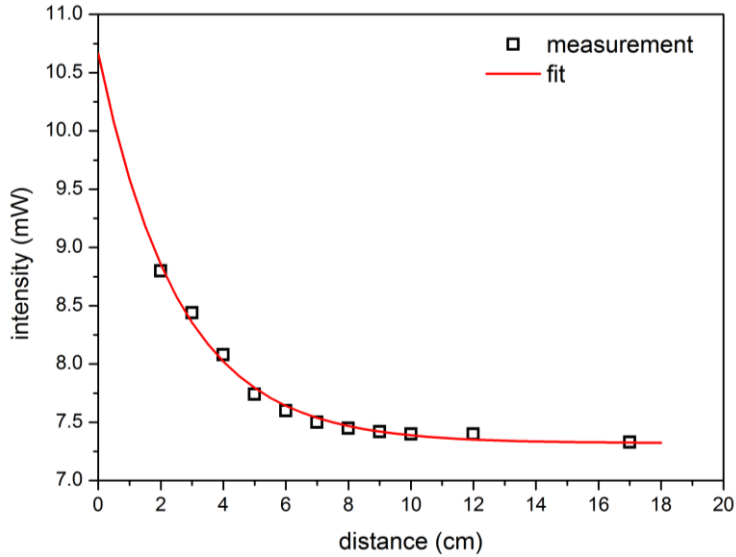


Figure 7.5: The birefringent region transmission of 515 nm measured at different distances from the sample. The red line is an exponential fit of the measured data. Exponential decrease in the transmitted intensity confirms our assumption that the main part of the losses is introduced by scattering.

The assumption that losses mainly occur as a result of scattering on inhomogeneous structures was confirmed by transmission measurements made at a fixed wavelength and various distances from the photo-detector to the sample (Figure 7.5). In this experiment the radial polarization converter for 515 nm was used as a birefringent sample. The intensity was measured on the optical axis of the system. The obtained transmission data was fitted with the exponential function:

$$I_t = a \exp(-b \cdot d) + c \quad (7.14)$$

where a , b and c are fitting parameters, and d is the distance from the detector to the sample. From the data we estimate that from the incident light 50% are scattered in equal parts in forward and backward directions. For more precise characterization the losses need to be characterized using integration sphere.

Strong retardance was induced above $2 \mu\text{J}$ for 1030 nm and $1.5 \mu\text{J}$ for 515 nm (Figure 7.4). The threshold was independent of the writing speed. One can notice, that once the nanograting is induced (above $2 \mu\text{J}$), the retardance is weakly dependent on the average power, rapidly reaching a certain saturation value. Additional measurements revealed that the retardance rapidly grows in a

relatively narrow region of pulse energies, mainly from 1.5 to 2 μJ for 1030 nm. The threshold for nanograting is slightly higher for 1030 nm than for 515 nm, as it should be expected having in mind the lower energy of light quantum. The retardance values however are of the same order and do not have any significant difference. This indicates that non-linear absorption does not play crucial role in nanograting formation. On the other hand, it slowly decreases with writing speed, or number of pulses. At higher average powers a slight decrease is already observed which is related to stronger material damage of the material. The losses measured for the same structures do not correlate with retardance measurements, indicating they are not related to nanograting formation. Additionally, the losses are independent on the wavelength of the femtosecond laser pulses and on the writing speed, but strongly depends on incident average power. At 515 nm, more than 40% of incident light is scattered, however at 1030 or 1550 nm the scattering is strongly reduced. As a result, structures of better optical quality are expected if written at lower translation speeds.

The main part of losses observed for Type 2 modification is contributed from the Rayleigh scattering of the inhomogeneous structure, which has $1/\lambda^4$ dependence. Additionally, two absorption bands can be distinguished at short wavelength, which are attributed to Si E' centers (210 nm), an unpaired electron in a silicon atom bound to three oxygen atoms, and ODC(II) (245 nm), a divalent silicon atom, defects induced by ultrashort light pulses [126]. For comparison, structures exhibiting isotropic refractive index increase showed negligible scattering and curiously only the E' center related absorption band could be observed at short wavelengths.

Comparing the transmission losses for samples written with the first and second harmonics, one can notice that for second harmonic irradiated samples have less pronounced defect bands, which could explained by partial annealing occurring due to heat accumulation at high repetition rates (Figure 7.6). However, total losses are higher for second harmonic irradiated samples. This could be result of higher nonlinear absorption for more energetic quanta.

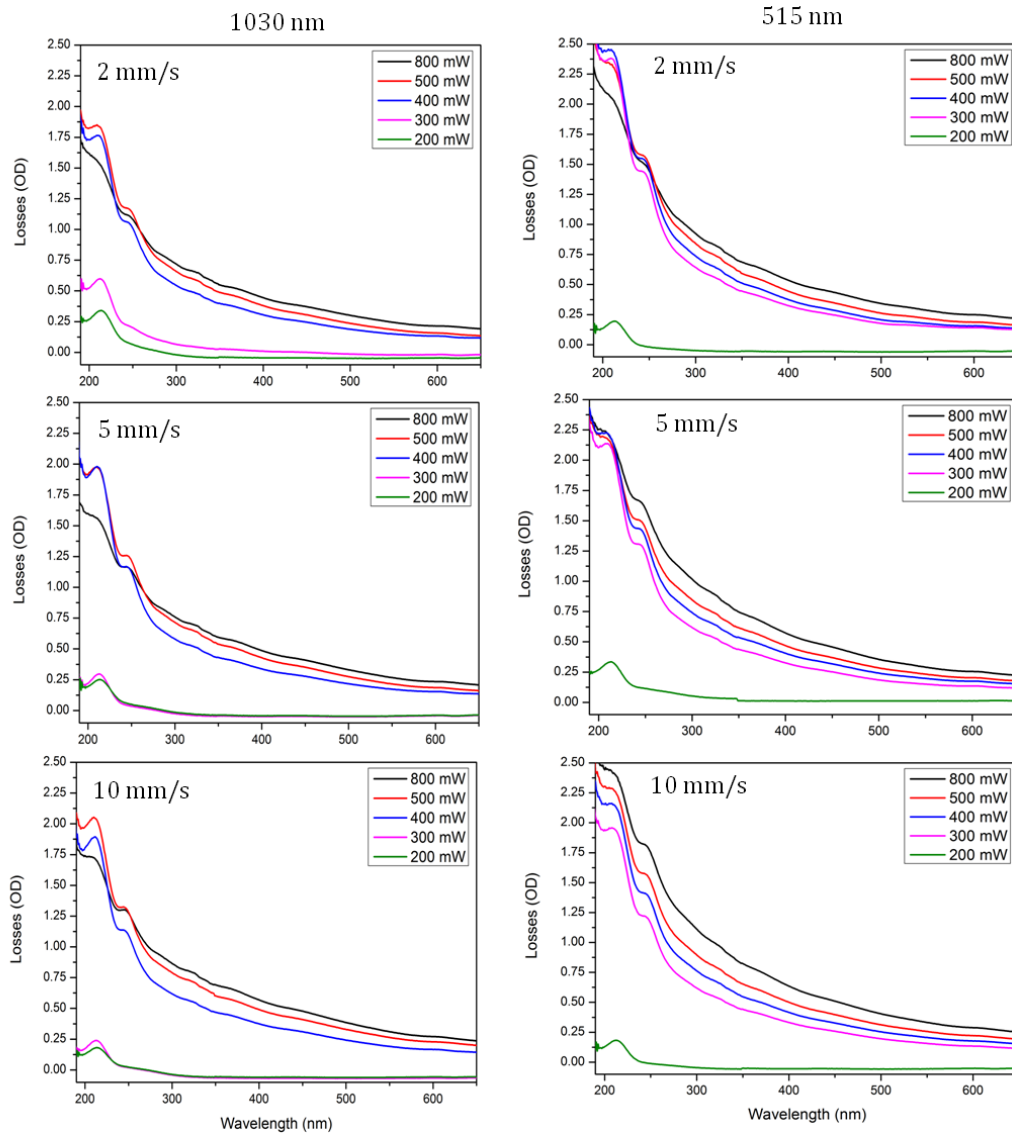


Figure 7.6: Losses for group of samples written at 1, 5 and 10 mm/s translation speed with I and II harmonics (1030 nm and 515 nm). The legend indicates the range of average power used during the writing procedure. The large separation between structures written at 200 mW and 300-800 mW indicates presence of I (isotropic refractive index increase) and II type (nanograting) modifications.

The losses also tend to be lower for the structures written with lower translation speed. It is known that the nanograting evolves from the randomly distributed planes aligned perpendicular to the polarization to well organized periodic gratings with the number of pulses. One could expect an increase of optical quality with the reduced translation speed.

The measured retardance dependence (excluding oscillation observed due to the self-interference of the laser beam) with a wavelength shows a steady rise in the

spectral region from 450 to 550 nm and a plateau extending to at least 1.5 μm (Figure 7.7). The long plateau tail could be expected, as at longer wavelengths the retardance approaches asymptotically to a nondispersive value predicted by effective medium theory. However, the form birefringence theory predicts a less rapid change of retardance as the light wavelength approaches the period of the nanostructure. The reason of this abnormal sharp retardance decrease could be attributed to the complex physical structure of the induced nanogratings which is not fully described by the simplified laminar model. Alternatively, this can indicate the presence of strong dispersion of the material modified during the laser irradiation. However, defects induced by laser irradiation will contribute only to a slight refractive index change and should not strongly affect retardance dispersion.

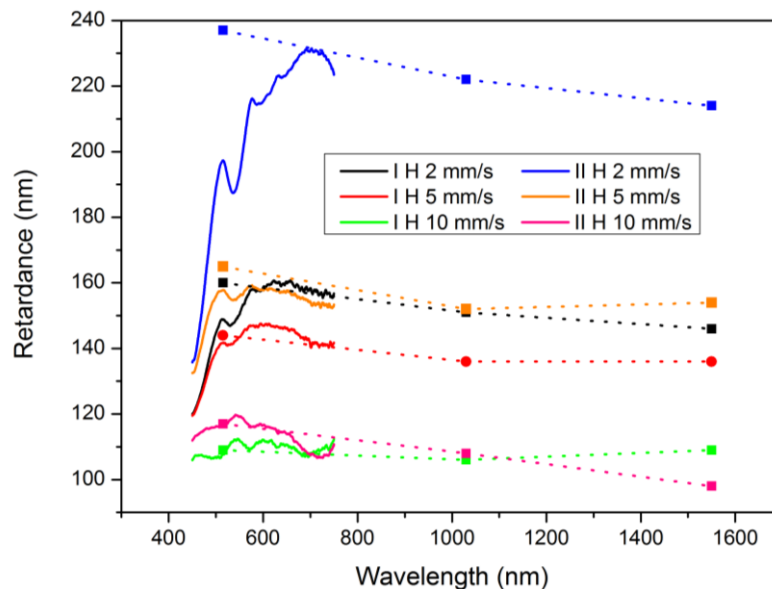


Figure 7.7: Spectral dependence of femtosecond laser induced retardance in fused silica glass. Oscillations seen on the short wavelength side are due to interference of the coherent white light laser source used in the experiments. The dashed lines indicate independent measurements performed with 3 different laser sources at 515 nm, 1030 nm and 1550 nm.

7.2 Retardance dependence on spherical aberration

The way to increase the induced retardance is the introduction of strong spherical aberration. It is known that spherical aberration inevitably are present in the case of strong focusing as a result of the refractive index mismatch at the interface of two transparent media [31]. The deeper the geometrical focus is moved into the

bulk of the sample, the stronger the beam is distorted. Mostly, this effect is undesired as it strongly distorts the intensity distribution in the focus and decreases writing resolution. Multiple techniques inherited from optical microscopy were explored to eliminate it. Among the most popular methods for aberration compensation are phase manipulation with a spatial light modulator or tube lens and the use of immersion lenses. However, spherical aberration can be an effective way of extending the focus in the light propagation direction and should result in an increased retardance, which is the product of induced refractive index difference ($n_e - n_o$) and physical length of a induced structure.

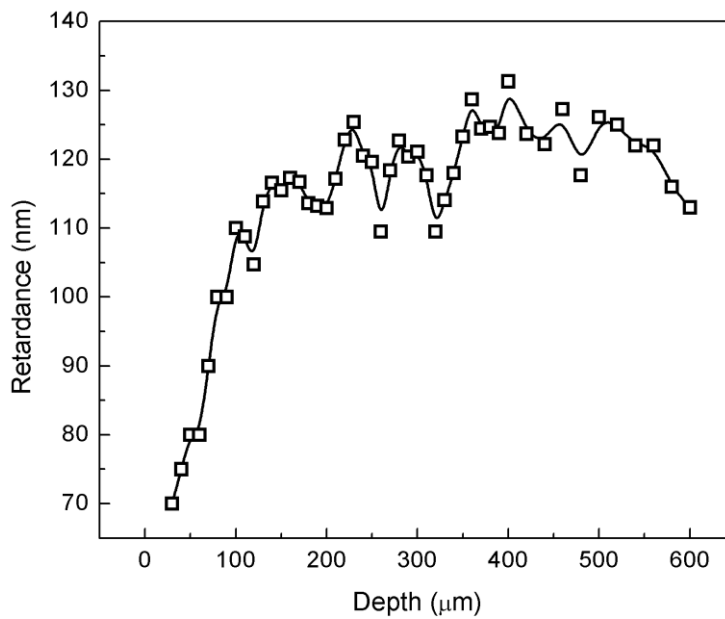


Figure 7.8: Dependence of induced retardance on focusing depth. Pulse energy was $0.75 \mu\text{J}$ and numerical aperture 0.7.

This expectation was tested using a 0.7 N.A. Mitutoyo objective. As it was shown in Chapter 2 even at a focusing depth of $50 \mu\text{m}$ strong focus elongation can be achieved with such a numerical aperture. In the experiment the geometrical focus was moved from the surface down to $600 \mu\text{m}$ into the bulk of the sample. The effect of spherical aberration was monitored by measuring the induced retardance after the laser irradiation (Figure 7.8). The measurements demonstrated that we managed to increase retardance from 70 nm up to 150 nm during the single scan by keeping the pulse energy at a constant value of $0.75 \mu\text{J}$. This clearly demonstrates the strong influence of spherical aberration on the laser writing

process at this relatively high numerical aperture. The observed effect can be explored as an additional tool for precise tuning of laser induced birefringence. It is worth mentioning, that the retardance value became saturated after about 150 μm depth which can be a result of laser beam filamentation which will lock the laser intensity and prevent from further decrease.

The mathematical modelling of laser intensity distribution at the presence of spherical aberration was performed together with Dr. David Lara from Imperial College. The intensity distribution at the focus was modelled using a three dimensional Fourier transform [127]. The laser beam was linearly polarized along the x axis and was approximated as a plane wave. The vectorial electric field distribution was calculated for focusing depths from 0 to 300 μm with a 25 μm step. At a 0.7 numerical aperture the depolarization of the electric field was still negligible, i.e. almost no electric field was present for y and z polarized components of the polarization (Figure 7.9).

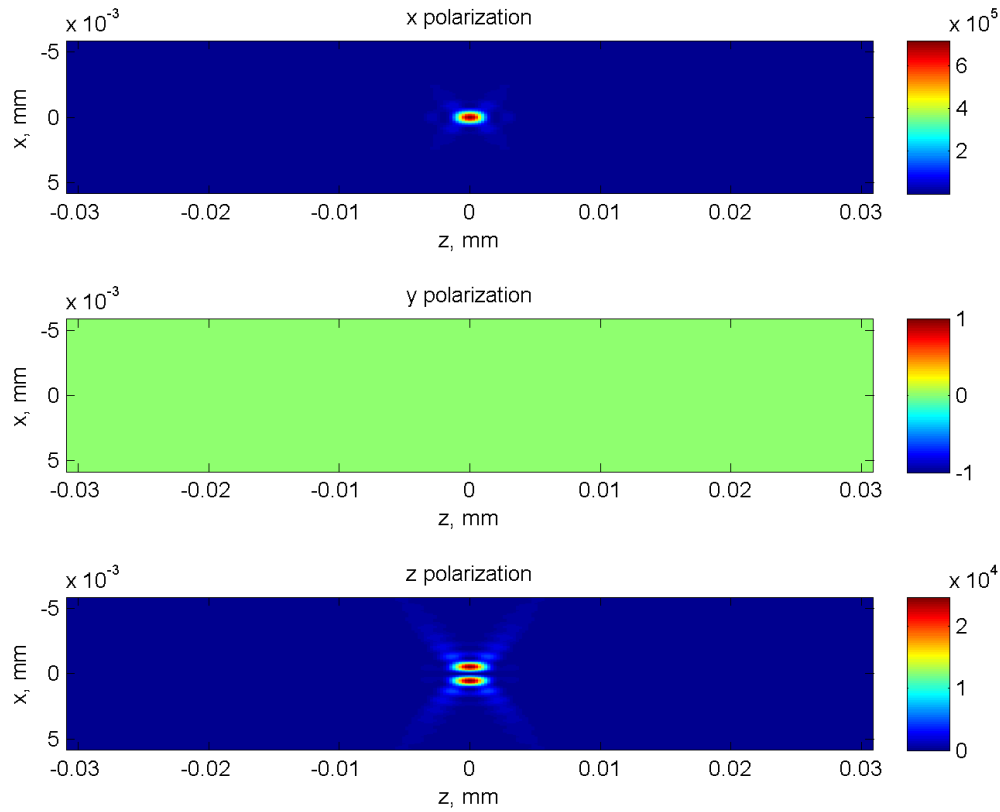


Figure 7.9: Intensity distribution at the focus for unaberrated x-polarized laser beam focused with 0.7 NA objective. The colorbar indicate difference in the magnitude for x, y and z polarized components.

The length of the laser induced structure was estimated by choosing a certain threshold and measuring the distance where light intensity is exceeding it. As a result, several approximations are involved. First, it is assumed that $\Delta n = n_e - n_o$ induced by the nanograting is along the induced structure. Second, each slice in the z direction equally contributes to the total retardance. If only non-linear absorption is responsible for electron excitation when the induced structure length should be dependent on I^n , where n is number of photons required for electron excitation from the valence to the conduction band. However, electron excitation depends on several mechanisms. Here we decided to compare the induced structure length by analyzing the intensity distribution. Moreover, qualitative behaviour of the induced structure length with a focusing depth does not depend on the nonlinearity degree. The intensity threshold was chosen in such a way that the obtained results would be closer to the measurements. Retardance was

calculated using $\Delta n = -4 \times 10^{-3}$ [49], which is a typical value for laser induced nanograting in fused silica.

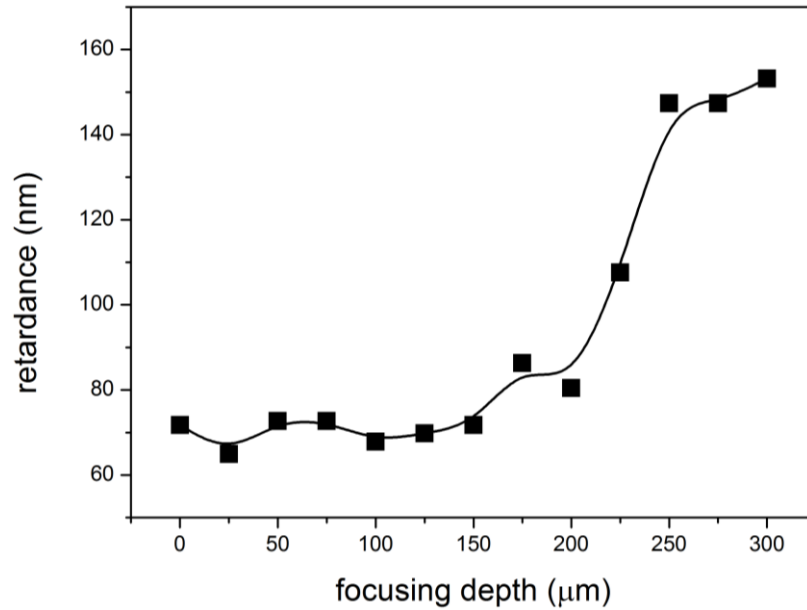


Figure 7.10: Modelled retardance dependence on the focusing depth into the substrate of fused silica.

The modelling results (Figure 7.10) qualitatively match with the measurements, indicating that the main source of retardance increase with focusing depth is spherical aberration. Indeed, we can see that the calculated retardance values are very close to those measured in the experiment.

7.3 Retardance dependence on the numerical aperture

The retardance of the birefringent structure is a product of refractive index difference multiplied by the length of the structure. It is known that length of the laser induced structure is related to the numerical aperture of the focusing optics. The lower the numerical aperture is the longer the structure. Additionally, lower NA means a bigger spot size which is important for producing homogeneous polarization converters in a reasonable amount of time. However, the numerical aperture cannot be infinitely reduced, as at low values the self-focusing threshold will be reached before permanent damage occurs, as a result instead of localized material modification one will obtain filamentation and supercontinuum generation, as it was discussed in Paragraph 2.3.1.

For efficient operation of birefringent optical elements high retardance is normally required. A series of experiments were performed to determine a writing regime where such high values of retardance can be achieved. By scanning lines with a 1 μm inter-distance, homogeneous structures of 30 μm in diameter were written. Measurements of multiple line structures are less sensitive to the focusing than a single line characterization, and thus a smaller measurement error is produced. In the writing procedure the average femtosecond laser power was varied from 50 mW (below nanograting formation threshold) to 4.5 W and the repetition rate was set to 200 kHz.

The Abrio system is designed primarily for biological specimens, which exhibit very low levels of birefringence. As the system is operating at 515 nm, the highest retardance it can measure is 257 nm. As a result, measured retardance shows an artificial decrease for retardance higher than that. If higher retardance values are needed to be characterized, a simple unwrapping procedure must be performed. The decrease of the retardance due to measurement limitation can be distinguished by measuring the slow axis orientation. If the measured value exceeds the 250 nm limit, the slow axis is rotated by 90 degrees. After the correction, retardance of more than 350 nm was measured. Such high values allow writing a half-wave plate for 700 nm in a single scan.

The optimum parameters to induce a high retardance were determined by a set of experiments. The structures were written with two different translation speeds (1 mm/s and 2 mm/s) at energies up to 7.5 μJ and later characterized with a quantitative birefringence measurement system (CRi Abrio) and Olympus BX51 optical microscope. The measured retardance dependence on pulse energy at two different focusing conditions clearly demonstrates the possibility of reaching high retardance values exceeding even the half-wave value (258 nm) for 530 nm (Figure 7.11). One can see that with lower NA optics, higher energy is required for forming nanogratings and, as a result, the structures with the same retardance are less uniform. However, the retardance saturates at much higher values allowing the writing of a half-wave retardance waveplate in a single scan.

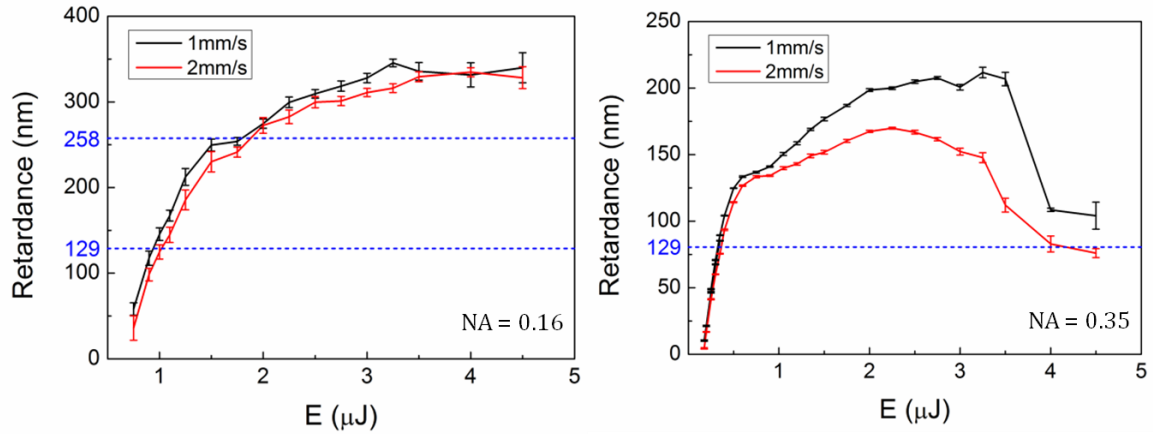


Figure 7.11: Retardance values for nanogratings written with 0.16 NA aspheric lens (Top) and 0.35 NA objective (Bottom) at two translation speeds (1 and 2 mm/s). Dotted lines indicate retardance values of quarter and half wave for 530 nm.

7.4 Conclusions

The spectral properties of femtosecond pulse induced nanogratings were characterized for a wide range of wavelengths from 200 nm to 1550 nm. The transmission spectrum of Type 2 modification has two pronounced absorption bands, which are attributed to E' and ODC(II) defects. In contrast, Type 1 modification only exhibited an absorption band for E'. The main part of the optical losses are attributed to the scattering of inhomogeneous structure. The obtained results were similar for the first and second harmonic of laser irradiation. The dispersion of retardance exhibits an unusually sharp decrease at about 450 nm. A simple form birefringence theory does not predict such behaviour indicating that a more complex model should be invoked. At longer wavelengths the retardance value reaches constant value which extends to at least 1550 nm.

In the optimized process a retardance of more than 200 nm can be induced in a single scan with relatively high writing speed. Higher retardance values are achieved by the stacking of several layers. As a result polarization sensitive devices can be fabricated for various wavelengths in the visible and near infrared with losses as low as 10% (at 1550 nm).

Additionally, we explored the possibility of inducing a permanent isotropic refractive index increase with sub-picosecond light pulses. We demonstrate that at high writing speed (or when the number of pulses is relatively small) and low pulse energy the isotropic refractive index increase can be induced with pulses as long as 800 *fs*.

The retardance induced with a high NA objective depends on the focusing depth. This effect arises mainly due to spherical aberration caused by the refractive index mismatch at the surface of the fused silica substrate. By increasing the focusing depth to 300 μm we managed to almost double the value of induced retardance.

Finally, using aspheric lenses as low as 0.16 NA we managed to induce retardance higher than a half-wave for 532 nm in a single scan. This allows the writing of birefringent optical elements with a relatively high speed avoiding the need to stack several layers. These findings were later explored for fabrication of efficient optical elements with space variant birefringence.

Chapter 8. Polarization sensitive elements

8.1 Introduction

In conventional anisotropic optical elements, such as linear polarisers or wave plates, optical properties are uniform in the transverse direction. These elements are widely used to manipulate light polarization: purify, rotate, transform. All operations are identical for each point of such an element. However, there is an increasing interest to produce polarization diffractive optical elements, i. e. elements where anisotropic properties spatially vary across the structure, due to the variety of prospective functions, such as beam splitters [60,128], azimuthal and radial polarization state converters [129,130] or coronagraphs [131]. In certain cases a single spatially variant polarization element can effectively replace a group of conventional polarization elements. Potentially, they also could be applied for birefringent memory read-out. Such elements can be seen as an analogy to conventional diffractive optics, which found numerous applications from complex beam shapers to Fresnel lenses in mobile phones' LED flash. Currently spatial polarization control is achieved by several technologies including liquid crystal based spatial light modulators [128], segmented linear polarizers [132], photolithographically produced subwavelength gratings [60,133] and materials containing photoalignment chromophores [134,135].

Spatial light modulators allow dynamic tuning of its diffractive properties, which is desirable for many applications as it allows easily change the diffraction pattern. However, liquid crystals, which are the basis of spatial light modulators, can modulate only one polarization component at a time. Essentially, a liquid crystal modulator is an array of waveplates, where retardance can be arbitrarily set for each waveplate. The slow axis, however, is uniform across the array and cannot be manipulated. As a result, full control of polarization requires the light to impinge on a spatial light modulator at least twice, making the configuration of the experiment non-trivial. Frequently additional optical elements must be included to achieve the desired result, for instance radial polarization (Figure 8.1). In simple

cases, only one spatial light modulator can be used. However, for full polarization control separate devices must be combined.

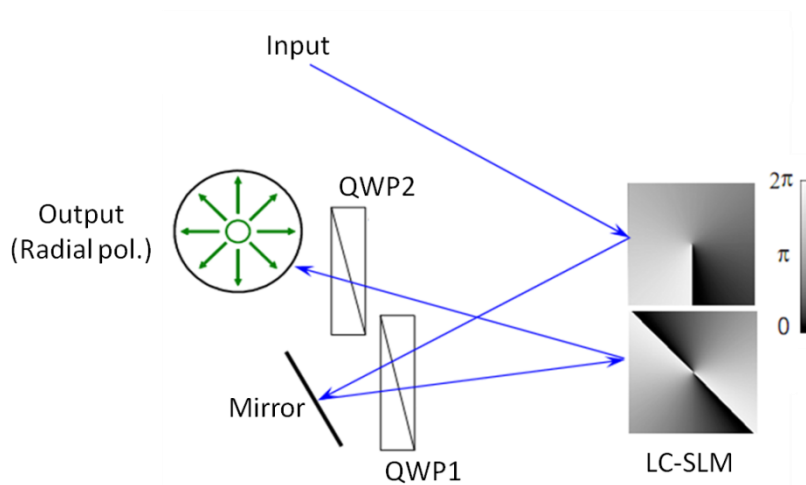


Figure 8.1: Scheme to generate radial polarization using a liquid crystal spatial light modulator (SLM) (Source: [134]). Incident linear polarization after being reflected from the SLM is passed through a quarter wave plate, then again reflected from the SLM and after passing through the second quarter wave plate radial polarization is generated.

This inevitably introduces losses exceeding tens of percents. Additionally, they are expensive and operate only at moderate laser fluences (200 mJ/cm^2). Also liquid crystal based devices tends to suffer from thermal drift, which causes uncontrolled change of the polarization properties. The advantage of spatial light modulators is their ability to dynamically change optical properties of the light on a time scale of less than 200 ms.

Simple passive spatially variant elements can be fabricated by joining small segments of polarizers or waveplates together to achieve the required effect. The segmentation technique is, however, limited to only a few simple geometries and suffers from low resolution, leading to losses due to diffraction and spatial filtering. Also elements produced in such a way are costly as it requires high precision and involves such time consuming procedures as polishing, gluing and aligning separate parts of the final optical element. The positive side of such elements is their high optical quality and ability to be used at high powers. In comparison with

spatial light modulators based set-ups, this technique allows the production of much more compact and easy to use polarization control elements.

Birefringent elements can also be written using azobenzene containing materials. The birefringence is induced in an initially isotropic material by axis selective *trans-cis-trans* photoisomerization and the subsequent orientation of the azobenzene groups along laser beam polarization [136]. It is possible to write a polarization diffraction grating directly exposing the material to the interference pattern of two circularly polarized beams [135]. Thus it is easy to use for fast mass production, leading to potentially low manufacturing cost. However, such polymeric substances, currently, lack stability and tend to return to the random molecule distribution even at the room temperature.

A photolithographic technique was used to create a subwavelength grating which would exhibit form birefringence [60,133]. Metal stripes (Ti and Au) using contact photolithography and lift-off were formed on the surface of a GaAs wafer into a subwavelength structure. Alternatively, using wet etching, dielectric gratings can be fabricated. Although this method allows complex geometries and easily controlled final parameters, due to restrictions of available resolution and the requirements for a high aspect ratio, a device working only with 10 μm irradiation was demonstrated. Recently, a similar technique was used to fabricate devices operating in NIR (1 μm). The advance to shorter wavelengths was achieved by engineering the refractive index distribution. However, such technology inherits all drawbacks of the photolithographic technique, including the requirement for a clean-room environment, high quality requirements for mask alignment during pattern transfer and long pre and post production.

8.2 Polarization diffraction grating

8.2.1 Working principle

The polarization diffraction gratings, unlike scalar diffraction gratings, which are based on periodic modulation of either phase or amplitude, introduce a periodic spatial variation of polarization and thus lead to polarization dependent

diffraction [60]. Additionally, the polarization of diffracted orders in general is different from that of the incident beam. Essentially, such diffraction grating acts as a polarization beam splitter. A polarization grating can be fabricated in two ways. First (Type 1), one can introduce periodic spatial variation of retardance by the use of a spatial light modulator [128], or surface etching of a birefringent material such as lithium niobate [133] or crystalline quartz. Second (Type 2), the grating can be produced by modulating the angle of the slow axis [60]. When a beam with uniform polarization propagates through the grating the polarization and phase of the transmitted light field becomes periodic in space. As a result, this will yield discrete diffraction orders in the far-field. Both types of gratings are sensitive to the state of polarization of the incident beam, however they act differently. The first type of polarization grating will split the incident light into two orthogonal linear polarizations. The energy carried by each diffraction order is proportional to the power of x and y linearly polarized components present in the incident beam. The second type, will act as a circular polarization beam splitter, separating the incident light into two circularly polarized beams with opposite handedness. This time, the energy of diffraction orders will be defined by the amount of left and right handed circular polarizations present in the incident beam. The property of beam separation depending on the polarization state can be exploited for measurements of polarization states avoiding the need of any moving part.

The Type 2 polarization diffraction grating can be fabricated using subwavelength gratings. In this case, modulation of the slow axis will be achieved by locally varying the orientation of the subwavelength grating [60]. The polarization grating then will consist of two periods; one much larger than the wavelength of incident light and another smaller than it. Theoretical analysis of Type 2 polarization gratings performed using the Jones matrix formalism reveals that the intensity distribution between maxima depends on the retardance value [60,132]. The diffraction efficiency can be evaluated by calculating amplitudes of diffraction orders:

$$\zeta_0 = \left| \frac{1}{2}(t_x + t_y e^{i\phi}) \right|^2, \quad (8.1)$$

$$\zeta_1 = \left| \frac{1}{2}(t_x - t_y e^{i\phi}) \langle \mathbf{E}_{in} | \mathbf{LH} \rangle \right|^2, \quad (8.2)$$

$$\zeta_{-1} = \left| \frac{1}{2}(t_x - t_y e^{i\phi}) \langle \mathbf{E}_{in} | \mathbf{RH} \rangle \right|^2, \quad (8.3)$$

where $\zeta_0, \zeta_1, \zeta_{-1}$ are amplitudes for the 0, 1 and -1 diffraction orders respectively, while t_x and t_y are transmission coefficients for polarization parallel and perpendicular to the subwavelength grating grooves. Here we consider that $t_x = t_y = 1$. The phase shift due to retardance is indicated as ϕ and expressed as $\phi = \frac{2\pi\Delta}{\lambda_0}$ where Δ is retardance, and λ_0 is wavelength of the incident light in vacuum. Dirac brackets denote polarization states: $|\mathbf{E}_{in}\rangle, |\mathbf{LH}\rangle, |\mathbf{RH}\rangle$ are Jones matrices for incident light, left hand and right hand polarizations. In helicity base right hand circular $|\mathbf{RH}\rangle$, left hand circular $|\mathbf{LH}\rangle$ and linear horizontal polarizations $|\mathbf{LHP}\rangle$ are expressed:

$$|\mathbf{RH}\rangle = \begin{pmatrix} 1 \\ 0 \end{pmatrix}, \quad (8.4)$$

$$|\mathbf{LH}\rangle = \begin{pmatrix} 0 \\ 1 \end{pmatrix}, \quad (8.5)$$

$$|\mathbf{LHP}\rangle = \frac{1}{\sqrt{2}} \begin{pmatrix} 1 \\ 1 \end{pmatrix}, \quad (8.6)$$

After applying to Eq. 1, given the assumption that the 0, 1 and -1 diffraction orders are expressed as:

$$\zeta_0 = \frac{1}{2}(1 + \cos \phi), \quad (8.7)$$

$$\zeta_1 = \frac{1}{2}(1 - \cos \phi) \langle \mathbf{E}_{in} | \mathbf{LH} \rangle^2, \quad (8.8)$$

$$\zeta_{-1} = \frac{1}{2}(1 - \cos \phi) \langle \mathbf{E}_{in} | \mathbf{RH} \rangle^2. \quad (8.9)$$

We can see from (3) that increasing the retardance leads to the energy transfer from the 0 order to adjacent ones. When the phase shift is equal to π , the 0 order completely disappears. Additionally, the incident light polarization state is preserved in the 0 order. The -1 and 1 orders are right and left hand circularly polarized. In our case, (assuming a retardance value of ~ 90 nm) about 20% of

incident light should be diffracted into -1 and 1 orders, while the other 80% remains in the 0 order.

8.2.2 Experimental results

In our experiment a grating of dimensions $1\text{ mm} \times 1\text{ mm}$ (Figure 8.2) was produced by successively writing 1 mm long lines separated by $2\text{ }\mu\text{m}$ at a speed of $200\text{ }\mu\text{m/s}$. Before writing a new line the half-wave plate was rotated by a certain angle so that the final period would be $125\text{ }\mu\text{m}$. The period is defined as the distance over which the polarization azimuth rotates by 180° . The total processing time was about 1 hour, which can be significantly reduced by optimizing the manufacturing parameters.

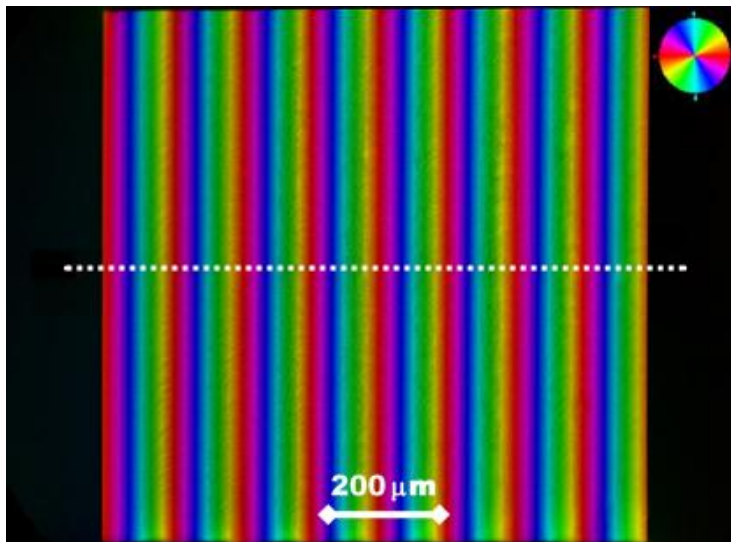


Figure 8.2: Quantitative birefringence microscopy image of polarization diffraction grating. Pseudo colour indicates azimuth of the slow axis.

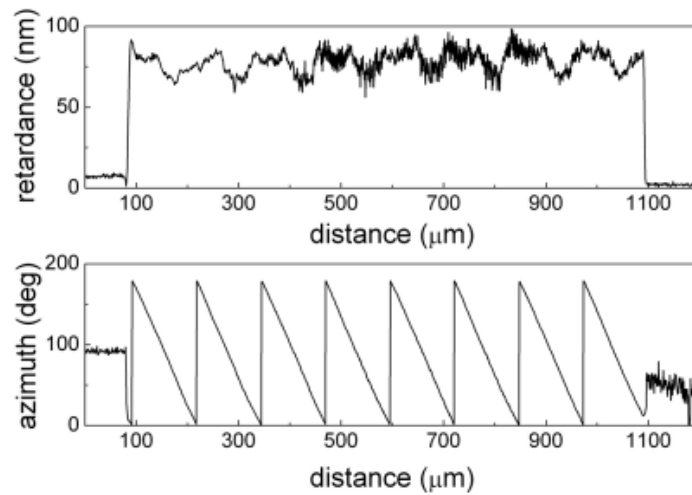


Figure 8.3: Retardance (Top) and azimuth (Bottom) profiles taken along the white dotted line.

With a quantitative birefringence microscope (Abrio CRi) we confirmed the successful realization of the desired variation of the slow axis and measured an induced retardance of about 90 nm (Figure 8.3) for 515 nm wavelength. However, undesirable modulation of retardance occurred across the grating. The variation of slow axis is seen by polarized light as a phase modulation. For circular polarization, this grating is effectively a prism, which deflects the beam. This was confirmed with measurements of phase variation performed on a digital holographic microscope (Figure 8.4).

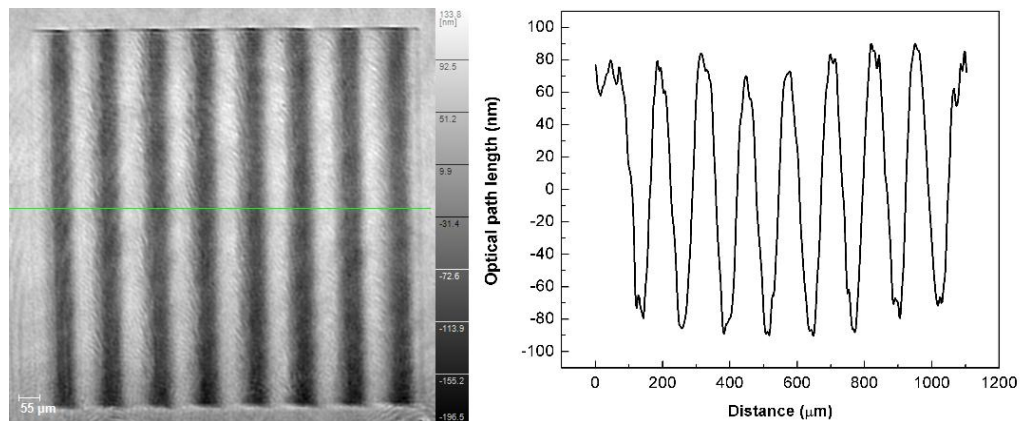


Figure 8.4: (Left) Grayscale map representation of the birefringent grating phase variation measured with a digital holography microscope. (Right) An optical path variation (taken along the green line) for linear polarization produced by a periodic pattern of the slow axis orientation.

The directional dependence of written lines was observed when the laser beam polarization was at $\sim 45^\circ$ to the writing direction (Figure 8.5). The imprinted lines were asymmetric, with one edge less defined than the other. Reversing the scanning direction correspondingly reversed this feature. Consequently, the lines did not overlap homogeneously thus degrading the quality of the produced diffractive element. It is worth mentioning that scanning in both directions results in a pattern with the period of double scanning step (Figure 8.5). If scanning is performed only in one direction then the period, which appears due to scanning, is as expected. Another interesting feature is that the homogeneous retardance distribution can be observed only for one scanning direction (middle structure in Figure 8.5). We relate this effect to light interaction with a material at the boundary of the line, thus the observed directional dependence has a different nature compared to previously reported quill and non-reciprocal writing [14,17]. As a result of this asymmetry, the written tracks 'join' differently together depending on the writing direction. If writing is performed in both directions two adjacent lines merge together comprising a period twice that of the scanning step (Figure 8.5). This was confirmed by measuring the diffraction pattern of the laser beam transmitted through the written structure. Also the polarization direction plays an important role in this case. Depending on the polarization direction with respect to the scanning direction one can achieve a birefringent structure of different quality. Only one of two possible combinations gives a smooth distribution of retardance. To avoid this problem, the polarization grating was written by scanning only in one direction.

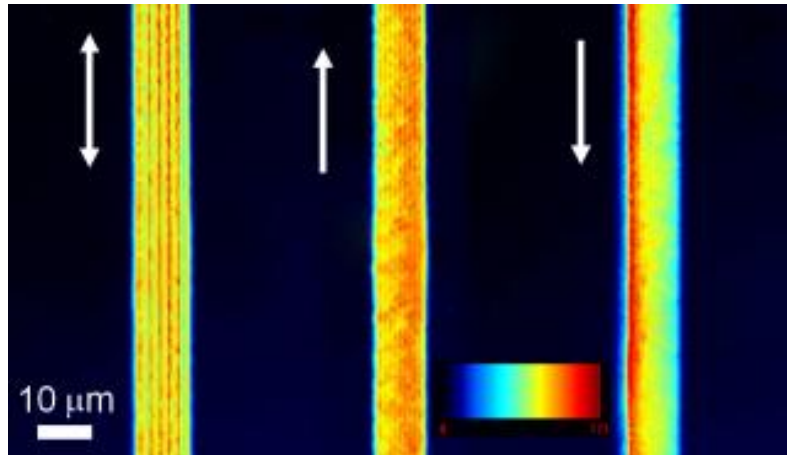


Figure 8.5: Directional dependence of written lines when the polarization azimuth is at 45° to the writing direction. Structures are produced of lines separated by $1\ \mu\text{m}$, white arrows indicate the sample translation direction. If lines are written by translating the sample in both directions two adjacent lines merge together. The effect is clearly seen on the first structure.

Dependence of structural properties, determined by Raman spectroscopy, was also reported to be dependent on the polarization [137]. The source of polarization dependence can be induced by the ellipticity of light introduced by the reflection from dielectric mirrors. As a result this can change with polarization azimuth. However, the polarization distortion effect was minimized by placing a half-wave plate just before the objective, thus no polarization mixing should occur. Another source of polarization dependence can arise from light interaction with the boundaries of written lines, which could also explain a complex pattern observed in the optical image of the grating (Figure 8.6). It is known that a polarization parallel to the writing direction produce a smoother modification than the perpendicular.



Figure 8.6: Optical image of the polarization grating. A peculiar pattern could be clearly seen. The smoothness of the induced structure strongly depends on the polarization of the writing beam with respect to the writing direction.

The diffraction properties were characterised by directing light from a Nd:YAG (532 nm) (Figure 8.7) and a HeNe (633 nm) (Figure 8.8) continuous wave lasers through the diffraction grating and onto a white screen or a beam profile meter. The different diffraction patterns, with respect to the incident polarization state, can be seen clearly in Figure 8.7, which shows far field diffraction images for different incident polarizations. The linearly polarized beam was diffracted into 0, -1 and 1 orders with the ratio of the amplitudes being 0.12:1:0.11 (Figure 8.8) for measurements taken at 633 nm. For a left hand circular polarization only 0 and 1 diffraction orders were present (amplitude ratio 0.21:1:0), while right hand circular polarization resulted in 0 and -1 diffraction orders (amplitude ratio 0:1:0.18). This proved that the observed diffraction was caused by the space variant polarization of the written structure. Based on the ratios we estimated a retardance of 89 nm at 633 nm, which correlates well with independent birefringence measurements made using the Abrio CRi system.

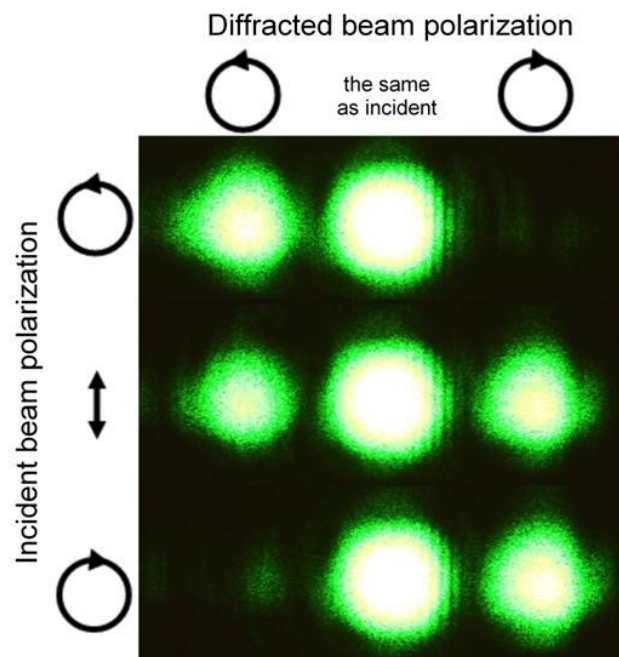


Figure 8.7: Far-field diffraction images for linear and circular incident polarizations. Incident polarization state is indicated on the left side. The white light is due to saturation of the CCD camera.

An extra diffraction, arising due to the periodic nature of the line scanning, appeared at larger angles. It was insensitive to the incident polarization and accounted for 4% of the incident light.

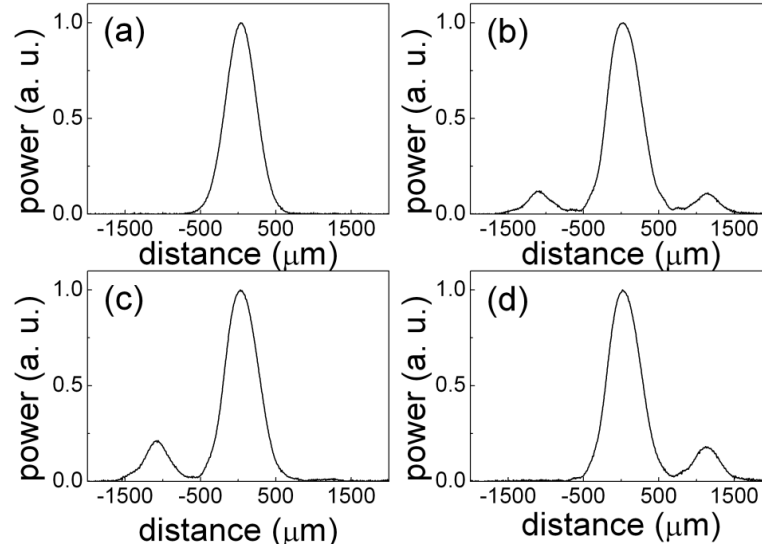


Figure 8.8: Diffraction profiles measured for HeNe laser with beam profile meter: a) incident beam profile, b) diffraction pattern for linear polarization, c,d) diffraction patterns for left and right handed circular polarizations.

For comparison, another polarization diffraction grating 2×2 mm size was fabricated using a 0.16 NA microscope objective, achieving a longer Rayleigh range (Figure 8.9), i. e. extending the birefringent structure and adding more retardance. The polarization grating was written with a 22.5 μm period, focusing a pulse train of 200 kHz with 1.25 μJ pulse energy. The induced retardance was of about 257 nm, which is close to a half-wave for 515 nm. The efficiency of the grating was much higher as compared to that discussed above. More than 80% of the incident light was diffracted into -1 and 1 orders. As it was explained above, the polarization grating with higher retardance (close to π phase shift) works the most efficiently as the zeroth order is effectively suppressed. A slight change in the zeroth order can be explained by unwanted retardance modulation present in the grating.

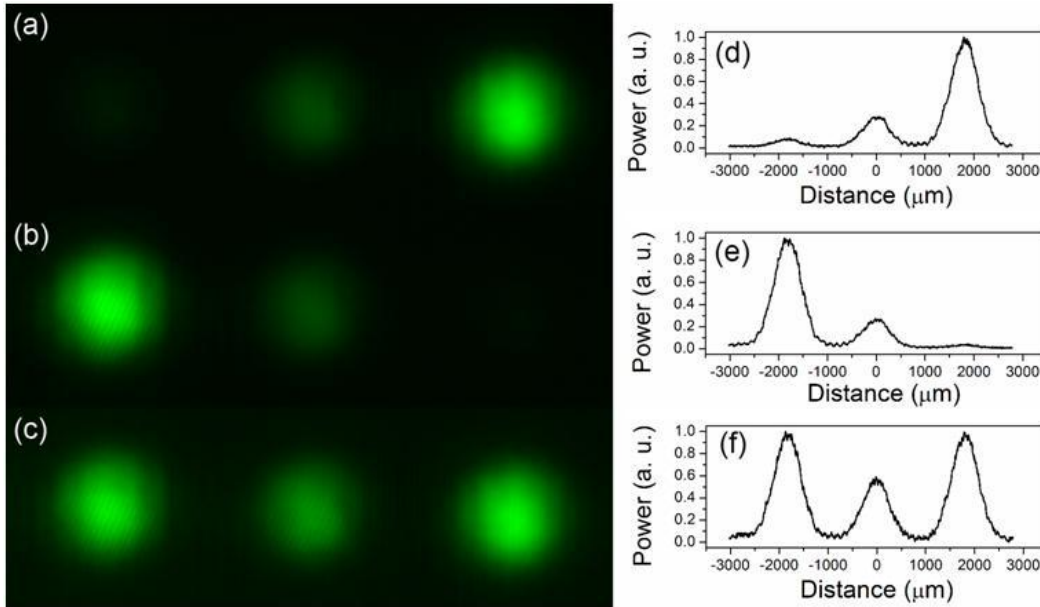


Figure 8.9: Far-field diffraction images for circular (right (a) and left (b)) and linear (c) incident polarizations. Respective profiles measured for 515 nm with a beam profile meter: (d,e) diffraction patterns for right and left handed circular polarizations respectively, (f) diffraction pattern for linear polarization.

If an extra retardance is added by placing a liquid crystal compensator in the light pass of the microscope, the affected zone appears coloured under crossed polarizers (Figure 8.10). This coloration is well known in polarization microscopy, and occurs when the optical path length difference due to birefringence is in the order of wavelength λ_c :

$$\lambda_c = |n_e - n_o|t_p. \quad (8.10)$$

For λ_c ordinary and extraordinary waves propagating through birefringent material experience a phase shift equal to 2π or one wavelength and thus polarization at this wavelength remains unchanged. After the second polarizer oriented perpendicular to the first one, the light with λ_c will be suppressed. If this wavelength is located in the visible, the output light lacks this component and appears as its complimentary colour. If the retardance of the sample is not sufficient a waveplate with additional retardance can be inserted between two crossed polarizers shifting λ_c into the visible spectrum.

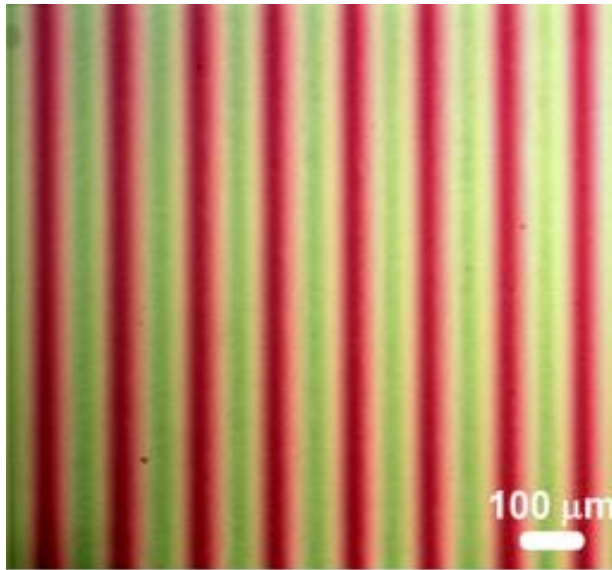


Figure 8.10: Coloration of birefringent structure in crossed polarizers when additional constant retarder is added.

Obviously, the effect depends not only on the retardance, but also on the orientation of the slow axis. If the first polarizer is oriented along the fast or slow optical axis, the coloration effect won't be observed. The maximum effect is observed when the incident polarization is at 45° with the slow axis. The ability to control retardance and the slow axis with a submicron resolution and thus to print coloured graphics inside glass, makes the technique attractive for security marking (Figure 8.11).

If the technique would allow the printing of "red", "green" and "blue" pixels which will differ by the amount of retardance, one could easily cover the whole palette of colours. The resolution of $2\ \mu\text{m}$ would be more than enough, e.g. 400 DPI (dots per inch) corresponds to a $20\ \mu\text{m}$ spot diameter if a RGB mode is considered. The only problem is to achieve sufficiently high retardance values needed for the coloration. This can be partially solved using low NA objectives, which have longer Rayleigh range compared to a high NA objective used in this experiment. The retardance is expected to increase at the expense of lower spatial resolution.



Figure 8.11: Birefringent rose printed in silica glass using ultrashort light pulses. (Color contrast is enhanced).

8.2.3 Birefringence measurements with polarization grating

As was described above the polarization grating effectively works as a circular polarization beam splitter. The intensity of left and right diffraction orders is directly proportional on the state of the incident light polarization. It is known that any polarization state can be seen as a superposition of two circular polarizations with opposite handedness. On the other hand, circular polarization propagating through a birefringent material will, in general, become elliptically polarized. By measuring the ellipticity of the polarization one can fully describe birefringent properties of the investigated material.

Here the Jones matrix formalism is employed to demonstrate the possibility of measuring retardance with a polarization diffraction grating. A single optical axis birefringent object can be described by the following matrix:

$$M_{OBJ} = \begin{pmatrix} e^{i\Delta\phi} \cos^2 \theta + \sin^2 \theta & (e^{i\Delta\phi} - 1) \cos \theta \sin \theta \\ (e^{i\Delta\phi} - 1) \cos \theta \sin \theta & e^{i\Delta\phi} \sin^2 \theta + \cos^2 \theta \end{pmatrix}, \quad (8.11)$$

where $\Delta\phi$ is the phase retardation between x and y polarized light and θ is the fast axis angle with respect to the x axis. Without any loss of generality, let us assume that the left handed circularly polarized light is propagating through this object. As

was stated above a birefringent diffraction grating can be described as a circular polarizer (left handed M_{CPLH} or right handed M_{CPRH}):

$$M_{CPLH} = \frac{1}{2} \begin{pmatrix} 1 & -i \\ i & 1 \end{pmatrix}, \quad (8.12)$$

$$M_{CPRH} = \frac{1}{2} \begin{pmatrix} 1 & i \\ -i & 1 \end{pmatrix}. \quad (8.13)$$

The whole system is then written as follows:

$$E_{OUT} = M_{CPLH} M_{OBJ} E_{LCP}. \quad (8.14)$$

When the output electric field is equal to:

$$E_{LOUT} = \frac{1}{2\sqrt{2}} (e^{i\phi} + 1) \begin{pmatrix} 1 \\ i \end{pmatrix} \quad (8.15)$$

$$E_{ROUT} = \frac{1}{2\sqrt{2}} (e^{i\phi} - 1) e^{2\theta} \begin{pmatrix} 1 \\ -i \end{pmatrix} \quad (8.16)$$

In the experiment we measure intensity:

$$I_{LOUT} = E_{LOUT} E_{LOUT}^* = 1 + \cos \phi, \quad (8.17)$$

$$I_{ROUT} = E_{ROUT} E_{ROUT}^* = 1 - \cos \phi. \quad (8.18)$$

As one can notice the described values are already normalized. Thus, during the experiment both diffraction orders need to be measured to normalize the intensity.

Finally the retardance can be expressed as follows:

$$\phi = \frac{\lambda}{2\pi} \arccos(I_{LOUT} - 1). \quad (8.19)$$

8.3 Polarization converter

8.3.1 Introduction

Another application of femtosecond laser-induced form birefringence is a polarization converter. Typically in optics two types of polarization are discussed: linear and circular. Both of them are spatially homogeneous, i.e. in every part of the light beam the polarization state is the same. However, recently an increasing interest arose for spatially variant polarization states. The most examined ones are

radial and azimuthal polarizations (Figure 8.12). Recently, such beams have attracted a significant attention largely because of their unique properties under high numerical aperture (NA) focusing. Numerical calculations have shown that tighter focus spots can be obtained using radial polarization, caused by a strong and localized longitudinal field component [138]. This effect has been experimentally confirmed by several groups [139,140] and has already found applications in high resolution imaging such as confocal microscopy, two-photon microscopy, second harmonic generation microscopy [141], third-harmonic generation microscopy [142], and dark field imaging [143]. Radial polarization also ideally suits for surface plasmon excitation with axially symmetric metal/dielectric structures [144], because plasmon excitation is strongly dependent on the excitation polarization. Efficient localized plasmon excitation can be explored also for cancer treatment [145]. The large longitudinal electric fields generated with radially polarized beams are also explored for particle acceleration [146].

Three-dimensional focus engineering is another application where beams with exotic polarizations can be used. By controlling the polarization azimuthal angle φ_0 from the radial direction, a focal field with a transverse flat-top profile can be created [140]. Introducing a pupil plane phase or amplitude mask provides additional degrees of freedom and enables extra focal field profile control, so that a highly homogeneous electric field distribution in three dimensions is achieved [147]. Recently, even more exotic focal field distributions, such as an optical “bubble” [147] or optical “needle” [22], have been implemented. Additionally, the high degree of symmetry inherently present in radial/azimuthal polarization leads to efficient interaction with matter without an undesirable anisotropy produced by a linearly polarized light [149,150]. The main hindrance to a widespread use of such polarization modes is the lack of simple and cost-effective ways to generate them.

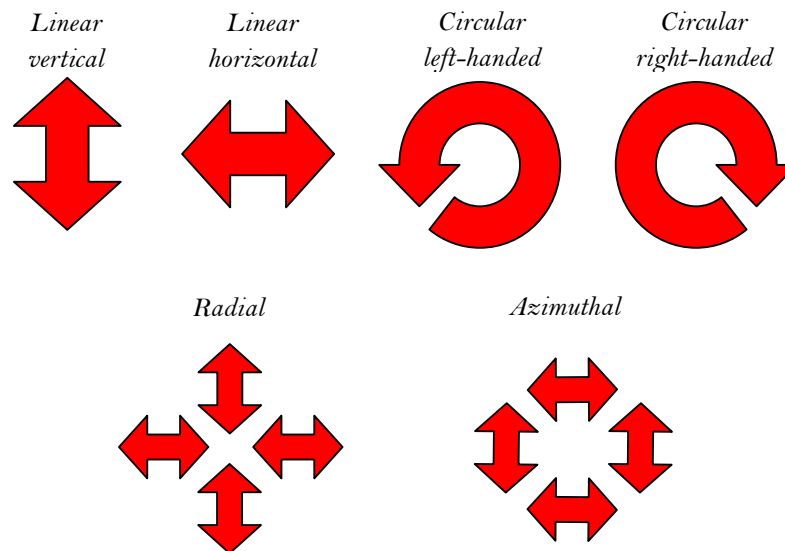


Figure 8.12: Schematic representation of various polarization states. In the upper row all polarizations are spatially homogeneous, while in the lower row both polarizations are spatially variant.

Spatially variant polarization states are very sensitive to any phase change, which can distort the initial high symmetry. For instance, reflection from a dielectric mirror tends to strongly distort the intensity pattern of radial polarization as a result of the phase shift. The problem can be solved by generating the desired spatially variant polarization just before the sample. This mostly requires very compact polarization generation setup. Additionally, such a simple task as polarization rotation turns out to be very challenging for cylindrical vector beams. Thus the polarization generation technique should be not only efficient, but also provide a compact setup and polarization state control options.

8.3.2 Methods for spatially variant polarization generation

Here I will shortly overview currently used methods for spatially variant polarization generation. Depending on whether the generation method involves amplifying medium the techniques are split into two groups: passive and active.

The active methods are based on forcing the laser to oscillate in cylindrical vectorial mode by adding an axial birefringent or dichroic element into the cavity [151]. One of the first demonstrations were done by inserting a calcite crystal into the cavity, so that the crystal axis would be parallel to the optical axis

of the cavity [152]. Due to birefringence e and o polarizations the divergent laser beam experience slightly different magnifications inside of the crystal. The added central stop aperture allows discriminating one of the spatially variant modes because of higher loss. The birefringent crystal can be replaced with axicon, which due to different Fresnel transmission coefficients for s and p polarizations will act as an axial dichroic element. The most effective apex angle of the axicon is Brewster's angle [153]. The dichroic element allows simplifying the cavity design, as a single element acts as a mode separator and selector.

The passive methods are based on converting spatially homogeneous polarizations (linear or circular) into spatially variant cylindrical vector polarizations. Similarly to intracavity generation methods, axial birefringence or dichroism can be also utilized for polarization conversion. Recently, a single charged circularly polarized optical vortex was converted into radial/azimuthal polarization with calcite crystal [154]. The crystal axis was aligned parallel to the beam propagation direction. Later radial or azimuthal polarization was selected with an aperture which could be quite tricky. The optical vortex was used to pre-compensate Berry phase which occurs for circular polarization in this case [151].

Another passive method is based on local polarization rotation inside of a liquid crystal cell. The device is made of a nematic liquid crystal sandwiched between linearly and circularly rubbed plates. Due to circular rubbing the liquid crystal molecules rotate from the initial linear rubbing direction to a spatially variant distribution of the second plate. A very popular technique for polarization manipulation is based on a liquid crystal spatial light modulator. As a spatial light modulator cannot directly manipulate polarization, the desired electric field distribution is achieved by a two step procedure, which requires reflecting the beam twice from a spatial light modulator [134,155]. This can be done by splitting the active area of the modulator into two parts or by using two modulators simultaneously. The first spatial light modulator provides pure phase modulation to the incoming beam to either correct certain aberrations in the system or to add the desired phase pattern to the beam. The combination of the quarter-wave plate and the second modulator essentially forms a polarization rotator, where the

amount of rotation is determined by the phase retardation of each pixel on the spatial light modulator. Properly designing the phase pattern on the second spatial light modulator allows the input linear polarization to be converted into any arbitrary polarization distribution, including cylindrical vector beams. Another radial/azimuthal polarization generation method is based on segmented half-wave plate converters. By gluing together several segments of a half-wave plate with the appropriately arranged slow axis one could convert linear polarization into radial-like polarization. Such a polarization state will have a step-like electric vector orientation change. After this segmented converter, an additional filtering can be involved in order to generate a pure radial polarization. Alternatively, polarization converters can be produced with spatially variant subwavelength gratings [129], which would generate azimuthally symmetric polarization from conventional linearly or circularly polarized Gaussian modes. The subwavelength gratings will induce form birefringence. The working principle of such devices is similar to the mentioned above segmented half-wave plates. The advantage of this design is that the direction of the subwavelength gratings can change continuously, thus pure radial/azimuthal polarization can be generated just by one optical element. The period of the gratings should be smaller than the wavelength of light, otherwise the nanostructure will not behave as an uniaxial optical crystal. Photolithography, which is usually used for the fabrication of such elements, has a limited resolution that restricts the wavelength of operation to the infrared. Although, it is possible to achieve high resolution using currently available photolithography techniques, the complexity of the process does not pay-off with the obtained quality. In this respect, the nanogratings induced by femtosecond laser irradiation are a perfect choice for devices working in the visible and near-infrared.

| Method | Advantages | Disadvantages |
|--|--|---|
| Spatial Light Modulator | Commercially available Flexible | Costly Bulky Complicated setup Power limited |
| Liquid crystal cell | Commercially available Easy to use Compact | Less flexible Power limited |
| Intracavity generation | High power | No flexibility Special laser design required Costly |
| Birefringent crystal | Relatively low cost High power | No flexibility Requires polarization filtering |
| Subwavelength grating via photolithography (for CO ₂ laser) | Flexible Relatively low cost Easy to use High power | Limited to far-infrared Complicated fabrication |

Table 8.1: Summary of polarization generation methods.

8.3.3 Form birefringence based polarization converters

Depending on the induced retardance, two types of converters can be constructed (Figure 8.13). The first type is a spatially variant quarter wave plate, which converts an incident circularly polarized beam into a radially or azimuthally polarized optical vortex. The second type, is a spatially variant half-wave plate, which converts incident linear or circular polarization into radial/azimuthal polarization or an optical vortex respectively. Both types differ by the amount of required retardance and orientation of the slow axis (Figure 8.13).

Using Jones matrix formalism we can apply a rotation operation to the matrix of a quarter wave plate. Then the spatially variant quarter wave plate can be described by the following matrix:

$$M_{QW} = \begin{pmatrix} \cos^2 \theta + i \sin^2 \theta & (1 - i) \cos \theta \sin \theta \\ (1 - i) \cos \theta \sin \theta & i \cos^2 \theta + \sin^2 \theta \end{pmatrix}, \quad (8.20)$$

where $\theta = \phi + \pi/4$ and ϕ is a polar angle in the polar coordinate system.

Multiplying a vector describing the left handed circular polarization by this matrix, the following expression is derived:

$$\mathbf{E}_{AZI} = M_{QW} \frac{1}{\sqrt{2}} \begin{pmatrix} 1 \\ i \end{pmatrix} = \begin{pmatrix} -\sin \phi \\ \cos \phi \end{pmatrix} e^{i\phi} e^{i\frac{\pi}{4}}. \quad (8.21)$$

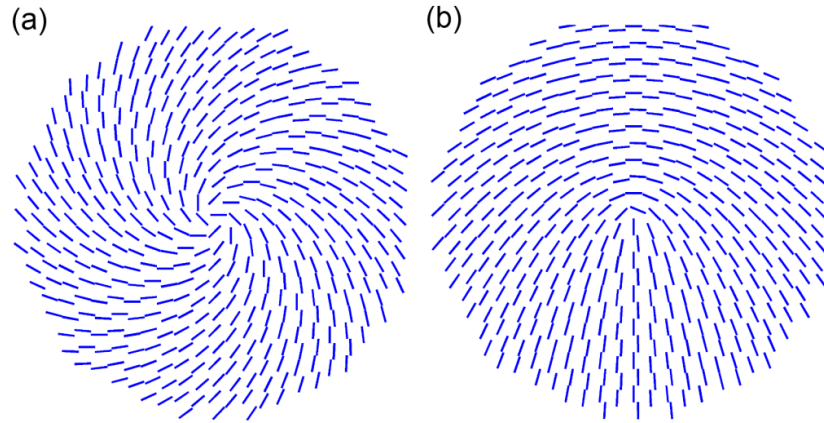


Figure 8.13: Schematic drawings of nanogratings distribution in quarter- (a) and half-wave (b) polarization converters. The blue dashes indicate the direction of the nanogratings.

The first term of the product represents azimuthal polarization while the second term indicates the presence of the orbital angular momentum $l = 1$. Similar calculations made for the right handed incident polarization yield radial polarization with the orbital momentum $l = -1$ (Figure 8.14). The appearance of the orbital momentum is the result of the Berry phase mentioned earlier. As a result, a combination of the radial/azimuthal polarization and orbital momentum yields a complicated electric field distribution. The pure radial polarization with flat phase front can be generated by a adding vortex phase plate, which would compensate the orbital momentum.

If the rotation operation is performed for a spatially homogeneous half-wave plate, we get the following Jones matrix expression for a spatially variant half-wave plate:

$$M_{HW} = \begin{pmatrix} \cos \phi & \sin \phi \\ \sin \phi & -\cos \phi \end{pmatrix}. \quad (8.22)$$

One can notice that this is essentially the same rotation operator, where the incident polarization is rotated by the angle ϕ . The only difference is that the angle used here is also the azimuth of the polar coordinates. Then for the incident horizontally polarized light, the radial polarization emerges:

$$\mathbf{E}_{RAD} = M_{HW} \cdot \mathbf{E}_{LVP} = M_{HW} \begin{pmatrix} 0 \\ 1 \end{pmatrix} = \begin{pmatrix} \sin \phi \\ -\cos \phi \end{pmatrix}. \quad (8.23)$$

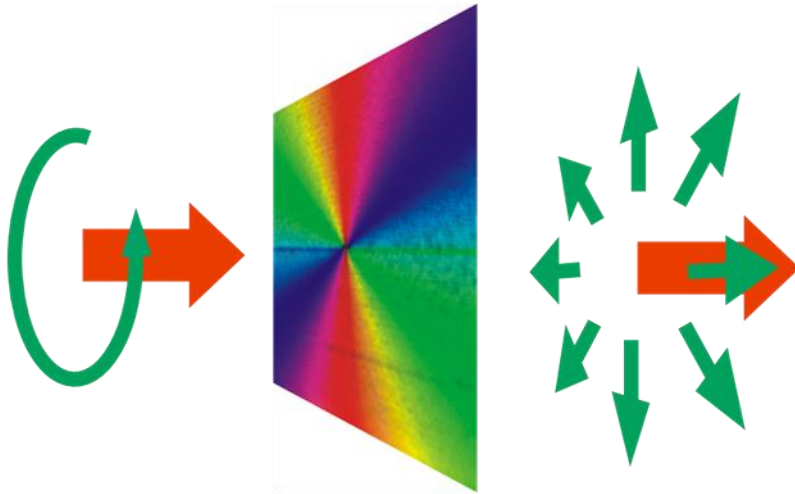


Figure 8.14: Principle of radial polarization converter (quarter-wave plate case). Incident circularly polarized light is converted into radially polarized optical vortex due to spatially variant slow axis direction shown in pseudo colour.

Similarly for the incident vertically polarized light, the azimuthal polarization is derived. In this case, as opposed to a spatially variant quarter-wave plate, a half-wave plate converts linear polarization into pure radial polarization state without the presence of orbital momentum. The superposition of two azimuthally symmetric polarization states can be easily produced by rotating the incident beam polarization with respect to the radially variant half-wave plate. An interesting result follows if a circularly polarized light is transmitted through the same converter:

$$\begin{aligned} \mathbf{E}_{VOR} &= M_{HW} \cdot \mathbf{E}_{RCP} = M_{HW} \frac{1}{\sqrt{2}} \begin{pmatrix} 1 \\ i \end{pmatrix} = \frac{1}{\sqrt{2}} \begin{pmatrix} \cos \phi + i \sin \phi \\ \sin \phi - i \cos \phi \end{pmatrix} \\ &= e^{i\phi} \begin{pmatrix} 1 \\ -i \end{pmatrix}. \end{aligned} \quad (8.24)$$

As one can see, incident circular polarization changes its handedness and additionally acquires a spatially variant phase factor which is a direct indication of an optical vortex presence. As a result, the same converter can be used for generation of azimuthally symmetric polarization states and optical vortices.

If a converter is designed for a 515 nm wavelength, the corresponding retardance values for quarter- and half-wave are 128.75 nm and 257.5 nm respectively. In order to reduce the fabrication time we performed a set of experiments searching for conditions where such retardance values could be induced by a single scan.

8.3.4 Fabrication and characterization

The main challenge in the fabrication of polarization converters is continuous control of the slow axis of the induced anisotropy. Several approaches were evaluated for this purpose. First, the converter was fabricated by raster scanning. The writing speed was very low as a result of the need to change polarization after every single dot. The fabricated structure also exhibited strong scattering due to its “pixelated” structure. However, the working principle was demonstrated, justifying the possibility to fabricate birefringent converters by ultrafast laser writing. In the next step, the birefringent converter was fabricated by writing multiple segments stacked together to form a uniform structure.

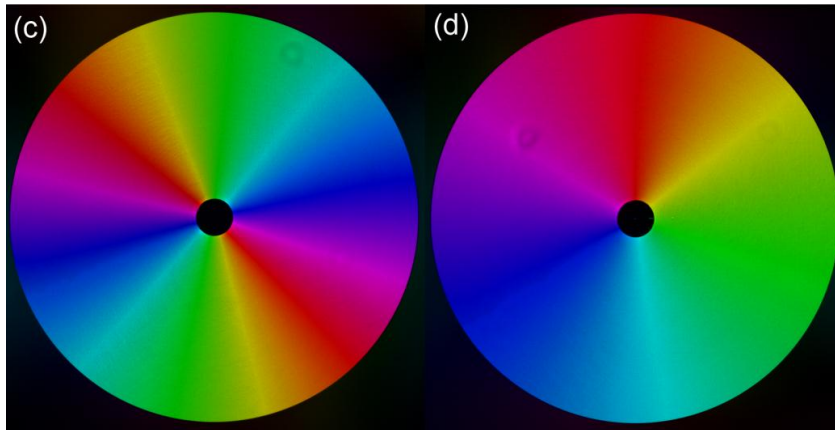


Figure 8.15: Quantitative birefringence measurements of femtosecond laser written radial polarization converters for circular (c) and linear (d) incident polarizations. The brightness represents the retardance magnitude while the colour indicates the direction of the slow axis.

Using this approach we substantially reduced the fabrication time and managed to improve the quality of the converter. However, an undesired diffraction pattern could be observed due to the radial arrangement of the segments. Finally, we managed to fully synchronise a rotation stage, responsible for slow axis orientation, with the translation stages and write the converter by moving a glass plate in a spiral trajectory while continuously rotating polarization of the laser beam. The optimized writing process appreciably reduced the total fabrication time, which in comparison to the initial results, was lowered by a factor of 7.

The average laser power and focusing optics for birefringent converter fabrication were chosen based on the results described in Chapter 7. To get the retardance value of a quarter-wave for 532 nm, the light was focused via an objective of $NA = 0.35$ as this requires less energy that means that the structures are more uniform. For the retardance value of a half-wave, the light was focused via an aspheric lens with $NA = 0.16$ and the writing speed was 2 mm/s (Figure 8.15).

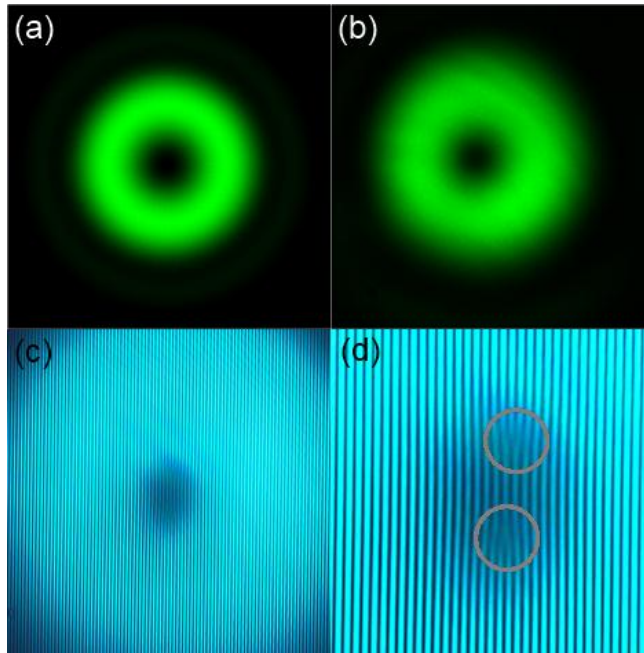


Figure 8.16: (a) Modelled and (b) measured vortex intensity profiles, (c) diffraction pattern of two interfering vortices, (d) zoomed central part, red circles indicate a 'fork' pattern formed due to a phase discontinuity present in the interfering electric field.

High quality polarization converters were also fabricated for 1030 nm and 1550 nm. As nanograting birefringence is constant for long wavelengths, the required retardance was achieved by stacking several birefringent layers together, while using the same focusing optics and laser power as for elements operating at 532 nm.

Operation of the fabricated devices was evaluated with several different laser sources: femtosecond Yb:KGW first and second harmonics, an argon ion CW laser (515 nm), a Nd:YAG CW laser (532 nm) and a telecom laser (1550 nm).

The ability of a half-wave retardance converter to generate an optical vortex with circular polarization was examined by observing the self-interference pattern on a CCD camera. The interference pattern was formed by overlapping two replicas of the laser beam after it passed through the converter. As both beams were incident at an angle, the intensity gained a 'sine' wave like modulation. In the interference pattern two forks can be clearly seen, confirming the presence of an optical vortex (Figure 8.16).

A constant value of retardance with the continuously varying direction of the slow axis was measured across the whole structure. The transmission losses are 40 % at 532 nm, 20 % at 1 micron and 10 % in the telecom wavelengths. The measurements made in the far-field were found to be in good agreement with the model of this optical system based on the Jones matrix formalism and Fourier propagation.

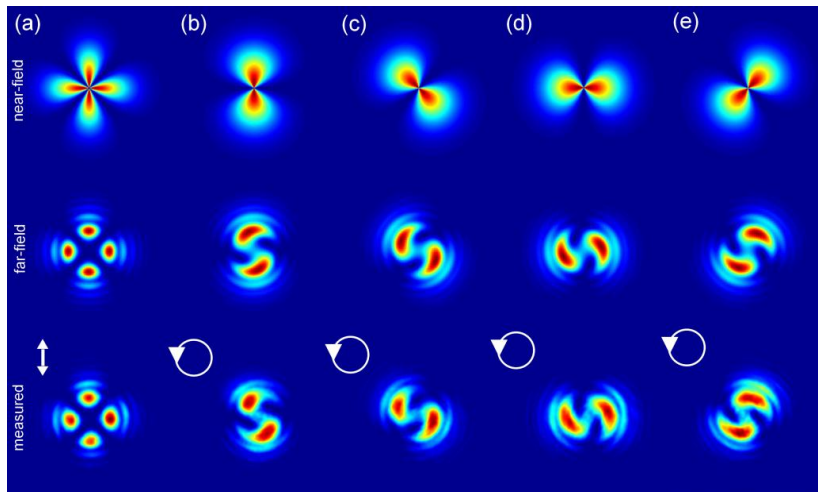


Figure 8.17: Modelled near- and far-field (top and middle) and measured (bottom) intensity distributions after the polarization converter for incident linear polarization (a) and for left handed circular polarization (i.e., azimuthal polarization with the orbital angular momentum $l = 1$ is generated) at different angles of the polarizer 0° (b), 45° (c), 90° (d), 135° (e). White arrows indicate the incident polarization state.

The performance of the converter for circular polarization was investigated with a circularly polarized argon ion laser beam ($\lambda = 514$ nm). After passing the quarter-wave retardance converter, the beam was transmitted through a linear polarizer and collected by a CCD camera. For comparison, the respective beam profiles were modelled using the Jones calculus and Fourier propagation (Figure 8.17). In the near-field, modelling and measurements produced the propeller shapes typical for the radial polarization. In the far-field, the diffraction distorts this shape producing a peculiar 's' shape pattern, though the symmetric propeller shape can be restored in the near-field by focusing the beam again.

An azimuthally (radially) polarized vortex with the orbital angular momentum $l = 1$ ($l = -1$) can be considered as a superposition of two circularly polarized

beams, one possessing the orbital angular momentum $l = 2$ ($l = -2$) and the other having a plane front. The interference of these two beams after the polarizer (analyser) produces a characteristic 's' shape pattern, which was observed in our experiment. To visually demonstrate this, we transmitted a radially polarized optical vortex generated with the converter through the polarization grating discussed above (Figure 8.18). As this grating works as a circular polarization beam splitter, the incident beam was split into an optical vortex and a plane wave.

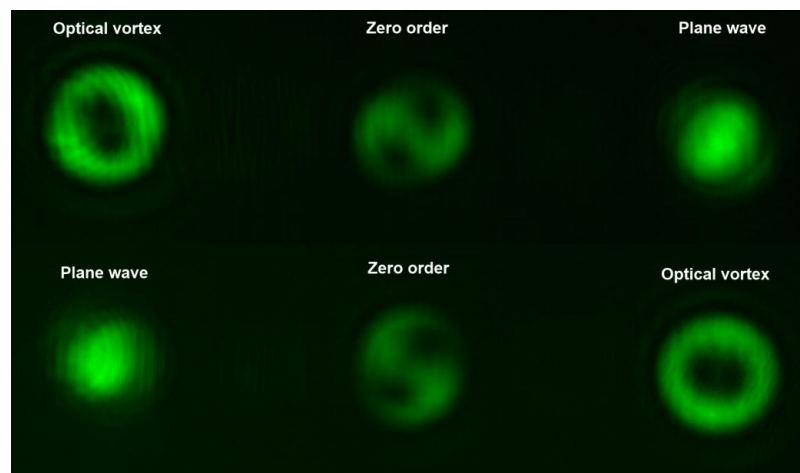


Figure 8.18: Diffraction patterns of radially/azimuthally polarized optical vortices.

A similar procedure was used for testing a half-wave retardance converter. If linear polarization is incident on such a converter a cylindrically symmetric polarization state is produced. In special cases one can produce radial or azimuthal polarization. In order to control the state of the output polarization the half-wave plate was before the converter. By aligning the dumbbell shape with the transmission axis of the linear polarizer placed after the converter we could adjust the system to get radial polarization. This is a pure radial polarization as opposed to the radially polarized optical vortex described above, thus the propeller shape is retained even in the far-field (Figure 8.19). The characteristic dumbbell shape measured after linear polarizer was almost symmetric for all orientations of polarizer's transmission axis (Figure 8.19).

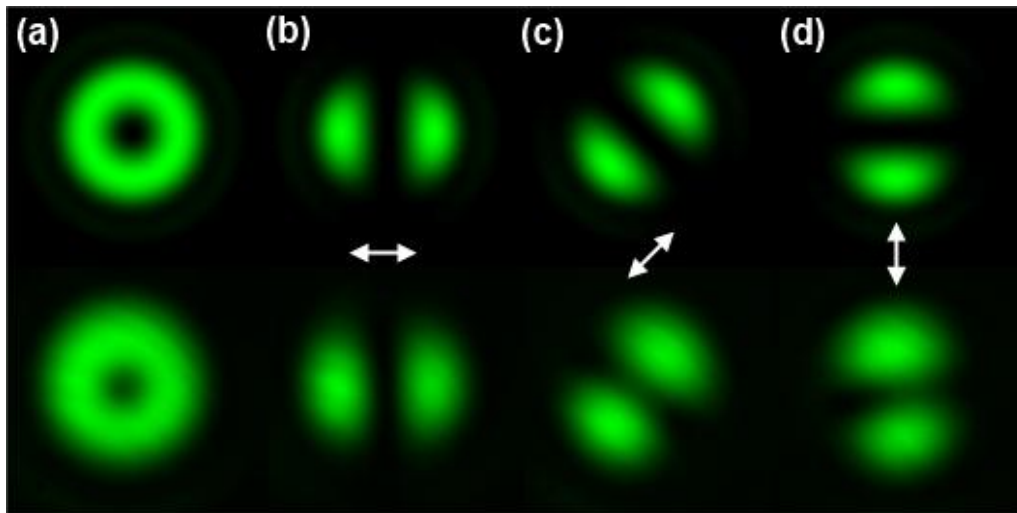


Figure 8.19: Modelled (top) and measured (bottom) profiles of generated radial polarization directly after converter (a) and after polarizer (b-d). White arrows indicate the transmission axis of the polarizer inserted between the converter and a CCD camera.

Additionally we investigated the contrast of the obtained beam (the ratio between minimum and maximum located in the central part and in the ring respectively), this parameter is of interest for many applications such as STED microscopy or atom trapping. Low contrast indicates the presence of a phase mismatch in the laser beam due to imperfections of the half-wave converter.

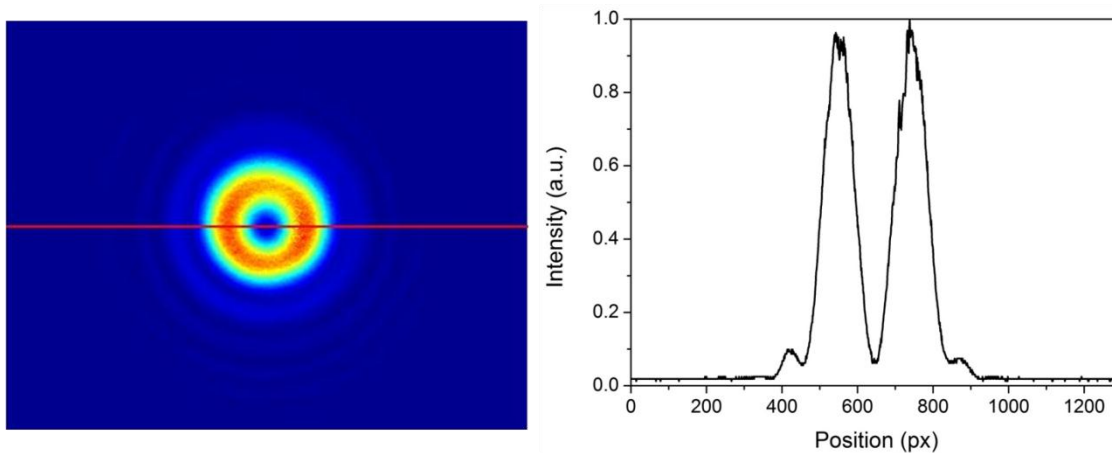


Figure 8.20: A beam profile of the radially polarized laser beam (515 nm) generated with a half-wave converter. The intensity distribution shown on the right is taken along the red line.

The circularly polarized optical vortex generated with a half-wave converter had a contrast of about 3%. However, we managed to improve it by more than one order

by inserting a linear polarizer after the converter. As a result, we measured that we are able to produce a high quality optical vortex with a contrast $>0.1\%$. The measurement of the exact value was limited by the dynamic range of the beam profiler used in the experiments (Figure 8.21).

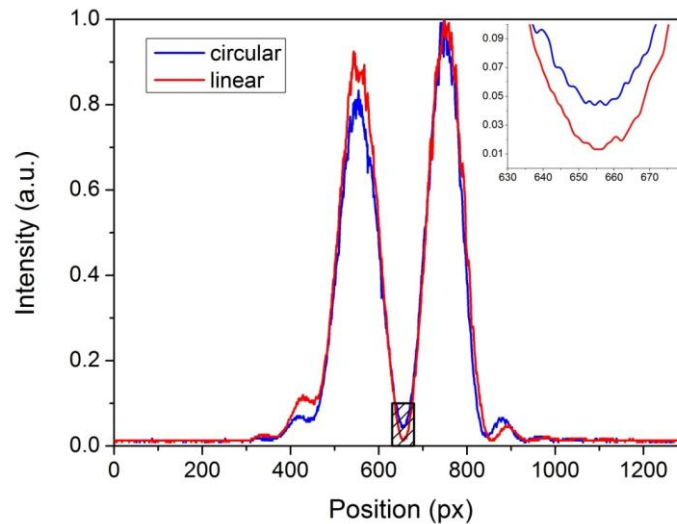


Figure 8.21: An optical vortex characterization with a beam profiler. After a linear polarizer the optical vortex intensity contrast is less than 0.1% (measurements are limited by the dynamic range of the camera). Inset: zoom of the vortex's central part. For a linearly polarized vortex, intensity measured in the central part is close to the background value ~ 0.01 .

The damage threshold for these converters was characterized by Altechna Ltd following the procedure according to ISO 11254 – 2 standard). Such an element had a damage threshold of 22.8 J/cm^2 at 1064 nm , $\tau = 3.5 \text{ ns}$, $f = 10 \text{ Hz}$.

8.3.5 Application of radial polarization for transparent material processing

In the introduction it was already mentioned that radial polarization leads to more efficient material processing. Currently, due to commercial interest only metals and semiconductors, i.e. absorbing materials were processed with radial polarization. We however aimed to investigate the effect of radially symmetric polarization on fused silica bulk modification. For a homogeneous polarization state (linear polarization) the nanogratings induced in fused silica are known to self-assemble from pulse to pulse arranging into highly organized nanostructures

covering large areas [52]. The radial polarization is known to induce concentric nanocircles if the irradiated sample is not translated [154]. Here we demonstrated that using a radially symmetric polarization state nanograting orientation depends on the writing direction. This observation can be exploited for efficient microfluidic device fabrication.

The experiments were performed with our femtosecond writing setup. The radially symmetric polarization state was generated by inserting a 6 mm diameter radial polarization converter described earlier in this chapter. In order to avoid phase distortion which might occur upon the reflection from dielectric mirrors and strongly distort a radially polarized beam profile, we placed the converter just before the objective lens. Using a three axial mechanical translation stage we aligned the converter with the optical axis of the laser beam by monitoring quality of the converted polarization. The state of the spatially variant polarization was controlled by the achromatic half-wave plate. The laser beam was finally focused with an 0.16 NA aspheric lens. The longitudinal field is not induced at such a low numerical aperture and the spatial polarization distribution after the converter is preserved also in the focus.

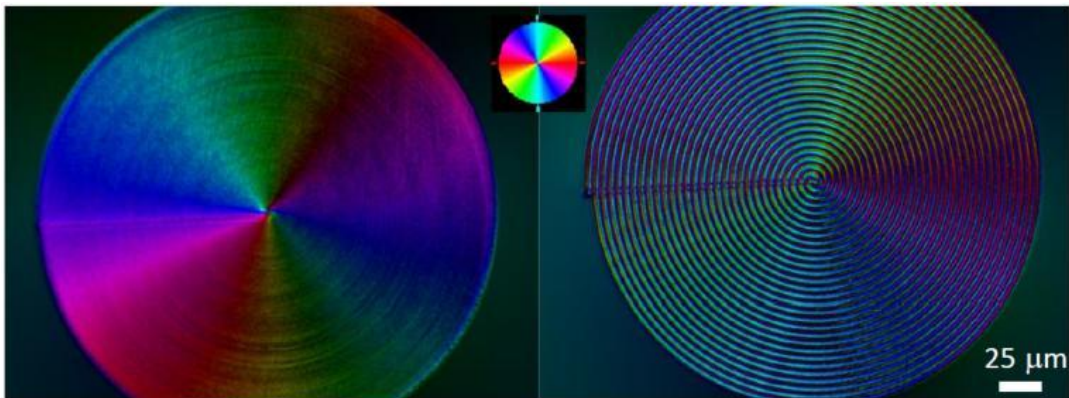


Figure 8.22: Birefringent structures written with a femtosecond radially polarized beam. Clear dependence of the slow axis orientation on writing direction can be seen. The uniform slow axis orientation can be achieved overlapping adjacent lines (Left), if the interline distance is increased each laser written line has a complex slow axis variation across.

In the first experiment we wrote spiral patterns with a radially polarized beam. Two structures with different inter-line separation ($1\ \mu\text{m}$ and $5\ \mu\text{m}$) were written

in the bulk of fused silica. No additional polarization control was included. The irradiated samples were further inspected with a quantitative birefringence measurement system Abrio (CRi Inc.). The slow axis of the induced birefringence clearly follows the direction of the laser beam scanning, indicating that nanogratings are spontaneously orienting with the scanning direction. If the inter-line distance is smaller than the spot size of the scanning laser beam a uniform radial distribution of the slow axis can be achieved. The self-orientation of the nanogratings is a result of their property that induced nanogratings record the last polarization state of the laser beam. Due to this phenomenon only the central part of the induced line will retain the nanograting orientation related to the writing direction. If the line separation is larger than the laser beam spot size the nanograting track has a slow axis which varies across the line.

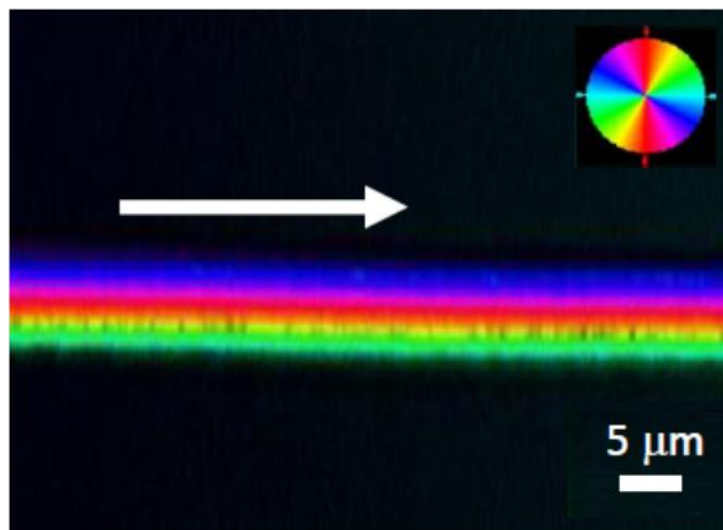


Figure 8.23: Abrio image of the line written with radially polarized femtosecond laser beam. White arrow indicates writing direction. The variation of the nanograting orientation manifests as spatial variation of slow axis direction.

8.4 5 dimensional optical memory

Another interesting application of femtosecond laser pulse induced birefringence is multi-dimensional optical memory. The information hunger fuels the race for continuous advances in data storage. Currently, mainly for this task, planar technologies are used (magnetic and optical hard disks) with simple multilayering added. Additionally, development of cloud technologies will also require the reliable storing of tremendous amounts of data in a single location. As a result, the

increasing storage capacity demands the development of new approaches, such as storing more than a single bit per one physical location of optical storage. Here we demonstrate a novel approach of multiplexing the data storage by femtosecond laser induced nanostructures.

8.4.1 Multi-dimensional optical memory

Optical data storage is based on the manipulation of optical properties in the storage medium. Typically, in such storages the reflectivity of the surface is manipulated to achieve a two level intensity signal system, e. g. CD, DVD and Blue-Ray. The data is recorded using the linear absorption of the material, thus only the surface can be modified in this case. This is so-called 2D optical memory, as the data is stored only on the surface of the carrying medium. Employing a nonlinear absorption mechanism, such as two photon absorption, 3D optical memory can be constructed [156], where optical properties of the medium can be manipulated in the confined volume and thus extending the possible storage capacity by at least 10 times. The theoretical capacity limit of 3D optical memory is about 3.5 Tbit/cm³. Still this optical recording technology is based on two level intensity signal encoding. Thus in a single memory cell or voxel only 1 bit can be stored. In order to further expand the potential storage capacity multiple research groups started investigating the possibility of storing more than one bit in a single voxel. This can be implemented in media which are sensitive not only to the intensity of the laser beam but also to its other properties. The signal can then be read in several channels, thus enabling multiplexing of the data. One of the most popular ways is to explore birefringent or dichroic properties of the materials, i.e. recording and reading the polarization of the light beam.

It is well known that elongated metallic nanoparticles exhibit strong dichroism. The ability to control the nanoparticle shape with ultrashort laser pulses was explored by several research groups. It was found that nanoparticles are elongated along the polarization direction of the writing beam polarization [157]. Additionally, glass embedded nanoparticles exhibit well confined resonances in their absorption spectrum the location of which directly depends on the size of the

particles. Combining these two properties researchers were able to record data in five dimensions [158] with a data capacity of 1 Tbit/cm³. Essentially, this memory storage is made by mixing golden nanoparticles of different sizes. Then each memory cell contains several nanoparticles, which exhibit different extinction spectrum and can be independently manipulated with several wavelengths. Here we aim to demonstrate 5D memory based solely on laser induced birefringence. Such a recording medium does not contain any substructure as opposed to the previously described multi-dimensional memory.

8.4.2 Optical storage based on nanograting

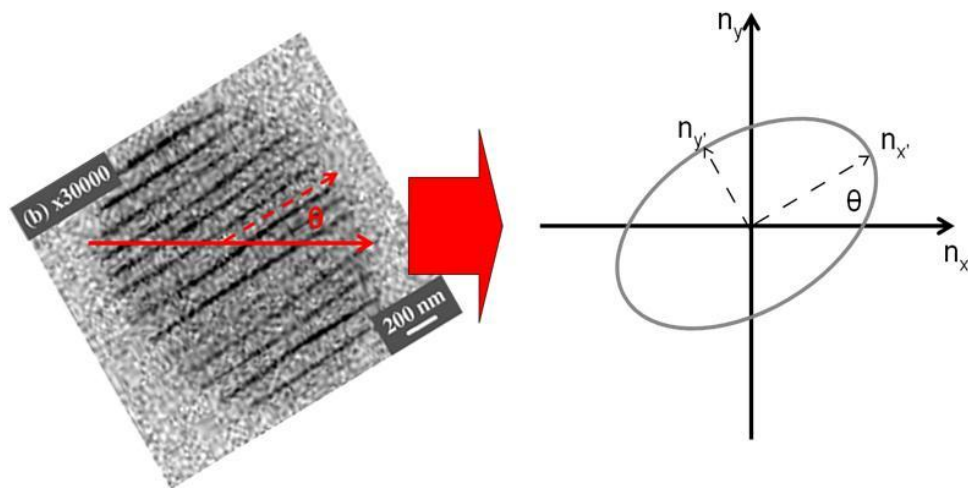


Figure 8.24: Schematic description of two parameters describing birefringence: slow axis angle θ and retardance $(n_{x'} - n_{y'}) \cdot d$.

More than a decade ago, the potential of ultrafast laser writing of isotropic modification for three-dimensional optical memory was demonstrated [44]. Later it was found that the ultrashort laser pulses could also induce anisotropic modifications related to self-assembled nanograting formation [52]. This anisotropy can be characterized by two independent parameters: retardance and slow axis orientation (Figure 8.24), which can be rewritten with successive pulse sequences [46,51]. Recently, it was proposed that using these two parameters optical recording can be extended beyond the three spatial dimensions [51]. As a result, femtosecond laser induced self-assembled nanostructures can be employed as a rewritable five-dimensional optical memory.

The femtosecond laser pulse induced nanograting is formed inside of fused silica glass, which itself is known for high stability and chemical resistance. Additionally, a nanograting is a structural modification which can withstand temperatures of 1000°C [49], making the described optical memory ideal for archiving high volumes of important information. It was also shown that such nanostructures can be successfully rewritten or deleted with ultrashort light pulses, which remodels an otherwise stable structure.

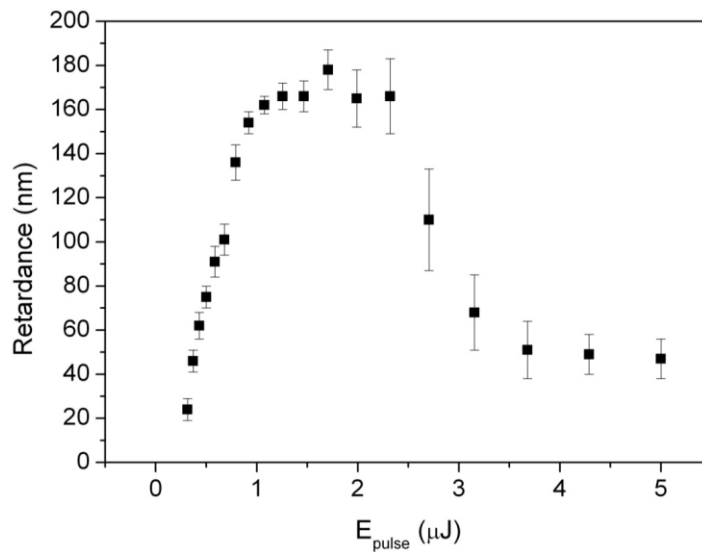


Figure 8.25: Dependence of femtosecond laser induced retardance on the pulse energy. In this experiment the laser repetition rate was set to 200 kHz. For pulse energies higher than 2 μJ strong damage occurs, which leads to reduction of induced retardance.

As the nanogratings are induced by non-linear absorption of intense femtosecond pulses, they are written selectively in the focal volume of the laser beam. The ability to record and read several layers of information by the nanogratings was demonstrated by Shimotsuma et al. [51]

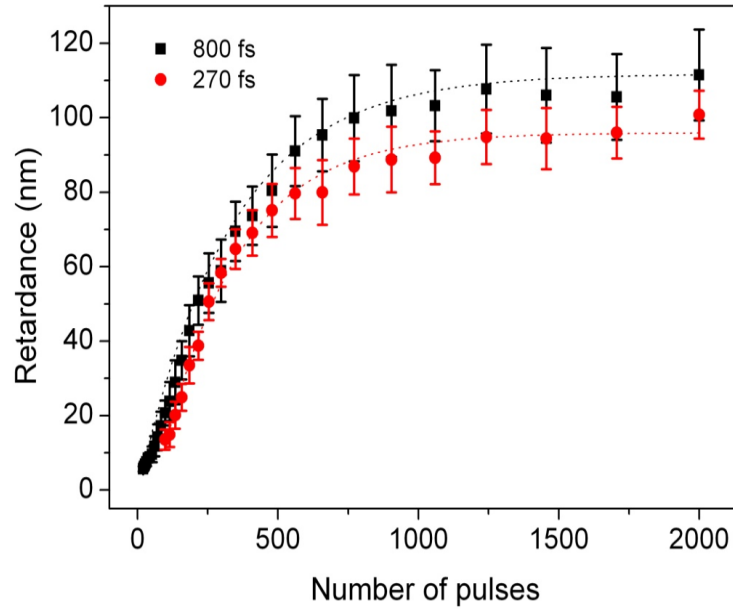


Figure 8.26: Dependence of femtosecond laser induced retardance on the number of pulses (or exposure time) for two different pulse durations (800 fs – black, 270 fs – red). In this experiment the laser repetition rate was set to 200 kHz.

During the recording procedure, the number of pulses and the azimuth of their polarization can independently control retardance and the slow axis direction. A set of experiments were performed to establish the relation of retardance with number of pulses (Figure 8.26). One can clearly see that retardance follows a square root law and is saturated with increasing number of pulses. By quantifying both parameters one can encode the information by using both parameters. The capacity of the storage will depend on the precision with which the retardance and slow axis can be written and read. Currently, during the recording procedure the retardance can be controlled with a precision of about 10 nm, while the slow axis angle can be defined with a precision of a few degrees. For the read-out procedure a polarization measurement system Abrio (CRi Inc.) is employed, which can measure both parameters with precision of less than 1 nm and 1 degree respectively.

For the demonstration of multi-dimensional optical recording a 0.35 NA aspheric lens was employed. The estimated spot size at the focus then is:

$$d = 2\omega_0 = \frac{2\lambda_0}{\pi NA} \sim 1800 \text{ nm.} \quad (8.25)$$

The depth of focus will be:

$$b = \frac{2\pi\omega_0^2}{\lambda_0} \sim 5000 \text{ nm.} \quad (8.26)$$

Assuming a 12 cm diameter and 1 mm thickness storage, the size of a standard optical disc, we can estimate that the storage capacity will be 70 GB for conventional 3D storage and 420 GB assuming 8 layers encoding for retardance and 8 layers for slow axis. These numbers demonstrate that even very moderate focusing leads to pretty impressive data capacities.



Figure 8.27: Images of 8 layers generated with MATLAB code for 5D optical recording demonstration. Each of these layers was assigned a fixed polarization orientation, while the greyscale information was recorded by variation of number of laser pulses.

The retardance can be read with about 10 nm precision, while slow axis can be resolved with 5 deg. For high NA retardance can be as high as 100 nm, while the slow axis angle can obviously vary from 0 to 180 deg. Thus we get 10 layers for retardance and 36 for slow axis. If we use irradiation parameters similar to that used for Blue-Ray discs (405 nm and 0.85 NA), we obtain 39 TB for 3D storage and 360 TB for 5D storage. Thus polarization multiplexing would improve storage capacity by one order.

In practice, multiple effects can significantly reduce (such as nonlinear absorption) or increase (spherical aberration, self-focusing) the size of an induced structure, thus complicating the evaluation of the recording resolution. In a very crude approximation the spot size estimated above can be considered as a size of laser induced structure. At high numerical apertures the spherical aberration will be extremely large. Liquid immersion lenses which are normally used to increase the NA and overcome the aberration will be impractical due to substantially lowering the recording speed. Another way of overcoming the spherical aberration would be adaptive optics implemented using liquid crystals or lenses with a variable focus.

As a demonstration of multidimensional optical data storage, we recorded the portraits of two great scientists, Maxwell and Newton, in a piece of silica glass by continuously controlling exposure and polarization during the writing process. For encoding both gray-scale (256 gray levels) portraits were first matched in pixel size. The Newton portrait was split into 8 layers and later combined with Maxwell image using a MATLAB code (Figure 8.27). Finally 8 gray-scale images were generated and each separately recorded with different polarization orientation.

The number of pulses can be easily set by our writing set-up controlling software provided by Altechna Ltd. We expressed grayscale values of each layer directly into the number of pulses. The polarization rotation is performed by mechanically rotating a half-wave plate. As a result, the Maxwell portrait was encoded with varying strength of birefringence and Newton's one by varying the slow-axis orientation. Later, using the Abrio system, we managed to decouple both images, clearly demonstrating the potential of the proposed information recording technique (Figure 8.28).

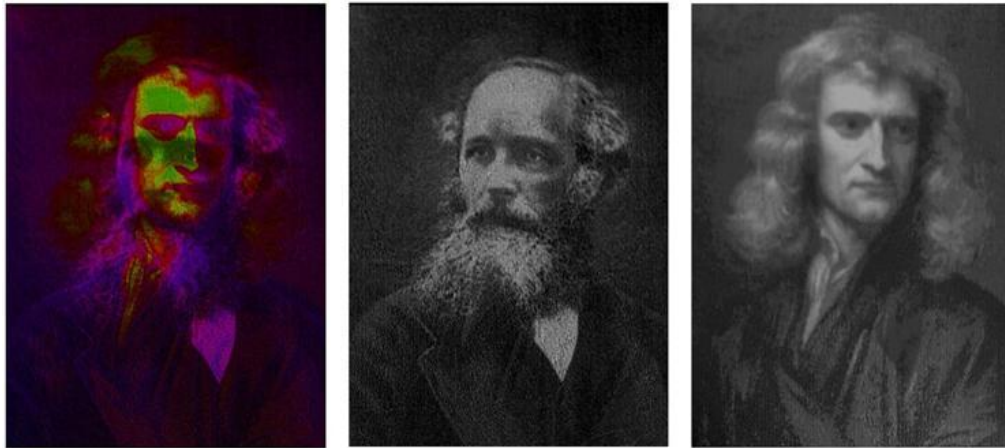


Figure 8.28: (Left) The Abrio image representing in false colours the recorded information in slow axis and retardance. (Middle and Right) Decoupled images of Maxwell and Newton (no additional operations on images were performed).

8.5 Conclusions

A femtosecond laser beam focused into the bulk of fused silica can produce self-organized nanograting. This structure, with sub-micron period, exhibits form birefringence with retardance of several hundreds nanometers. Manipulation of the writing laser beam polarization allows control of the spatial orientation of the nanostructure and as a result the orientation of the optical axes of induced birefringence. Here we demonstrate a technique which allows the fabrication of optical elements with spatially variant birefringence. The ability to control the direction of slow axis with a precision of one micron and induce high retardance levels leads to the engineering of unique optical devices.

A birefringent diffraction grating operating in the visible, with a diffraction efficiency of more than 80% was demonstrated. The birefringent grating exhibited sensitivity to the handedness of the circular polarization. Using a circularly polarized beam and this optical element one could measure the retardance of the material. It could operate with both monochromatic and polychromatic light sources. Such elements can be explored for instant (real time) polarization characterization or novel polarization microscopy.

Radial polarization beam converters were fabricated using the same femtosecond laser writing setup. The devices operating in the visible and near-infrared were

demonstrated. These elements allow the efficient conversion of linear polarization into radial/azimuthal polarization. Additionally, a circularly polarized beam can be converted into an optical vortex, where the charge sign is defined by the handedness of the incident circular polarization. This effect is similar to the one discussed in Chapter 5 and is also related to Pancharatnam–Berry geometrical phase. The quality of the converted beam is comparable to commercially available radial polarization generation techniques. The optimized fabrication procedure allowed the reduction of the writing time for a single converter down to one hour². High damage threshold allows applications of these converters where high power lasers are used.

Finally, we demonstrated the implementation of 5D optical recording based on femtosecond laser induced nanostructures in the bulk of fused silica. The additional channels for memory multiplexing were retardance and birefringence, which can be independently recorded and read. As a demonstration, two images were recorded into the same plane and then successfully decoupled using a quantitative birefringence measurement system. Potentially high capacity and stable optical storage could benefit for large storage infrastructures, where large amounts of information need to be stored in compact and reliable form.

² Fabrication time largely depends on the size of fabricated optical element. The quoted time is of the standard polarization converter of 4 mm in diameter.

Chapter 9. Conclusions and future work

9.1 Summary and discussion

In this thesis we have reported several novel developments in the field of femtosecond laser micro-structuring. Three optical vortex generation methods were demonstrated based on different approaches: second harmonic generation, edge birefringence and optical elements with spatially variant anisotropy. All three methods were implemented exploring the unique properties of femtosecond lasers: short pulse duration and high intensity. One common feature of all optical vortex generation methods described here is spin-to-orbital momentum conversion. We investigated two different transparent media: ambient air and glass. It is worth noticing, that all the presented work was done with a novel femtosecond laser source based on directly a diode pumped Yb:KGW crystal. The fact reflects recent advances in the field of short pulse lasers, which previously was dominated by Ti:Sapphire laser systems.

Using tightly focused femtosecond laser pulses into the ambient air we observed high average second harmonic generation. In contrast to previous experiments on second harmonic generation [66,70] we used tight laser focusing with a microscope objective. The high average power of our laser system allowed performing the experiment at a high repetition rate – 200 kHz. The effective second order nonlinearity in our experimental conditions was 0.03 pm/V, which is of the same order as in poled silica fibres [74,75]. A further efficiency increase could be achieved with specially designed capillary or photonic crystal fibre [76], can result in practical conversion efficiencies in excess of 50 %. Of course, a larger interaction length will require adding some sort of phase matching. Alternatively, the interaction length can be also increased by tightly focusing a Bessel beam instead of a Gaussian [78]. The Bessel beams possess a much longer Rayleigh range, thus effectively increasing the interaction length. The potential difficulty with Bessel beams is that a large part of the energy is present in the outer rings, as a result a larger power budget is required.

Tightly focusing femtosecond laser pulses into fused silica we observed the formation of a micro-bubble chain. The bubble size and distribution was controlled with the exposure time. We observed that with increasing number of laser pulses the bubble chain evolves into a single large bubble located at the top of the light induced structure. A high refractive index contrast present at the boundary of the micro-bubbles produced spatially variant edge birefringence. To our knowledge, this is the first observation of this type of birefringence in the femtosecond irradiated material. Spatially variant anisotropy was explored for spin-to-orbital momentum conversion. We demonstrated that femtosecond laser induced bubbles can act as radial polarizers and generate optical vortices and introduce orbital angular momentum to the propagating laser beam. The sign of the orbital momentum can be controlled by the handedness of the incident circular polarization. The experimental results were backed by a theoretical model based on Jones matrix calculus and Fourier propagation.

We also analysed the spectral properties of femtosecond laser induced nanostructures for a wide range of wavelengths from 200 nm to 1550 nm. The transmission spectrum of Type 2 modification had two pronounced absorption bands, which are attributed to E' and ODC(II) defects. In contrast, Type 1 modification only exhibited absorption band for E'. The main part of the optical losses was attributed to the scattering of the inhomogeneous structure. The spectral dependence of the retardance exhibited a sharp drop at the 450 nm and a large plateau extending to at least 1550 nm. At certain experimental conditions we managed to induce the refractive index increase with laser pulses longer than 300 fs. This contradicts previous results, which indicated that a positive refractive index change can be induced only with pulses shorter than 150 fs [45]. The obtained results were similar for the first and second harmonic of laser irradiation, indicating that nanograting formation is weakly dependent on the wavelength. In the optimized process we achieved a retardance of more than 200 nm in a single scan with relatively high writing speed (1 mm/s). We also measured an induced retardance dependence on the focusing depth. These measurements clearly demonstrated the importance of spherical aberration induced by a refractive index

mismatch. Due to the elongated focus produced by aberration, retardance induced deep in the sample was twice as large as close to the surface. Higher retardance values (such as half-wave for 1030 nm or 1550 nm) were reached by stacking several birefringent layers. As a result polarization sensitive devices can be implemented for various wavelengths in the visible and near infrared with losses as low as 10% (at 1550 nm).

Nonlinear interaction with transparent media enabled the fabrication of embedded optical elements. The ability to control the slow axis direction with a precision of one micron and induce high retardance levels lead to engineering optical devices capable of polarization sensitive diffraction and beam conversion. Firstly, we wrote a birefringent structure with a continuously modulated slow axis orientation. As a result, a birefringent diffraction grating operating in the visible with the diffraction efficiency of more than 80% was demonstrated. The sensitivity of such grating to the handedness of circular polarization was proposed for the characterization of birefringent samples. By measuring the ratio of two diffracted orders one can calculate the retardance of the sample. Secondly, we demonstrated high quality polarization converters which enabled the generation of cylindrical vector beams including radial and azimuthal polarizations and optical vortices. The converters were demonstrated for the visible and near infrared. Polarization converters were used for the experiments of femtosecond laser material processing. Finally, femtosecond laser induced nanogratings were explored for multi-dimensional optical recording. The data storage was multiplexed adding modulation of slow axis and retardance as additional memory cells. Potentially such optical storage could reach capacities of 360 TB. The high capacity and stability of demonstrated optical storage could be a benefit for large storage infrastructures, where large amounts of information need to be stored in a compact and reliable form.

Our major breakthroughs consisted of:

- Demonstration of high average second harmonic generation in air with tightly focused femtosecond laser pulses.

- Demonstration of optical vortex generation via second harmonic generation in air.
- Observation and characterization of optical vortices produced on femtosecond laser written micro-bubbles in the substrate of fused silica.
- First demonstration of a polarization diffraction grating operating in the visible and based on form birefringence.
- Demonstration of efficient radial polarization converters operating in the visible and near-infrared.
- Demonstration of 5D optical memory based on femtosecond laser induced nanostructures.

9.2 Future work

The work described in this thesis represents the advancement achieved in the field of femtosecond direct writing. However, current achievements also bring new challenges which need to be solved in the future.

The developed polarization converters can be seen as a demonstration of spatially birefringent element fabrication. Despite a comparably good performance of the demonstrated optical elements, the optimization of the process is required. One of the main problems is rather strong scattering, which introduces large losses in the visible. The magnitude of the birefringence can be controlled by fluence. However, additional parameters, such as a pulse duration, wavelength, can play important roles in the optical quality of the induced structure. Particularly, it is interesting to compare structures induced with laser pulses with duration ranging from tens to hundreds femtoseconds. The demonstrated optical elements are only a few of the possible applications of femtosecond laser induced nanostructures. Indeed, this technique has a potential for being used for the advanced polarization control and diffractive optics. A complex pattern can be easily implemented controlling polarization and retardance of the induced structure.

Currently, laser material processing is performed mostly with homogeneous (linear or circular) polarized Gaussian laser beams and is limited to the local modification of the refractive index of the material. However, recently a growing

interest has been expressed towards the application of more exotic laser beams such as Bessel or optical vortex for material processing. This can be generalized under the following idea: match the processing tool (i.e. laser) to the given task. For instance, Bessel beams allow fabrication of high aspect structures. However, every new type of laser beams requires specific optical elements (such as axicon for Bessel beam generation) and a cumbersome setup with very limited capabilities. As a result new types of laser beams are not widely used in industry. We foresee that the same technique which we explored for fabrication of polarization converters could be used to develop vast range of beam converters. The advantages of such elements are compactness, high damage threshold, efficiency and low cost. Preliminary results on fused silica laser modification with radial and azimuthal polarizations look promising and having a great potential for material processing.

Nanogratings could be explored not only for generation of known laser beams such as Bessel, Hermite-Gaussian, Laguerre-Gaussian modes, but also enable engineering of the intensity distribution at the focus of the beam. The development of the novel birefringent optical elements will expand knowledge on ultrafast laser beam focus control under tight focusing. For instance, radially polarized laser beam focused with high NA objective will exhibit a strong longitudinal electric field, which could even accelerate charged particles [146].

These possibilities of focal spot engineering can also bring benefits to nonlinear effects observed in ambient air. As it was discussed in Chapter 4 long interaction length should lead to more efficient second harmonic generation. This could be achieved with Bessel beams. Another interesting experiment would be with laser beams carrying an angular momentum (circularly polarized laser beams or optical vortices). Finally, the nonlinear interaction could be controlled via temporal shape of incoming pulse. The temporal shaping will allow optimising plasma excitation and a subsequent nonlinear interaction with a trailing part of the pulse.

Currently, intrinsic parameters (period and pitch) of femtosecond laser induced self-assembled nanogratings are not controlled. The ability to manipulate them

would open new possibilities for engineering optical properties of the material. The dispersion control could be achieved via the nanogratings period. As a result, we will be able to develop devices operating in a broad spectrum range, which is very important for extremely short few cycle pulses, widely used in attosecond pulse generation. Also this will allow us to locally control the phase and polarization of the light thus effectively replacing costly equipment such as spatial light modulators used for similar purposes today.

It is known that this period depends on fluence and wavelength. The few cycle pulses could provide access to multiple wavelengths spanned over a large part of the visible spectrum. As a result, the achromatic elements could be fabricated if the aspect ratio and the period could be easily adjusted during the experiment. The manipulation of a few cycle pulses is extremely difficult. First, extremely short pulses require complicated pulse compression schemes. Second, their broad spectrum complicates focusing as chromatic aberrations can be easily introduced. Third, interaction of material with such short pulses could be affected by strong spatio-temporal distortions. Thus pulses of a few femtoseconds are not yet explored for material processing.

The ability to induce high retardance of up to several microns would allow the fabrication of birefringent elements for the telecom band and the far-infrared. The losses should be minimal for these wavelengths. However, current fabrication time is too long for practical applications. The fabrication time could be reduced using a multifoci pattern created with a microlens array or a spatial light modulator. Currently, we are modifying our femtosecond laser setup to introduce a liquid crystal spatial light modulator, which will allow the advanced control of light distribution at the focus.

The self-assembly mechanism responsible for nanogratings is still under discussion. All proposed theories are supported only by post mortem measurements. More efforts should be made to investigate the temporal evolution of nanogratings formation. However, this will require an experimental technique with high spatial and temporal resolution.

List of Publications

Journal Papers

M.Beresna, P.G.Kazansky, Y.Svirko, M.Barkauskas, R.Danielius

High average power second harmonic generation in air

Applied Physics Letters 2009 Vol.95 pp.121502

M.Beresna, P.G.Kazansky

Polarization diffraction grating produced by femtosecond laser nanostructuring in glass

Optics Letters 2010 Vol.35(10) pp.1662-1664

M.Beresna, P.G.Kazansky, O.Deparis, I.C.S.Carvalho, S.Takahoshi, A.V.Zayats

Poling-assisted fabrication of plasmonic nanocomposite devices in glass

Advanced Materials 2010 Vol.22(39) pp.4368-4372

Y.Shimotsuma, M.Sakakura, P.G.Kazansky, M.Beresna, J.Qiu, K.Miura, K.Hirao

Ultrafast manipulation of self-assembled form birefringence in glass

Advanced materials 2010 Vol.22(36) pp.4039-4043

C.Corbari, M.Beresna, P.Kazansky

Saturation of absorption in noble metal doped nanocomposite glass film excited by evanescent light field

Applied Physics Letters 2010 Vol.97 pp.261101

M.Beresna, M.Gecevicius, P.G.Kazansky, T.Gertus

Radially polarized optical vortex converter created by femtosecond laser nanostructuring of glass

Applied Physics Letters 2011 Vol.98(20) pp.201101

O.Deparis, M.Beresna, C.Vandenbem, P.G.Kazansky

Light coupling and enhanced backscattering in layered plasmonic nanocomposites

Optics Express 2011 Vol.19(2) pp.1335-1343

M.Beresna, M.Gecevicius, P.G.Kazansky

Polarization sensitive elements fabricated by femtosecond laser nanostructuring of glass
Optical Materials Express 2011 Vol.1(4) pp.783-795 (Invited)

M.Lancry, B.Poumellec, A.Chahid-Erraji, M.Beresna, P.G.Kazansky

Dependence of the femtosecond laser refractive index change thresholds on the chemical composition of doped-silica glasses

Optical Materials Express 2011 Vol.1(4) pp.711-723

M.Beresna, M.Gecevicius, N.M.Bulgakova, P.G.Kazansky

Twisting light with micro-spheres produced by ultrashort light pulses

Optics Express 2011 Vol.19(20) pp.18989-18996

P.G.Kazansky, Y.Shimotsuma, M.Sakakura, M.Beresna, M.Gecevicius, Y.Svirko, S.Akturk, J.Qiu, K.Miura, K.Hirao

Photosensitivity control of an isotropic medium through polarization of light pulses with tilted intensity front

Optics Express 2011 Vol.19(21) pp.20657-20664

Conference Papers and Invited Talks

M.Beresna, I.Carvalho, O.Deparis, A.V.Zayats, C.Corbari, P.G.Kazansky

Sensing properties of golden nanoparticles embedded in sol-gel

COST Action MP0702 Training School Metz France 23-25 Mar 2009

P.G.Kazansky, W.Yang, M.Beresna, Y.Shimotsuma, M.Sakakura, K.Miura, K.Hirao, J.Qiu, Y.P.Svirko

3D nanoripples, self-assembled form birefringence and ultrafast laser calligraphy in transparent materials

Workshop on ZnO and TiO2 Nanostructures Berlin 9 Jul 2009 (Invited)

P.G.Kazansky, Y.Shimotsuma, J.Qiu, W.Yang, M.Sakakura, M.Beresna, Y.Svirko, S.Aktürk, K.Hirao

Ultrafast light blade: Anisotropic sensitivity of isotropic medium to femtosecond laser radiation

Advanced Laser Technologies Antalia 26 Sep - 1 Oct 2009 (Invited)

P.G.Kazansky, W.Yang, C.Corbari, M.Beresna, Y.Shimotsuma, M.Sakakura, K.Miura, K.Hirao, J.Qiu, Y.P.Svirko

Recent advances in ultrafast laser micromachining of transparent materials

Lasers in Manufacturing, The 19th International Congress on Photonics in Europe Munich 15-18 Jun 2009 (Invited)

P.G.Kazansky, M.Beresna, C.Corbari, A.Canagasabey, M.Ibsen, Y.Shimotsuma, M.Sakakura, K.Miura, K.Hirao, J.Qiu

Recent advances in material modification by strong fields: from poling to femtosecond laser writing

CLEO Pacific Rim Shanghai 30 Aug - 3 Sep 2009 (Invited)

P.G.Kazansky, M.Beresna, Y.Shimotsuma, K.Hirao, Y.P.Svirko

The art and science of femtosecond laser writing

The 22nd Annual Meeting of the IEEE Photonics Society Belek-Antalia 4-8 Oct 2009 (Invited)

P.G.Kazansky, W.Yang, M.Beresna, Y.Shimotsuma, M.Sakakura, K.Hirao, J.Qiu, Y.P.Svirko

New phenomena in ultrafast laser interaction with matter

Progress In Electromagnetics Research Symposium Beijing 23-27 Mar 2009

P.G.Kazansky, M.Beresna, Y.Shimotsuma, M.Sakakura, K.Miura, K.Hirao, J.Qiu, Y.P.Svirko

Recent advances in ultrafast laser micromachining: From optical materials to living cells

Photonic Tools in Biology: Marker-free Imaging and Optical Manipulation Institute of Physics, London 7 Dec 2009

M.Beresna, P.G.Kazansky

Beam shaping with birefringent structures written in silica glass

Northern Optics 2009 Vilnius Lithuania 26-28 Aug 2009

P.G.Kazansky, M.Beresna, Y.Shimotsuma, K.Hirao, Y.P.Svirko

New phenomena in interaction of intense ultrashort light pulses with transparent materials: from 3D self-assembled nanostructures to quill writing and nonreciprocal photosensitivity

Photonics West 2010 San Francisco 23-28 Jan 2010 (Invited)

M.Beresna, P.G.Kazansky

Recent advances in femtosecond laser direct writing of integrated optical elements

WE-Heraeus Seminar on Quantum Communications Based on Integrated Optics Bad Honnef

22-25 Mar 2010

P.G.Kazansky, Y.Shimotsuma, M.Beresna, M.Sakakura, J.Qiu, S.Aktürk, Y.Svirko, K.Miura, K.Hirao

Material processing using ultrashort light pulses with tilted front

CLEO/QELS 2010 San Jose 16-21 May 2010

M.Beresna, P.G.Kazansky

Polarization diffraction grating produced by femtosecond laser nanostructuring in glass

CLEO/QELS 2010 San Jose 16-21 May 2010

M.Beresna, P.G.Kazansky, Y.Svirko, M.Barkauskas, R.Danielius

Second harmonic optical vortex generation in air

CLEO/QELS 2010 San Jose 16-21 May 2010

M.Beresna, P.G.Kazansky

Femtosecond laser induced vortex anisotropy

CLEO/QELS 2010 San Jose 16-21 May 2010

P.G.Kazansky, M.Beresna, Y.Shimotsuma, K.Hirao, Y.P.Svirko

New phenomena in interaction of intense ultrashort light pulses with transparent materials: from 3D self-assembled nanostructures to quill writing and nonreciprocal photosensitivity

Proc. SPIE 2010 Vol.7600 pp.760017

P.G.Kazansky, M.Beresna, Y.Shimotsuma, K.Hirao, Y.P.Svirko, S.Aktürk

Revealing new properties of light-matter interaction using ultrashort light pulses: from self-assembled nanostructures to hidden anisotropy of light beam

International Symposium on Filamentation Crete 31 May-5 Jun 2010 (Invited)

P.G.Kazansky, M.Beresna, Y.Shimotsuma, M.Sakakura, Y.Svirko, S.Aktürk, J.Qiu, K.Miura, K.Hirao

Revealing extraordinary properties of femtosecond laser writing in glass

ISNOG 2010 Ningbo 13-18 Jun 2010 (Invited)

P.G.Kazansky, M.Beresna, Y.Shimotsuma, K.Hirao, Y.P.Svirko, S.Aktürk

Avant-garde femtosecond laser writing

BGPP 2010 Karlsruhe 21-24 Jun 2010 BWB1 (Invited)

C.Corbari, M.Beresna, O.Deparis, P.G.Kazansky

Leaky-modes excitation in thermally poled nanocomposite glass and their exploitation for saturable absorption

BGPP 2010 Karlsruhe 21-24 June 2010 BTuB7

O.Deparis, M.Beresna, C.Corbari, P.G.Kazansky

Enhanced light backscattering in thermally poled plasmonic nanocomposite and its application to vapour sensing

BGPP 2010 Karlsruhe 21-24 Jun 2010 BThD4 (Postdeadline)

P.G.Kazansky, M.Beresna, Y.Shimotsuma, K.Hirao

Recent advances in ultrafast laser processing of transparent materials

ICONO/LAT 2010 Kazan Russia 23-27 Aug 2010 (Invited)

P.G.Kazansky, M.Beresna, Y.Shimotsuma, M.Sakakura, J.Qiu, Y.P.Svirko, S.Aktürk, K.Miura, K.Hirao, C.Corbari

Recent advances in femtosecond laser writing inside transparent materials

Advanced Laser Technologies (ALT 2010) Nijmegen, Netherlands 12-16 Sep 2010 (Invited)

P.G.Kazansky, M.Beresna, Y.Shimotsuma, K.Hirao, Y.P.Svirko, S.Aktürk

The science and art of femtosecond laser writing

Alexander von Humboldt Forum 'Science and Society in Modern Europe' Vilnius 23-26 Sep 2010 (Invited)

P.G.Kazansky, M.Beresna, C.Corbari, Y.Shimotsuma, M.Sakakura, K.Miura, J.Qiu

Extraordinary modifications and structures in glass produced by ultrafast laser writing

International Congress on Ceramics Osaka 14-18 Nov 2010 (Invited)

M.Beresna, M.Gecevicius, P.G.Kazansky

Light twisting with micro-spheres produced by ultrashort light pulses

Open Readings 2011 Vilnius, Lithuania 17-19 Mar 2011

M.Gecevicius, M.Beresna, P.G.Kazansky

Exploring 5th dimension of optical recording with ultrashort light pulses

CLEO/QELS 2011 Baltimore 1-6 May 2011

M.Beresna, P.G.Kazansky, T.Taylor, A.V.Kavokin

Freezing ultrashort light pulses by exciton-polariton interference in glass

CLEO/QELS 2011 Baltimore 1-6 May 2011

M.Beresna, M.Gecevicius, P.G.Kazansky

Polarization vortex converter imprinted by femtosecond laser nanostructuring in glass

CLEO/QELS 2011 Baltimore 1-6 May 2011

P.Kazansky, M.Beresna, Y.Bellouard

Beyond conventional 3D ultrafast laser material processing

CLEO Europe Munich 22-26 May 2011 CM2.2 (Invited)

P.G.Kazansky, M.Beresna, M.Gecevicius

Harnessing ultrafast laser induced nanostructures in transparent materials

Workshop on Nonlinear nanostructures for ultrafast laser applications Berlin May 19-20 2011

(Invited)

A.Champion, Y.Belouard, M.Gecevicius, M.Beresna, P.G.Kazansky

Role of stress in the chemical etching of fused silica exposed to low-energy femtosecond laser pulses

Frontiers in Ultrafast Optics, Biomedical, Scientific and Industrial Applications San Francisco
23-26 Jan 2011 SPIE 7925 pp.79250Z

**P.Kazansky, M.Beresna, Y.Shimotsuna, M.Gecevicius, M.Sakakura, C.Corbari, K.Miura,
K.Hirao, Y.Bellouard**

Phase transitions induced by ultrafast laser writing in transparent materials

CLEO/QELS 2011 Baltimore 1-6 May 2011

M.Beresna, M.Gecevicius, P.G.Kazansky

Discovering new properties and applications of ultrafast laser nanostructuring in transparent materials

Bibliography

1. D. E. Spence, P. N. Kean, and W. Sibbett, "60-fsec pulse generation from a self-mode-locked Ti:sapphire laser," *Optics Letters* **16**, 42 (1991).
2. U. Keller, D. A. B. Miller, G. D. Boyd, T. H. Chiu, J. F. Ferguson, and M. T. Asom, "Solid-state low-loss intracavity saturable absorber for Nd:YLF lasers: an antiresonant semiconductor Fabry–Perot saturable absorber," *Optics Letters* **17**, 505 (1992).
3. D. Du, X. Liu, G. Korn, J. Squier, and G. Mourou, "Laser-induced breakdown by impact ionization in SiO₂ with pulse widths from 7 ns to 150 fs," *Applied Physics Letters* **64**, 3071 (1994).
4. P. P. Pronko, S. K. Dutta, J. Squier, J. V. Rudd, D. Du, and G. Mourou, "Machining of sub-micron holes using a femtosecond laser at 800 nm," *Optics Communications* **114**, 106–110 (1995).
5. K. M. Davis, K. Miura, N. Sugimoto, and K. Hirao, "Writing waveguides in glass with a femtosecond laser," *Optics Letters* **21**, 1729 (1996).
6. Y. Shimotsuma, P. Kazansky, J. Qiu, and K. Hirao, "Self-Organized Nanogratings in Glass Irradiated by Ultrashort Light Pulses," *Physical Review Letters* **91**, 247405 (2003).
7. Y. Sikorski, A. Said, P. Bado, R. Maynard, C. Florea, and K. Winick, "Optical waveguide amplifier in Nd-doped glass written with near-IR femtosecond laser pulses," *Electronics Letters* **36**, 226–227 (2000).
8. R. Osellame, S. Taccheo, and G. Cerullo, "Optical gain in Er-Yb doped waveguides fabricated by femtosecond laser pulses," *Electronics letters* **38**, 964–965 (2002).
9. A. G. Okhrimchuk, A. V. Shestakov, I. Khrushchev, and J. Mitchell, "Depressed cladding, buried waveguide laser formed in a YAG:Nd³⁺ crystal by femtosecond laser writing.," *Optics letters* **30**, 2248–50 (2005).
10. S. Maruo, O. Nakamura, and S. Kawata, "Three-dimensional microfabrication with two-photon-absorbed photopolymerization.," *Optics letters* **22**, 132–4 (1997).

11. S. Maruo and J. T. Fourkas, "Recent progress in multiphoton microfabrication," *Laser & Photonics Review* **2**, 100–111 (2008).
12. K. König, I. Riemann, P. Fischer, and K. J. Halhuber, "Intracellular nanosurgery with near infrared femtosecond laser pulses.," *Cellular and molecular biology (Noisy-le-Grand, France)* **45**, 195–201 (1999).
13. M. F. Yanik, H. H. N. Cinar, A. D. Chisholm, Y. Jin, and A. Ben-Yakar, "Neurosurgery: functional regeneration after laser axotomy.," *Nature* **432**, 822 (2004).
14. P. G. Kazansky, W. Yang, E. Bricchi, J. Bovatsek, A. Arai, Y. Shimotsuma, K. Miura, and K. Hirao, "'Quill' writing with ultrashort light pulses in transparent materials," *Applied Physics Letters* **90**, 151120 (2007).
15. D. N. Vitek, E. Block, Y. Bellouard, D. E. Adams, S. Backus, D. Kleinfeld, C. G. Durfee, and J. A. Squier, "Spatio-temporally focused femtosecond laser pulses for nonreciprocal writing in optically transparent materials," *Optics Express* **18**, 24673–24678 (2010).
16. P. G. Kazansky, Y. Shimotsuma, M. Sakakura, M. Beresna, M. Gecevičius, Y. Svirko, S. Akturk, J. Qiu, K. Miura, and K. Hirao, "Photosensitivity control of an isotropic medium through polarization of light pulses with tilted intensity front," *Optics Express* **19**, 20657 (2011).
17. W. Yang, P. G. Kazansky, and Y. P. Svirko, "Non-reciprocal ultrafast laser writing," *Nature Photonics* **2**, 99–104 (2008).
18. Y. Y. Lau, F. He, D. P. Umstadter, and R. Kowalczyk, "Nonlinear Thomson scattering: A tutorial," *Physics of Plasmas* **10**, 2155 (2003).
19. C. D'Amico, A. Houard, M. Franco, B. Prade, A. Mysyrowicz, A. Couairon, and V. Tikhonchuk, "Conical Forward THz Emission from Femtosecond-Laser-Beam Filamentation in Air," *Physical Review Letters* **98**, (2007).
20. R. Ackermann, K. Stelmaszczyk, P. Rohwetter, G. Méjean, E. Salmon, J. Yu, J. Kasparian, G. Méchain, V. Bergmann, S. Schaper, B. Weise, T. Kumm, K. Rethmeier, W. Kalkner, L. Wöste, and J. P. Wolf, "Triggering and guiding of megavolt discharges

- by laser-induced filaments under rain conditions," *Applied Physics Letters* **85**, 5781 (2004).
21. U. Morgner, F. X. Kärtner, S. H. Cho, Y. Chen, H. a Haus, J. G. Fujimoto, E. P. Ippen, V. Scheuer, G. Angelow, and T. Tschudi, "Sub-two-cycle pulses from a Kerr-lens mode-locked Ti:sapphire laser: addenda.," *Optics letters* **24**, 920 (1999).
 22. L. Giniunas, J. Pocius, and R. Danielius, "Versatile high power, high repetition rate Yb femtosecond system," *2007 European Conference on Lasers and Electro-Optics and the International Quantum Electronics Conference* **2721**, 1–1 (2007).
 23. U. Keller, "Ultrafast solid-state laser oscillators: a success story for the last 20 years with no end in sight," *Applied Physics B* **100**, 15–28 (2010).
 24. D. Strickland and G. Mourou, "Compression of amplified chirped optical pulses," *Optics Communications* **55**, 447–449 (1985).
 25. S. Backus, C. G. Durfee, M. M. Murnane, and H. C. Kapteyn, "High power ultrafast lasers," *Review of Scientific Instruments* **69**, 1207 (1998).
 26. L. Allen, M. Beijersbergen, R. Spreeuw, J. Woerdman, and others, "Orbital angular momentum of light and the transformation of Laguerre-Gaussian laser modes," *Physical Review A* **45**, 8185–8189 (1992).
 27. M. Fox, *Optical Properties of Solids*, 2nd ed. (Oxford University Press, 2010), p. 396.
 28. L. Sudrie, A. Couairon, M. Franco, B. Lamouroux, B. Prade, S. Tzortzakis, and A. Mysyrowicz, "Femtosecond Laser-Induced Damage and Filamentary Propagation in Fused Silica," *Physical Review Letters* **89**, 186601 (2002).
 29. M. J. Soileau, N. Mansour, E. W. van Stryland, and W. E. Williams, "Laser-induced damage and the role of self-focusing," *Optical Engineering* **28**, 1133–1144 (1989).
 30. D. Rayner, a Naumov, and P. Corkum, "Ultrashort pulse non-linear optical absorption in transparent media.," *Optics express* **13**, 3208–17 (2005).
 31. A. Marcinkevičius, V. Mizeikis, S. Juodkasis, S. Matsuo, and H. Misawa, "Effect of refractive index-mismatch on laser microfabrication in silica glass," *Applied Physics A: Materials Science & Processing* **76**, 257–260 (2003).

32. R. R. R. Gattass and E. Mazur, "Femtosecond laser micromachining in transparent materials," *Nature Photonics* **2**, 219–225 (2008).
33. C. B. Schaffer, A. Brodeur, and E. Mazur, "Laser-induced breakdown and damage in bulk transparent materials induced by tightly focused femtosecond laser pulses," *Measurement Science and Technology* **12**, 1784–1794 (2001).
34. L. V. Keldysh, "Ionization in the field of a strong electromagnetic wave," *Sov. Phys. JEPT* **20**, 1307–1314 (1965).
35. H. Misawa and S. Juodkakis, eds., *3D Laser Microfabrication. Principles and Applications* (Wiley-VCH, 2006).
36. M. D. Perry, B. C. Stuart, P. S. Banks, M. D. Feit, V. Yanovsky, and a. M. Rubenchik, "Ultrashort-pulse laser machining of dielectric materials," *Journal of Applied Physics* **85**, 6803 (1999).
37. D. G. Papazoglou, I. Zergioti, and S. Tzortzakis, "Plasma strings from ultraviolet laser filaments drive permanent structural modifications in fused silica.," *Optics letters* **32**, 2055–7 (2007).
38. L. Bressel, D. de Ligny, C. Sonnevile, V. Martinez, V. Mizeikis, R. Buividas, and S. Juodkakis, "Femtosecond laser induced density changes in GeO₂ and SiO₂ glasses: fictive temperature effect [Invited]," *Optical Materials Express* **1**, 605 (2011).
39. S. S. Mao, F. Quere, S. Guizard, X. Mao, R. E. Russo, G. Petite, and P. Martin, "Dynamics of femtosecond laser interactions with dielectrics," *Applied Physics A* **79**, 1695–1709 (2004).
40. E. N. Glezer and E. Mazur, "Ultrafast-laser driven micro-explosions in transparent materials," *Applied Physics Letters* **71**, 882 (1997).
41. J. W. Chan, T. Huser, S. Risbud, and D. M. Krol, "Structural changes in fused silica after exposure to focused femtosecond laser pulses.," *Optics letters* **26**, 1726–8 (2001).
42. H. Sun, S. Juodkakis, and M. Watanabe, "Generation and recombination of defects in vitreous silica induced by irradiation with a near-infrared femtosecond laser," *The Journal of Physical Chemistry. B* 3450–3455 (2000).

43. D. Grojo, M. Gertsvolf, S. Lei, T. Barillot, D. Rayner, and P. Corkum, "Exciton-seeded multiphoton ionization in bulk SiO₂," *Physical Review B* **81**, 3–6 (2010).
44. E. N. Glezer, M. Milosavljevic, L. Huang, R. J. Finlay, T. H. Her, J. P. Callan, and E. Mazur, "Three-dimensional optical storage inside transparent materials.," *Optics Letters* **21**, 2023–2025 (1996).
45. C. Hnatovsky, R. S. Taylor, P. P. Rajeev, E. Simova, V. R. Bhardwaj, D. M. Rayner, and P. B. Corkum, "Pulse duration dependence of femtosecond-laser-fabricated nanogratings in fused silica," *Applied Physics Letters* **87**, 014104 (2005).
46. W. Yang, E. Bricchi, P. G. Kazansky, J. Bovatsek, and A. Y. Arai, "Self-assembled periodic sub-wavelength structures by femtosecond laser direct writing," *Optics Express* **14**, 10117 (2006).
47. M. Lancry, F. Brisset, and B. Poumellec, "In the heart of nanogratings made up during femtosecond laser irradiation," in *Bragg Gratings, Photosensitivity, and Poling in Glass Waveguides* (2010), p. BWC3.
48. C. Hnatovsky, R. S. Taylor, E. Simova, V. R. Bhardwaj, D. M. Rayner, and P. B. Corkum, "Polarization-selective etching in femtosecond laser-assisted microfluidic channel fabrication in fused silica," *Optics Letters* **30**, 1867 (2005).
49. E. Bricchi and P. G. Kazansky, "Extraordinary stability of anisotropic femtosecond direct-written structures embedded in silica glass," *Applied Physics Letters* **88**, 111119 (2006).
50. R. S. Taylor, C. Hnatovsky, E. Simova, P. P. Rajeev, D. M. Rayner, and P. B. Corkum, "Femtosecond laser erasing and rewriting of self-organized planar nanocracks in fused silica glass," *Optics Letters* **32**, 2888 (2007).
51. Y. Shimotsuma, M. Sakakura, P. G. Kazansky, M. Beresna, J. Qiu, J. Qiu, K. Miura, and K. Hirao, "Ultrafast manipulation of self-assembled form birefringence in glass," *Advanced Materials* **22**, 4039–4043 (2010).
52. E. Bricchi, B. G. Klappauf, and P. G. Kazansky, "Form birefringence and negative index change created by femtosecond direct writing in transparent materials," *Optics Letters* **29**, 119–121 (2004).

53. L. Sudrie, M. Franco, B. Prade, and A. Mysyrowicz, "Writing of permanent birefringent microlayers in bulk fused silica with femtosecond laser pulses," *Optics Communications* **171**, 279–284 (1999).
54. P. Kazansky, H. Inouye, T. Mitsuyu, K. Miura, J. Qiu, K. Hirao, and F. Starrost, "Anomalous Anisotropic Light Scattering in Ge-Doped Silica Glass," *Physical Review Letters* **82**, 2199–2202 (1999).
55. N. F. Borrelli, C. M. Smith, J. J. Price, and D. C. Allan, "Polarized excimer laser-induced birefringence in silica," *Applied Physics Letters* **80**, 219 (2002).
56. M. Ams, G. D. Marshall, and M. J. Withford, "Study of the influence of femtosecond laser polarisation on direct writing of waveguides," *Optics Express* **14**, 13158 (2006).
57. S. M. Eaton, H. Zhang, P. R. Herman, F. Yoshino, L. Shah, J. Bovatsek, and A. Y. Arai, "Heat accumulation effects in femtosecond laser-written waveguides with variable repetition rate," *Optics Express* **13**, 4708 (2005).
58. R. R. Gattass, L. R. Cerami, and E. Mazur, "Micromachining of bulk glass with bursts of femtosecond laser pulses at variable repetition rates," *Optics Express* **14**, 5279 (2006).
59. E. Collett, *Field Guide to Polarization* (SPIE Publications, 2005), p. 148.
60. E. Hasman, Z. Bomzon, A. Niv, and G. Biener, "Polarization beam-splitters and optical switches based on space-variant computer-generated subwavelength quasi-periodic structures," *Optics Communications* **209**, 45–54 (2002).
61. S. Matsuo, "Matrix calculus for axially symmetric polarized beam," *Optics Express* **19**, 12815–12824 (2011).
62. M. Shribak and R. Oldenbourg, "Techniques for fast and sensitive measurements of two-dimensional birefringence distributions," *Applied Optics* **42**, 3009–3017 (2003).
63. Z. Chang, A. Rundquist, H. Wang, M. Murnane, and H. Kapteyn, "Generation of Coherent Soft X Rays at 2.7 nm Using High Harmonics," *Physical Review Letters* **79**, 2967–2970 (1997).
64. X. Xie, J. Dai, and X.-C. Zhang, "Coherent Control of THz Wave Generation in Ambient Air," *Physical Review Letters* **96**, (2006).

65. A. Fedotov, N. Koroteev, M. Loy, X. Xiao, and A. Zheltikov, "Generation of the Second and Third Harmonics in a Laser-Produced Plasma with 1-kHz 90-fs Light Pulses," *Laser Physics* **6**, 427 (1996).
66. Y.-D. Qin, H. Yang, C.-J. Zhu, and Q. Gong, "Intense femtosecond laser-induced second-harmonic generation in atmospheric-pressure air," *Applied Physics B: Lasers and Optics* **71**, 581–584 (2000).
67. K. Miyazaki, T. Sato, and H. Kashiwagi, "Spontaneous-field-induced optical second-harmonic generation in atomic vapors," *Physical Review Letters* 1154–1158 (1979).
68. D. Bethune, "Optical second-harmonic generation in atomic vapors with focused beams," *Physical Review A* **23**, (1981).
69. T. Mossberg, A. Flusberg, and S. R. Hartmann, "Optical second-harmonic generation in atomic thallium vapor," *Optics Communications* **25**, 121–124 (1978).
70. M. Mori, E. Takahashi, and K. Kondo, "Image of second harmonic emission generated from ponderomotively excited plasma density gradient," *Physics of Plasmas* **9**, 2812 (2002).
71. Y. R. Shen, *The Principles of Nonlinear Optics* (Wiley-Interscience, 1984), Vol. -1, p. 575.
72. L. Allen, K. Dholakia, N. Simpson, and M. Padgett, "Second-harmonic generation and the orbital angular momentum of light," *Physical Review A* **54**, R3742–R3745 (1996).
73. A. Bahabad and A. Arie, "Generation of optical vortex beams by nonlinear wave mixing," *Optics express* **15**, 17619–24 (2007).
74. W. Margulis, F. Laurell, and B. Leschel, "Imaging the nonlinear grating in frequency-doubling fibres," *Nature* **378**, 699–701 (1995).
75. P. Kazansky and V. Pruneri, "Electrically Stimulated Light-Induced Second-Harmonic Generation in Glass: Evidence of Coherent Photoconductivity," *Physical Review Letters* **78**, 2956–2959 (1997).

76. R. F. Cregan, B. J. Mangan, J. C. Knight, T. A. Birks, P. St. Russell, P. J. Roberts, and D. C. Allan, "Single-Mode Photonic Band Gap Guidance of Light in Air," *Science* **285**, 1537–1539 (1999).
77. C. Hensley, M. Foster, B. Shim, and A. L. Gaeta, "Extremely high coupling and transmission of high-powered-femtosecond pulses in hollow-core photonic band-gap fiber," in *CLEO* (2008), p. JFG1.
78. J. Durnin, J. Miceli, and J. H. Eberly, "Comparison of Bessel and Gaussian beams," *Optics Letters* **13**, 79 (1988).
79. M. Mansuripur, *Classical Optics and Its Applications* (Cambridge University Press, 2009), p. 701.
80. H. Karstensen and K. Drogemuller, "Loss analysis of laser diode to single-mode fiber couplers with glass spheres or silicon plano-convex lenses," *Journal of Lightwave Technology* **8**, 739–747 (1990).
81. Z. Wang, W. Guo, L. Li, B. Luk'yanchuk, A. Khan, Z. Liu, Z. Chen, and M. Hong, "Optical virtual imaging at 50 nm lateral resolution with a white-light nanoscope.," *Nature communications* **2**, 218 (2011).
82. R. Oldenbourg, "Analysis of edge birefringence.," *Biophysical journal* **60**, 629–41 (1991).
83. L. Marrucci, C. Manzo, and D. Paparo, "Optical Spin-to-Orbital Angular Momentum Conversion in Inhomogeneous Anisotropic Media," *Physical Review Letters* **96**, 1–4 (2006).
84. J. Ferrari, W. Dultz, H. Schmitzer, and E. Frins, "Achromatic wavefront forming with space-variant polarizers: Application to phase singularities and light focusing," *Physical Review A* **76**, 1–7 (2007).
85. S. Juodkazis, H. Misawa, T. Hashimoto, E. G. Gamaly, and B. Luther-Davies, "Laser-induced microexplosion confined in a bulk of silica: Formation of nanovoids," *Applied Physics Letters* **88**, 201909 (2006).

86. R. Graf, A. Fernandez, M. Dubov, H. J. Brueckner, B. N. Chichkov, and A. Apolonski, *Pearl-chain Waveguides Written at Megahertz Repetition Rate* (Springer Berlin / Heidelberg, 2007), Vol. 87, pp. 21–27.
87. Y. Bellouard and M.-O. Hongler, "Femtosecond-laser generation of self-organized bubble patterns in fused silica.," *Optics Express* **19**, 6807–21 (2011).
88. E. Toratani, M. Kamata, and M. Obara, "Self-fabrication of void array in fused silica by femtosecond laser processing," *Applied Physics Letters* **87**, 171103 (2005).
89. S. Kanehira, J. Si, J. Qiu, K. Fujita, and K. Hirao, "Periodic nanovoid structures via femtosecond laser irradiation.," *Nano Letters* **5**, 1591–1595 (2005).
90. J. Song, X. Wang, X. Hu, Y. Dai, J. Qiu, Y. Cheng, and Z. Xu, "Formation mechanism of self-organized voids in dielectrics induced by tightly focused femtosecond laser pulses," *Applied Physics Letters* **92**, 092904 (2008).
91. D. P. Hand and P. S. J. Russell, "Solitary thermal shock waves and optical damage in optical fibers: the fiber fuse," *Optics Letters* **13**, 767–769 (1988).
92. S. Hardy, "The motion of bubbles in a vertical temperature gradient," *Journal of Colloid and Interface Science* **69**, 157–162 (1979).
93. N. O. Young, J. S. Goldstein, and M. J. Block, "The motion of bubbles in a vertical temperature gradient," *Journal of Fluid Mechanics* **6**, 350 (1959).
94. R. S. Taylor, E. Simova, and C. Hnatovsky, "Creation of chiral structures inside fused silica glass," *Optics Letters* **33**, 1312 (2008).
95. B. Poumellec, L. Sudrie, M. Franco, B. Prade, and A. Mysyrowicz, "Femtosecond laser irradiation stress induced in pure silica," *Optics Express* **11**, 1070 (2003).
96. P. Török, "Imaging of small birefringent objects by polarised light conventional and confocal microscopes," *Optics Communications* **181**, 7–18 (2000).
97. E. Brasselet, M. Malinauskas, A. Žukauskas, and S. Juodkazis, "Photopolymerized microscopic vortex beam generators: Precise delivery of optical orbital angular momentum," *Applied Physics Letters* **97**, 211108 (2010).

98. M. Birnbaum, "Semiconductor Surface Damage Produced by Ruby Lasers," *Journal of Applied Physics* **36**, 3688 (1965).
99. A. Siegman and P. Fauchet, "Stimulated Wood's anomalies on laser-illuminated surfaces," *Quantum Electronics, IEEE Journal of* 1384–1403 (1986).
100. Z. Guosheng, P. M. Fauchet, and A. E. Siegman, "Growth of spontaneous periodic surface structures on solids during laser illumination," *Physical Review B* **26**, (1982).
101. P. Fauchet and A. E. Siegman, "Surface ripples on silicon and gallium arsenide under picosecond laser illumination," *Applied Physics Letters* **824**, 1–4 (1982).
102. D. C. Emmony, R. P. Howson, and L. J. Willis, "Laser mirror damage in germanium at 10 . 6 μm ," *Applied Physics Letters* **23**, 598 (1973).
103. L. J. Willis and D. C. Emmony, "Laser damage in germanium," *Optics & Laser Technology* **7**, 228–222 (1975).
104. G. N. Maracas, G. L. Harris, C. A. Lee, and R. A. McFarlane, "On the origin of periodic surface structure of laser annealed semiconductors," *Applied Physics Letters* **33**, 453–455 (1978).
105. J. A. Van Vechten, "Experimental tests for boson condensation and superconductivity in semiconductors during pulsed beam annealing," *Solid State Communications* **39**, 1285–1291 (1981).
106. F. Keilmann and Y. H. Bai, "Periodic surface structures frozen into CO₂ laser-melted quartz," *Applied Physics A Solids and Surfaces* **29**, 9–18 (1982).
107. J. Sipe, J. Young, J. Preston, and H. van Driel, "Laser-induced periodic surface structure. I. Theory," *Physical Review B* **27**, 1141–1154 (1983).
108. A. Borowiec and H. K. Haugen, "Subwavelength ripple formation on the surfaces of compound semiconductors irradiated with femtosecond laser pulses," *Applied Physics Letters* **82**, 4462 (2003).
109. N. Yasumaru, K. Miyazaki, and J. Kiuchi, "Femtosecond-laser-induced nanostructure formed on hard thin films of TiN and DLC," *Applied Physics A: Materials Science & Processing* **76**, 983–985 (2003).

110. G. Miyaji and K. Miyazaki, "Origin of periodicity in nanostructuring on thin film surfaces ablated with femtosecond laser pulses.," *Optics express* **16**, 16265–71 (2008).
111. J. Gottmann, D. Wortmann, and M. Hörstmann-Jungemann, "Fabrication of sub-wavelength surface ripples and in-volume nanostructures by fs-laser induced selective etching," *Applied Surface Science* **255**, 5641–5646 (2009).
112. V. Bhardwaj, E. Simova, P. Rajeev, C. Hnatovsky, R. Taylor, D. Rayner, and P. Corkum, "Optically Produced Arrays of Planar Nanostructures inside Fused Silica," *Physical Review Letters* **96**, 057404 (2006).
113. R. Taylor, C. Hnatovsky, and E. Simova, "Applications of femtosecond laser induced self-organized planar nanocracks inside fused silica glass," *Laser & Photonics Review* **2**, 26–46 (2008).
114. R. Buividas, L. Rosa, R. Sliupas, T. Kudrius, G. Sleky, V. Datsyuk, and S. Juodkazis, "Mechanism of fine ripple formation on surfaces of (semi)transparent materials via a half-wavelength cavity feedback.," *Nanotechnology* **22**, 055304 (2011).
115. M. Beresna, M. Gecevičius, P. G. Kazansky, T. Taylor, and A. V. Kavokin, "Exciton mediated self-organization in glass driven by ultrashort light pulses," *Applied Physics Letters* **101**, 053120 (2012).
116. G. Malpuech, A. Kavokin, and G. Panzarini, "Propagation of exciton polaritons in inhomogeneous semiconductor films," *Physical Review B* **60**, 16788–16798 (1999).
117. F. Messina, E. Vella, M. Cannas, and R. Boscaino, "Evidence of Delocalized Excitons in Amorphous Solids," *Physical Review Letters* **105**, 1–4 (2010).
118. E. Vella, F. Messina, M. Cannas, and R. Boscaino, "Unraveling exciton dynamics in amorphous silicon dioxide: Interpretation of the optical features from 8 to 11 eV," *Physical Review B* **83**, 4–11 (2011).
119. M. Vladimirova, S. Cronenberger, D. Scalbert, M. Nawrocki, A. Kavokin, A. Miard, A. Lemaître, and J. Bloch, "Polarization controlled nonlinear transmission of light through semiconductor microcavities," *Physical Review B* **79**, (2009).

120. A. Verger, C. Ciuti, and I. Carusotto, "Polariton quantum blockade in a photonic dot," *Physical Review B* **73**, (2006).
121. P. Martin, S. Guizard, P. Daguzan, G. Petite, P. D'Oliveira, P. Meynadier, and M. Perdrix, "Subpicosecond study of carrier trapping dynamics in wide-band-gap crystals," *Physical Review B* **55**, 5799 (1997).
122. L. Bressel, D. de Ligny, E. G. Gamaly, A. V. Rode, and S. Juodkasis, "Observation of O₂ inside voids formed in GeO₂ glass by tightly-focused fs-laser pulses," *Optical Materials Express* **1**, 1150 (2011).
123. C. Gu and P. Yeh, "Form birefringence dispersion in periodic layered media," *Optics Letters* **21**, 504 (1996).
124. M. Born and E. Wolf, *Principles of Optics: Electromagnetic Theory of Propagation, Interference and Diffraction of Light* (Cambridge University Press; 7 edition, 1999), p. 986.
125. H. Kikuta, Y. Ohira, and K. Iwata, "Achromatic quarter-wave plates using the dispersion of form birefringence.," *Applied optics* **36**, 1566–72 (1997).
126. A. Zoubir, C. Rivero, R. Grodsky, K. Richardson, M. Richardson, T. Cardinal, and M. Couzi, "Laser-induced defects in fused silica by femtosecond IR irradiation," *Physical Review B* **73**, 1–5 (2006).
127. J. Lin, O. Rodr'iguez-Herrera, F. Kenny, D. Lara, and J. Dainty, "Fast vectorial calculation of the volumetric focused field distribution by using a three-dimensional Fourier transform," *Optics Express* **20**, 1060–1069 (2012).
128. J. A. Davis, J. Adachi, C. R. Fernández-Pousa, and I. Moreno, "Polarization beam splitters using polarization diffraction gratings.," *Optics Letters* **26**, 587 (2001).
129. Z. Bomzon, V. Kleiner, and E. Hasman, "Formation of radially and azimuthally polarized light using space-variant subwavelength metal stripe gratings," *Applied Physics Letters* **79**, 1587 (2001).
130. R. Yamaguchi, T. Nose, and S. Sato, "Liquid Crystal Polarizers with Axially Symmetrical Properties," *Japanese Journal of Applied Physics* **28**, 1730–1731 (1989).

131. D. Mawet, P. Riaud, J. Surdej, and J. Baudrand, "Subwavelength surface-relief gratings for stellar coronagraphy.," *Applied Optics* **44**, 7313 (2005).
132. F. Gori, "Measuring Stokes parameters by means of a polarization grating.," *Optics Letters* **24**, 584–586 (1999).
133. J. E. Ford, F. Xu, K. Urquhart, and Y. Fainman, "Polarization-selective computer-generated holograms V-pol input :," *Optics Letters* **18**, 456–458 (1993).
134. H. Ono, H. Wakabayashi, T. Sasaki, A. Emoto, T. Shioda, and N. Kawatsuki, "Vector holograms using radially polarized light," *Applied Physics Letters* **94**, 071114 (2009).
135. G. Cipparrone, A. Mazzulla, S. P. Palto, S. G. Yudin, and L. M. Blinov, "Permanent polarization gratings in photosensitive Langmuir–Blodgett films," *Applied Physics Letters* **77**, 2106 (2000).
136. G. Cipparrone, P. Pagliusi, C. Provenzano, and V. P. Shibaev, "Polarization holographic recording in amorphous polymer with photoinduced linear and circular birefringence.," *The Journal of Physical Chemistry B* **114**, 8900 (2010).
137. Y. Bellouard, E. Barthel, A. A. Said, M. Dugan, and P. Bado, "Scanning thermal microscopy and Raman analysis of bulk fused silica exposed to lowenergy femtosecond laser pulses," *Optics Express* **16**, 19520 (2008).
138. S. Quabis, R. Dorn, M. Eberler, O. Glockl, and G. Leuchs, "Focusing light to a tighter spot," *Optics Communications* **179**, 1–7 (2000).
139. R. Dorn, S. Quabis, and G. Leuchs, "Sharper Focus for a Radially Polarized Light Beam," *Physical Review Letters* **91**, (2003).
140. B. Hao and J. Leger, "Experimental measurement of longitudinal component in the vicinity of focused radially polarized beam.," *Optics express* **15**, 3550–6 (2007).
141. D. P. Biss and T. G. Brown, "Polarization-vortex-driven second-harmonic generation.," *Optics Letters* **28**, 923–925 (2003).
142. S. Carrasco, B. E. A. Saleh, M. C. Teich, and J. T. Fourkas, "Second- and third-harmonic generation with vector Gaussian beams," *Journal of the Optical Society of America B* **23**, 2134–2141 (2006).

143. D. P. Biss, K. S. Youngworth, and T. G. Brown, "Dark-field imaging with cylindrical-vector beams.," *Applied Optics* **45**, 470–9 (2006).
144. Q. Zhan, "Evanescent Bessel beam generation via surface plasmon resonance excitation by a radially polarized beam," *Optics Letters* **31**, 1726 (2006).
145. H. Kang, B. Jia, J. Li, D. Morrish, and M. Gu, "Enhanced photothermal therapy assisted with gold nanorods using a radially polarized beam," *Applied Physics Letters* **96**, 063702 (2010).
146. Y. Liu, D. Cline, and P. He, "Vacuum laser acceleration using a radially polarized CO₂ laser beam," *Nuclear Instruments and Methods in Physics Research Section A: Accelerators, Spectrometers, Detectors and Associated Equipment* **424**, 296–303 (1999).
147. W. Chen and Q. Zhan, "Three-dimensional focus shaping with cylindrical vector beams," *Optics Communications* **265**, 411–417 (2006).
148. H. Wang, L. Shi, B. Lukyanchuk, C. Sheppard, and C. T. Chong, "Creation of a needle of longitudinally polarized light in vacuum using binary optics," *Nature Photonics* **2**, 501–505 (2008).
149. V. G. Niziev and A. V Nesterov, "Influence of beam polarization on laser cutting efficiency," *Journal of Physics D: Applied Physics* **32**, 1455–1461 (1999).
150. M. Endo, "Sheet metal cutting with a 2 kW radially polarized CO," in *Proceedings of SPIE* (2010), Vol. 7751, p. 77511B–77511B–9.
151. Q. Zhan, "Cylindrical vector beams: from mathematical concepts to applications," *Advances in Optics and Photonics* **1**, 1–57 (2009).
152. D. Pohl, "Operation of a Ruby Laser in the Purely Transverse Electric Mode TE₀₁," *Applied Physics Letters* **20**, 266 (1972).
153. Y. Kozawa and S. Sato, "Generation of a radially polarized laser beam by use of a conical Brewster prism," *Optics Letters* **30**, 3063 (2005).
154. C. Hnatovsky, V. Shvedov, W. Krolikowski, and A. Rode, "Revealing Local Field Structure of Focused Ultrashort Pulses," *Physical Review Letters* **106**, 123901 (2011).

155. M. R. Beversluis, L. Novotny, and S. J. Stranick, "Programmable vector point-spread function engineering.," *Optics Express* **14**, 2650 (2006).
156. E. Walker and P. M. Rentzepis, "Two-photon technology: A new dimension," *Nature Photonics* **2**, 406–408 (2008).
157. M. Kaempfe, T. Rainer, K.-J. Berg, G. Seifert, and H. Graener, "Ultrashort laser pulse induced deformation of silver nanoparticles in glass," *Applied Physics Letters* **74**, 1200 (1999).
158. P. Zijlstra, J. W. M. Chon, and M. Gu, "Five-dimensional optical recording mediated by surface plasmons in gold nanorods.," *Nature* **459**, 410 (2009).